From the Lübeck Institute of Experimental Dermatology
of the University of Lübeck
Director: Prof. Dr. Saleh M. Ibrahim

Interplay of mtDNA, metabolism and microbiota in the pathogenesis of AIBD

Dissertation

for Fulfillment of

Requirements

for the Doctoral Degree

of the University of Lübeck

from the Department of Natural Sciences

Submitted by

Paul Schilf
from Rostock

Lübeck, 2016

First referee: Prof. Dr. Saleh M. Ibrahim

Second referee: Prof. Dr. Stephan Anemüller

Chairman: Prof. Dr. Rainer Duden

Date of oral examination: 30.03.2017

Approved for printing: Lübeck, 06.04.2017

Ich versichere, dass ich die Dissertation ohne fremde Hilfe angefertigt und keine anderen als die angegebenen Hilfsmittel verwendet habe. Weder vorher noch gleichzeitig habe ich andernorts einen Zulassungsantrag gestellt oder diese Dissertation vorgelegt.

ABSTRACT

Mitochondria are critical in the regulation of cellular metabolism and influence signaling processes and inflammatory responses. Mitochondrial DNA mutations and mitochondrial dysfunction are known to cause a wide range of pathological conditions and are associated with various immune diseases. The findings in this work describe the effect of a mutation in the mitochondrially encoded *mt-Atp8* gene in the conplastic mouse strain C57BL/6J-mt$^{FVB/NJ}$ on the mitochondrial function and consequent alterations to metabolic and immunological phenotypes. This work provides insights into the mutation-induced cellular adaptations that influence the inflammatory milieu and shape pathological processes, in particular focusing on autoimmune bullous diseases, which have recently been reported to be associated with mtDNA polymorphisms in the human *MT-ATP8* gene. The *mt-Atp8* mutation diminishes the assembly of the ATP synthase complex into multimers and decreases mitochondrial respiration, affects generation of reactive oxygen species thus leading to a shift in the metabolic balance and reduction in the energy state of the cell as indicated by the ratio ATP to ADP. The metabolic alterations are concomitant with diminished function of the immune system as the *mt-Atp8* mutation limits the activation, proliferation, and pro-inflammatory potential of immune cell populations. The *mt-Atp8* mutation is associated with an alteration in the composition of the skin microbiota, potentially affecting the homeostasis of the immune milieu at the skin barrier. The effects of the *mt-Atp8* mutation coincide with amelioration of the pathogenesis of experimental autoimmune bullous disease model of Epidermolysis bullosa acquisita.

ZUSAMMENFASSUNG

Mitochondrien sind integraler Bestandteil in der Regulation des zellulären Metabolismus, sowie Signaltransduktion und entzündlichen Prozessen. Mutationen in der mitochondrialen DNA und mitochondriale Dysfunktion sind bekannte Ursachen in einem weiten Spektrum von Erkrankungen und sind assoziiert mit diversen immunologischen Erkrankungen. Kern dieser Arbeit sind die Effekte einer Mutation im mitochondrial-kodierten *mt-Atp8* Gen in dem conplastischen Mausstamm C57BL/6J-mt$^{FVB/NJ}$ auf mitochondriale Funktionen und infolgedessen auf metabolische und immunologische Funktionen. Diese Arbeit liefert Erkenntnisse über die mutationsbedingten zellulären Anpassungen welche das Entzündungs-milieu beeinflussen und pathologische Prozesse, insbesondere bullöse Autoimmundermatosen, regulieren. In einer kürzlich veröffentlichen Assoziationsstudie konnte eine mögliche Verbindung zwischen Polymorphismen im humanen *MT-ATP8* Gen und einer Untergruppe von bullösen Autoimmundermatosen gezeigt werden. In der vorliegenden Arbeit konnte anhand eines Mausmodells gezeigt werden, dass eine Mutation im *mt-Atp8* Gen die Oligomerisierung des ATP Synthase-Komplexes mindert, die mitochondriale Respiration reduziert, die Produktion von reaktiven Sauerstoffspezies beeinflusst, das metabolische Gleichgewicht verschiebt und den zellulären Energiestatus herabsetzt. Die metabolischen Veränderungen in den *mt-Atp8* Mutanten sind verbunden mit einer Limitierung des Immunsystems, verdeutlicht durch verminderte Aktivierung und Proliferation von Immunzellpopulationen, sowie Limitierung deren pro-inflammatorischen Potentials. Die *mt-Atp8* Mutation ist assoziiert mit einer Verschiebung in der Zusammensetzung der Hautflora und beeinflusst potentiell die Homöostase des Immun-milieu in der Hautbarriere. Die beobachteten Einflüsse der *mt-Atp8* Mutation sind in Übereinstimmung mit einer Milderung in der Pathogenese von bullösen Autoimmundermatosen in einem Tiermodell für Epidermolysis bullosa acquisita.

TABLE OF CONTENTS

LIST OF FIGURES

LIST OF TABLES

ABBREVIATIONS

2-DG – 2-Deoxyglucose
ADP – Adenosine triphosphate
AIBD – Autoimmune bullous skin diseases
ATP – Adenosine diphosphate
AUC – Area under curve
B6 - C57BL/6J
B6-mtFVB – C57BL/6J-mt$^{FVB/NJ}$
BrdU - 5-Bromo-2′-deoxyuridine
BSA – Bovine serum albumin
CI – Complex I, NADH-quinone oxidoreductase / NADH dehydrogenase
CIII – Complex III, cytochrome c oxidoreductase, Cytochrome bc1 complex
CIV – Complex IV, cytochrome c oxidase
CV – Complex V, F_0F_1-ATP Synthase
CCCP – Carbonyl cyanide 3-chlorophenylhydrazone
CIS – Common inbred strain, mouse
ddH_2O – Double distilled water
DDM – N-Dodecyl β-D-maltoside
DEJ – Dermal-epidermal junction
EEx – Energy expenditure
ETC – Electron transport chain
FCCP – Carbonyl cyanide 4-(trifluoromethoxy)phenylhydrazone
FCS – Fetal calf serum
HRP – Horseradish peroxidase
IgG – Immunoglobulin G
IL- Interleukin
InfraMot – Infrared light motion detection of locomotor activity
LDH – Lactate dehydrogenase
mCol7 – Murine type VII collagen
MID – Multiplex Identifiers
MMP – Mitochondrial membrane potential ($\Delta\psi$)
mtDNA – Mitochondrial DNA
mtROS – mitochondrial-derived reactive oxygen species
MUFA – Mono-unsaturated fatty acids
NAD^+ – Nicotineamide adenine dinucleotide, oxidized form
NADH – Nicotineamide adenine dinucleotide reduced form
NGS – next generation sequencing

OXPHOS – Oxidative phosphorylation system comprising respiratory chain enzymes (complex I, II, III, IV) and the ATP synthase (complex V)
Pen/Strep – Penicillin/Streptomycin
PEP – Phosphoenolpyruvate
PK – Pyruvate kinase
PUFA – Poly-unsaturated fatty acids
qPCR – Quantitative polymerase chain reaction
RER – Respiratory exchange ratio
SCFA – Short chain fatty acids
SFA – Saturated fatty acids
SDS – Sodium dodecyl sulphate
SNP – Single nucleotide polymorphism
TCA cycle – Tricarboxylic acid cycle
TMRE – Tetramethylrhodamine ethyl ester

1 INTRODUCTION

1.1 Mitochondria

Mitochondria are cellular organelles of critical importance in an ever increasing numbers of cellular processes and signaling pathways. Mitochondria provide the majority of energy to the cell in form of ATP. Production of ATP in the mitochondria is facilitated in the oxidative phosphorylation system (OXPHOS). Substrates that are introduced into the tricarboxylic acid cycle (TCA cycle) fuel the reduction of NAD^+ to NADH as well as FAD to $FADH_2$. The following oxidation of NADH and $FADH_2$ in the respiratory chain leads to an accumulation of protons in the mitochondrial intermembrane space. The proton gradient generated by the respiratory chain enzymes is harnessed by the ATP synthase, located in the inner mitochondrial membrane, to phosphorylate ADP to ATP using the proton-motive force of the mitochondrial membrane potential. While the majority of the approximately 1200-2000 known mitochondria-associated proteins (Calvo et al., 2016; Smith and Robinson, 2016) are encoded in the nucleus, the mitochondrial genome (mitochondrial DNA; mtDNA) encodes a total of 37 genes (13 protein coding genes, 22 tRNAs, 2 rRNAs) (Anderson et al., 1981; Bibb et al., 1981). The protein coding genes encode subunits of the oxidative phosphorylation system (complex I: *mt-Nd1*, *mt-Nd2*, *mt-Nd3*, *mt-Nd4*, *mt-Nd4l*, and *mt-Nd5*; complex III: *mt-Cytb*; complex IV: *mt-Co1*, *mt-Co2*, *mt-Co3*; complex V: *mt-Atp6*, *mt-Atp8*). Each cell contains multiple copies of mtDNA, showing tissue specific variations ranging for several hundreds to thousands of copies per cell (Kelly et al., 2012).

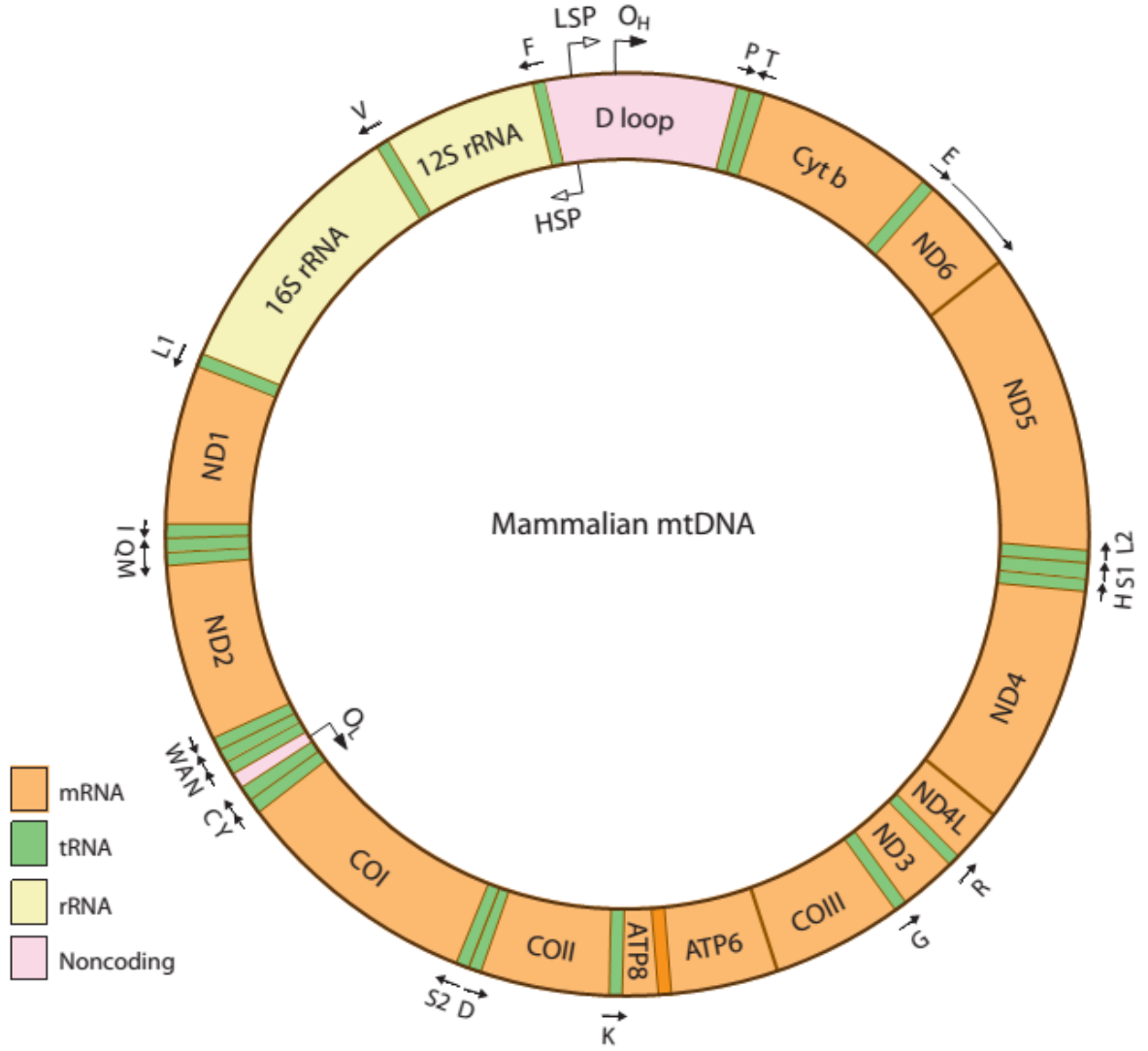

Figure 1. Mammalian mtDNA is a double-stranded circular molecule. The two strands are denoted the heavy (H) and light (L) strand due to different buoyant densities. The only longer noncoding region, the displacement loop (D loop), contains a triplex structure with a nascent H strand. The D loop contains the promoters for transcription of the H and L strand (HSP and LSP) as well as the origin of replication of the leading strand of mtDNA (O_H). The origin of replication of the lagging strand (O_L) is located in a cluster of tRNA genes. Transcription from HSP produces 2 rRNAs (12S and 16S rRNA), 12 mRNAs (ND1–5, ND4L, Cyt b, COI–III, ATP6, and ATP8), and 14 tRNAs (F, V, L1, I, M, W, D, K, G, R, H, S1, L2, T). Transcription from LSP has a dual function. First, it produces RNA primers needed for initiation of replication at O_H. Second, it is needed to produce one mRNA (ND6) and eight tRNAs (P, E, S2, Y, C, N, A, Q). Illustration by Annika Röhl. (Larsson, 2010)

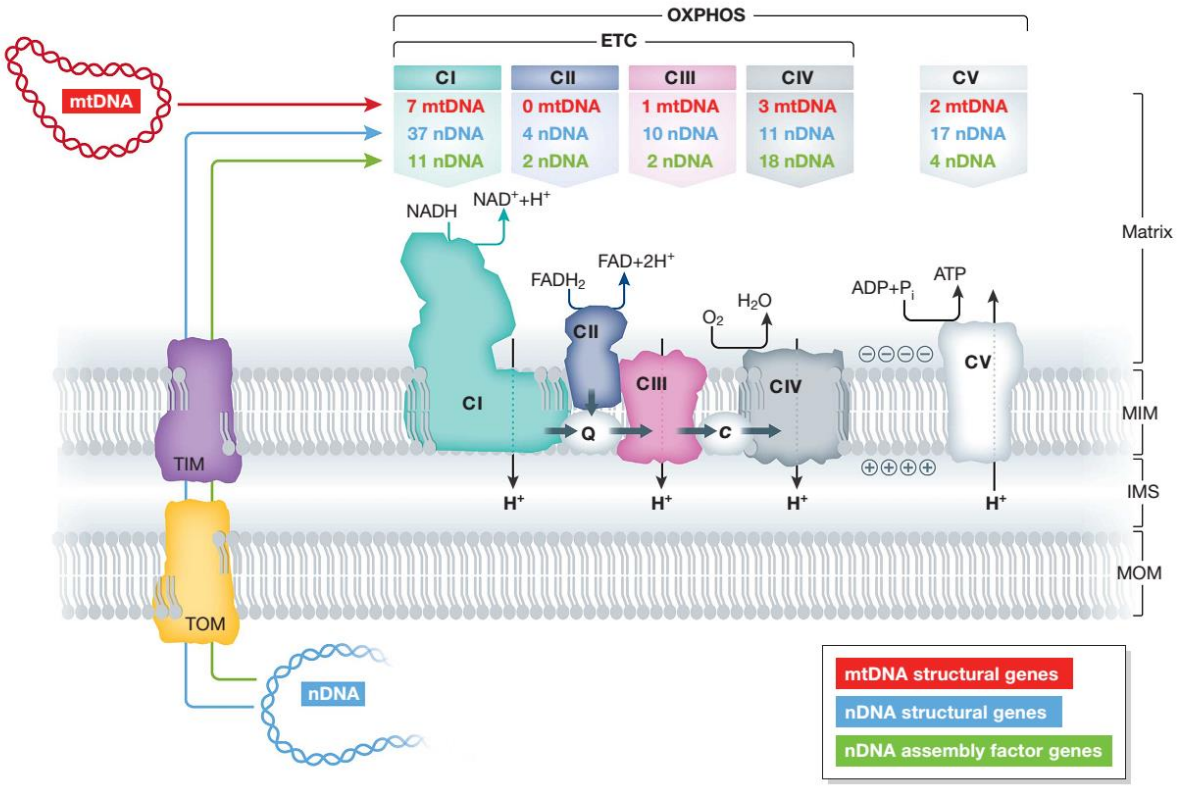

Figure 2. Genetic origin and functional interaction of the mitochondrial oxidative phosphorylation (OXPHOS) complexes. The mitochondrial OXPHOS system consists of five multi-subunit complexes (CI–CV) that reside in the mitochondrial inner membrane (MIM). The MIM encloses the mitochondrial matrix and is surrounded by the mitochondrial outer membrane (MOM). An inter-membrane space (IMS) is located between the MIM and MOM. The subunits of CI, CIII, CIV and CV are encoded by the mitochondrial (mtDNA; red) and nuclear DNA (nDNA; blue), whereas CII exclusively consists of nDNA-encoded subunits (table at the top). OXPHOS biogenesis is mediated by nDNA-encoded assembly factors (green). The nDNA-encoded proteins are imported into the mitochondrial matrix via the TOM (translocator of the inner membrane) and TIM (translocator of the inner membrane) systems. At CI and CII, NADH and $FADH_2$ are oxidized, respectively, and the released electrons are transported to CIII via Coenzyme Q_{10} (CoQ_{10}; 'Q'). From thereon, electrons are transported to CIV via cytochrome-c(cyt-c;'c') and donated to oxygen (O_2). Together, CI–CIV constitute the electron transport chain (ETC). The energy derived from the electron transport is used to expel protons (H^+) from the mitochondrial matrix across the MIM. This establishes an electrochemical proton-motive force, associated with an inside-negative mitochondrial membrane potential ($\Delta\psi$) and increased matrix pH. The controlled backflow of H^+ is used by CV to drive the production of ATP (Koopman et al., 2012).

Efficient mitochondrial function relies heavily on the balance between the mitochondrial and nuclear gene regulation. Imbalance in mito-nuclear regulation can have a severe systemic impact, i.e. influencing the aging process and affecting longevity (Houtkooper et al., 2013).

Through the integration of anabolic and catabolic pathways, mitochondria form a hub for metabolic flux. Many signaling pathways involve

mitochondrial functions like the production of reactive oxygen species (ROS) to facilitate activation of specific pathways (NLRP3 – inflammasome (Zhou et al., 2011); T cell activation (Sena et al., 2013a) or shape the general response of cellular phenotypes (apoptosis; ROS induced UPR/mitophagy to alter protein turnover (Hamanaka and Chandel, 2010). By influencing the equilibrium of metabolites, mitochondria determine the cellular response to signal transduction (Martínez-Reyes et al., 2016; Mishur et al., 2016; Ribas et al., 2016).

Mitochondria are not only important for general metabolic regulation and energy production they also play a critical role in immune cell function (Weinberg et al., 2015). In recent years the integral role of mitochondria has been shown in a variety of immune cell functions, i.e. macrophage polarization, innate immune signaling response, T cell activation, T cell differentiation, and memory T cell formation (Bengsch et al., 2016; O'Neill et al., 2016b; Weinberg et al., 2015).

1.2 **Mitochondrial disease and mtDNA mutations**

Due to the critical importance of mitochondria for energy metabolism and metabolic flux control in the cell, dysfunction of mitochondria is associated with a wide range of pathological conditions which also include diseases such as type 2 diabetes, Parkinson's disease, and Alzheimer's disease (Schapira, 2006; Shoffner et al., 1993). The classical mitochondrial diseases are commonly described as single or multi-organ pathologies accompanied with mitochondrial dysfunction caused by mitochondrial DNA mutations (Chinnery and Hudson, 2013; Kenney et al., 2014; Schapira, 2006; Taylor and Turnbull, 2005; Wallace and Chalkia, 2013). The list of pathologies that

are associated with mitochondrial dysfunction as well as mtDNA mutations has grown considerably over the years supporting the importance of the integrative function of mitochondrial metabolism in the context of cellular signaling processes.

Due to the critical importance to the energy metabolism, mutations in proteins associated with the OXPHOS system are often deleterious and result in an imbalance of the OXPHOS system. The mtDNA encoded genes show increased likelihood of accumulating mutations and are of particular interest in mitochondrial dysfunctions. The high copy number of mtDNA initially helps to mask potentially detrimental mutations. However, due to unequal segregation of mtDNA during mitosis the fraction of mutated mtDNA copies can reach a threshold at which point pathological conditions become apparent (Stewart and Chinnery, 2015). Amongst the genes encoded in the mtDNA, two genes encode subunits of the F_0F_1 ATP synthase.

The ATP synthase, complex V in the oxidative phosphorylation system is critical for the generation of ATP in mitochondria. Thus it is not surprising that mutations in this enzyme complex have been reported in humans that have detrimental effects resulting in mitochondrial disease and other pathologies (Jonckheere et al., 2009; Mayr et al., 2004, 2010). Multiple pathologies have been identified in the mitochondrial encoded *MT-ATP8* gene specifically (Jonckheere et al., 2012; Kytövuori et al., 2016). The effect and extend of the observed phenotypes strongly depends on the mutation site and deficiency severity (Čížková et al., 2008).

1.3 **Study of mtDNA SNPs using conplastic mouse strains**

It is well established that small to large scale deletions of mtDNA fragments and dominant deleterious mtDNA polymorphism have dramatic effect on the mitochondrial function and lead to severe multi-organ pathologies (mitochondrial diseases) (Schapira, 2006; Taylor and Turnbull, 2005; Wallace, 1999). On the other hand, mtDNA polymorphisms with potentially mild modulatory function that contribute to pathological conditions are less obvious and usually only found in genetic associations studies (Chinnery et al., 2010; Dankowski et al., 2016; Hudson et al., 2014; Samuels et al., 2006; van der Walt et al., 2004; Yu et al., 2008). Investigation of such polymorphisms however could give valuable mechanistic insight into the modulatory influence on disease susceptibility. A conventional method to study mtDNA mutations has been the use of cybrid cell lines (cytoplasmic hybrid/ transmitochondrial hybrid) in which enucleated cells are fused with ρ0 cells (rho0: cells depleted of mitochondrial DNA) (Vithayathil et al., 2012). This approach, however, may fail to deplete the mitochondria completely and yield a heteroplasmic cell containing both wild-type and introduced mutant mitochondria. Similarly the generation transmitochondrial mouse strains by this approach may introduce high variability in the phenotypes due to various degrees of heteroplasmy and it might not be feasible for many purposes (Pinkert and Trounce, 2002). Similarly, the mitochondrial "mutator mouse" has been described in which a mutated, error-prone mitochondrial polymerase introduces random mutations in the mtDNA. (Edgar and Trifunovic, 2009; Trifunovic et al., 2004). These conventional approaches to edit the mitochondrial DNA may lead to the introduction of heteroplasmy and a possible selective segregation of mitochondria and mtDNA during mitosis. This in turn may result in uneven distribution of the mutation load across several cell

divisions and generate heterogeneous cell populations. This scenario is unfavorable in most experimental situations as the effect of mtDNA mutations may depend on a particular threshold of heteroplasmy to become apparent (Stewart and Chinnery, 2015; Wallace and Chalkia, 2013).

The discovery that common inbred mouse strain (CIS) are closely related and exhibit nearly identical mitochondrial sequences and only differ by a few natural mutations that have accumulated during the establishment of the lines (Goios et al., 2007), led to the idea and establishment of a public resource of conplastic mouse strains (Yu et al., 2009a). The fact that mitochondria are exclusively maternally inherited allows the generation of mice carrying mtDNA mutations by simple backcross breeding. A female mouse of the mitochondrial donor strain is bred with a male mouse of the desired nuclear genome (nDNA) background. The female progeny, containing the desired mtDNA haplotype and a heterogeneous nuclear genome, is continuously breed with males of the desired nDNA background and thus in each generation the variation in the nDNA is decreased (Figure 3). After approximately 10 generations this breeding scheme is considered to yield conplastic mouse strains that differ in their mtDNA haplotype by defined SNPs, yet are identical in regard of the nuclear genome (Yu et al., 2009a). Genotyping the conplastic and reference mice using the Mega Mouse Universal Genotyping Array (Mega MUGA; Gene- Seek, Lincoln, NE) which contains 77’000 SNPs across the entire nuclear genome confirmed that the nuclear genomes of both strains are virtually identical (Bär et al., 2013).

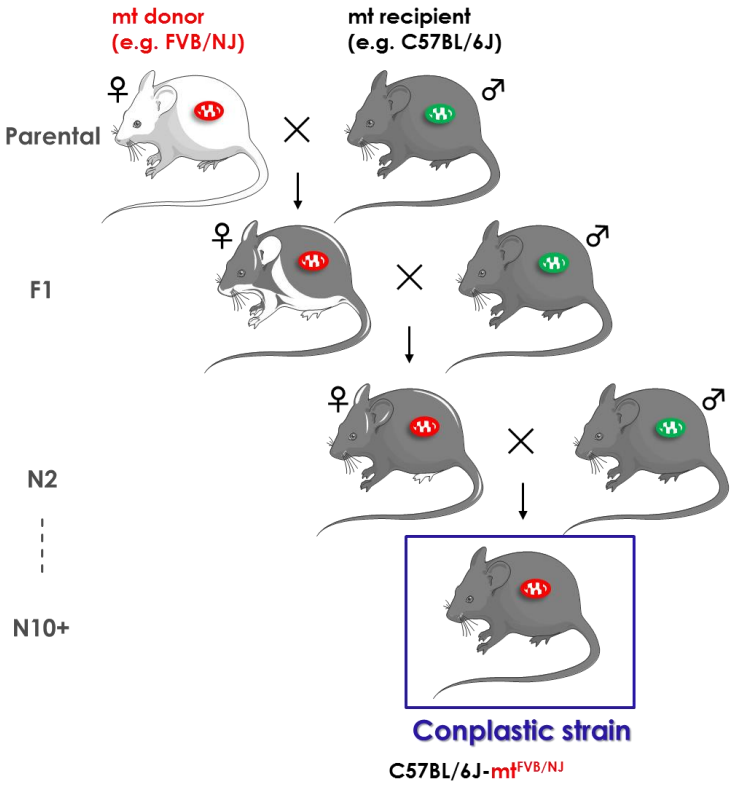

Figure 3. Schematic representation of the breeding pattern to generate conplastic mouse strains.

As a result, the use of these conplastic mouse strains allows the study of specific mutations in the context of various genetic environments and can be integral to identify the impact of mtDNA mutations in disease models.

1.4 Mouse model susceptibility and *mt-Atp8* single nucleotide polymorphism

A few years ago a variety of conplastic mouse strains have been generated amongst which is the strain C57BL6/J-mt$^{FVB/NJ}$ (B6-mtFVB) (Yu et al., 2009a). The comparison of the mtDNA sequences of wild-type C57BL6/J mice (B6) and conplastic B6-mtFVB mice reveals three polymorphic positions (Table 1). At position nt9461 of the *mt-Nd3* gene in the mtDNA the conplastic strain carries a substitution of cytosine (C) to thymine (T)

resulting in a synonymous mutation in a methionine codon of the *mt-Nd3* gene. Furthermore, the B6-mtFVB strain contains an additional adenine in the arginine-tRNA ($tRNA^{Arg}$) gene *mt-Tr* at position 9821insA increasing the adenine repeat sequences from 8A to 9A. This mutation however is unlikely to induce functional alteration. The length of the A repeat located in the D-loop region of the $tRNA^{Arg}$ may influence mitochondrial function if the repeat sequence in the loop is reaching a certain threshold (10A and more) but no differences were observed between 8A and 9A (Johnson et al., 2001; Moreno-Loshuertos et al., 2006). Of particular interest for this work is the mutation in the *mt-Atp8* gene at position nt7778 in the mtDNA. The conplastic mouse strain B6-mtFVB carries a substitution of guanine to thymine resulting in an amino acid substitution from aspartate to tyrosine (Table 1, Figure 4).

Table 1. Mitochondrial DNA polymorphisms in conplastic mtDNA mutant and wild-type mice. Amino acid substitution in mt-Atp8 gene, synonymous mutation in mt-Nd3 gene, insertion in adenine-repeat in mitochondrial arginine-tRNA (mt-Tr). Asp: Aspartate; Tyr: Tyrosine; Met: Methionine; mtXXXX: nucleotide position in the mitochondrial DNA.

Gene	Nucleotide			Amino Acid Substitution
	Position	C57BL/6J	C57BL/6J-$mt^{FVB/NJ}$	
mt-Atp8	**mt7778**	**G**	**T**	**Asp → Tyr**
mt-Nd3	mt9461	C	T	synonymous (Met→ Met)
mt-Tr	mt9821	8A	9A	-

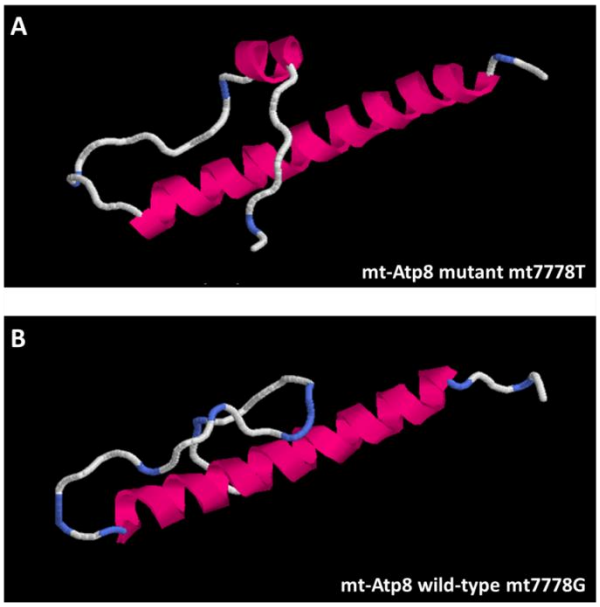

Figure 4. Automated protein structure of mt-Atp8 encoded protein subunit A6L. Created by the iterative threading assembly refinement server (I-TASSER) using the known amino acid sequence from mt-Atp8 encoded protein subunit A6L of the mt7778G/T mutant (a) and wild-type protein (b). Supplemental from (Bär et al., 2013).

The effect of the mutation in the *mt-Atp8* gene has been studied in a variety of genetic environments using various CIS as recipients for the FVB/NJ mtDNA (Yu et al., 2009a, 2009b). These previous studies demonstrated a critical factor in the matching of nuclear genome alleles and mtDNA polymorphisms creating distinct environments that affect the impact of the mtDNA mutation in a unique context. It was shown that the *mt-Atp8* mutation mt7778G/T, resulting in an amino acid substitution in the ATP synthase subunit 8 (A6L), led to an increase in the diabetes incidence when paired to the nuclear genome of NOD/LtJ mice, an increase in the arthritis score when paired to the nuclear genome of (DBA/1JxFVB/NJ)F2 mice as well as B10.Q/J mice and a decrease in the severity of nephritis as well as autoimmune pancreatitis when paired to the nuclear genome of MRL/MpJ mice (Yu et al., 2009b). Other publications could show the influence of this *mt-Atp8* gene mutation in Alzheimer's disease (Scheffler et al., 2012), Diabetes (Weiss et al., 2012a), atherosclerosis (unpublished data),

endotoxic liver failure /sepsis (Eipel et al., 2011), aggravate diet-induced non-alcoholic steatohepatitis (NASH)(Schröder et al., 2016) as well as anxiety (Gimsa et al., 2009)

1.5 **Autoimmune bullous skin diseases**

Immunological conditions in which immune surveillance mechanisms fail and the immune system loses tolerance against self-antigens lead to the development of autoimmune disorders. These sustained immunological pathologies result in chronic inflammatory tissue injury (Murphy et al., 2011). The current consensus of the classification of autoimmune diseases is based on the modified Witebsky's postulates: 1) a specific adaptive immune response directed to an affected tissue or organ; 2) presence of auto-reactive T cells or autoantibodies in the affected organ or tissue; 3) induction of the disease in healthy human or animals by transfer of auto-reactive T cells or autoantibodies; 4) induction of the disease in animals by immunization with autoantigen; 5) immunomodulation-elimination and suppression of autoimmune response leading to amelioration of the clinical manifestations (Damoiseaux and Tervaert, 2002; Hayter and Cook, 2012).

Autoimmune bullous skin diseases (AIBDs) are a rare subgroup of autoimmune diseases, characterized by their organ-specific manifestation at the skin and mucous membranes. AIBDs are separated into two groups defined by the targeted structure of the autoantibodies. In pemphigus diseases autoantibodies target desmosomal proteins in the epidermal compartment whereas pemphigoid diseases the targets are hemidesmosomal proteins at the interface of the dermal-epidermal junction

(DEJ) (Schmidt and Zillikens, 2011, 2013; Sitaru and Zillikens, 2005). Epidermolysis bullosa acquisita (EBA) is an AIBD of the pemphigoid group and characterized by autoantibodies targeting type VII collagen (Col7) located at the sub-epidermal anchoring fibrils of hemidesmosmes (Kasperkiewicz et al., 2016; Ludwig, 2013). Binding of autoantibodies to type VII collagen at the DEJ leads to activation of signaling cascades, inflammation and immune cell recruitment, culminating in dissociation of hemidesmosomal proteins and separation between the epidermis and dermis at the DEJ leading to sub-epidermal blister formation.

1.6 **mtDNA in skin and autoimmunity**

In recent years the importance of mitochondrial function in skin phenotypes has become more apparent. The multi-organ involvement of mtDNA mutations in classical mitochondrial diseases often results in co-morbidities such as a well-documented involvement of skin disorders (Feichtinger et al., 2014). While the mitochondrial metabolism is important for regulation of epidermal homeostasis and differentiation (Hamanaka and Chandel, 2013) mitochondria also become the target of the immune system. Production of anti-mitochondrial auto-antibodies (AMA) has been described in skin autoimmune disorders like scleroderma and pemphigus vulgaris (Kalantari-Dehaghi et al., 2013; Pope and Thompson, 1999). While the pathogenic potential of AMA is still disputed the impact of autoantibody-binding to cells expressing the target autoantigen (i.e. binding of pemphigus vulgaris autoantibodies to Desmoglein 3 at the plasma membrane of keratinocytes) leads to induction of signaling processes and alterations to mitochondrial function (Kalantari-Dehaghi et al., 2013; Marchenko et al., 2010).

Understanding of the importance of mtDNA mutations in autoimmune disorders motivated the recently published study comparing mutation incidence and mtDNA haplogroup in the mitochondrial encoded *MT-ATP8* gen and their association with bullous pemphigoid in a German patient cohort. The study identified specific mtDNA haplogroups enriched in the patient cohort and control cohort respectively (Table 2, Hirose et al., 2015a). Mutations in the *MT-ATP8* gene which have been otherwise commonly described in mitochondrial diseases are associated with autoimmune diseases like multiple sclerosis (Ahari et al., 2007) and psychological and neurological conditions (Auré et al., 2013; Flaquer et al., 2015)

Table 2. SNPs in MT-ATP8 which define R-or I mitochondrial haplogroups in German individuals.* (Hirose et al., 2015)

Gene	Nucleotide position	rCRS	Variant	Amino acid change	Control (n = 548)	Control freq (%)	BP (n = 309)	BP freq (%)	Defining mt haplogroup	OR (95% CI)	P value	mt haplogroup	OR (95% CI)	P value
MT-ATP8	8388	T	C	V>A	3	0.547	0	0	R1a	0.2518 (0.01295–4.894)	0.5570	R*	0.1450 (0.01876–1.121)	0.0390
	8473	T	C	SYN	5	0.912	0	0	R2	0.1596 (0.008792–2.899)	0.1658			
	8557	G	A	A>T	4	0.730	1	0.324	R7b	0.4416 (0.04911–3.970)	0.6591			
	8485	G	A	SYN	1	0.182	1	0.324	I	1.776 (0.1106–28.51)	1.0000	I	5.406 (1.084–26.96)	0.0289
	8519	G	A	E>K	1	0.182	5	1.618	I4	8.997 (1.046–77.40)	0.0252			

rCRS, revised Cambridge Reference Sequence; SYN, synonymous mutation; freq, frequency; mt haplogroup, mitochondrial haplogroup; OR, odds ratio; CI, confidence interval.

These findings represent part of the efforts which have motivated us to investigate the mechanisms by which mutations in mitochondrial genome influence the immune system and the loss of tolerance leading autoimmunity and the effects of mtDNA mutations on aging. Parts of these efforts will be addressed in this work. Central in these investigations is the interaction of cellular function with metabolism.

1.7 **Immunometabolism**

Immune responses are energy demanding processes, are tightly controlled by cell and stimulus-specific profiles and often involve biogenesis. Regulation of bio-energetic processes usually involves multiple signaling pathways that are balanced in equilibrium. Signal transduction induces a shift in this balance affecting the interdependent feedback loops influencing gene expression regulation. The consequences of the majority of cell activation processes affect metabolic equilibria and vice versa (Metallo and Vander Heiden, 2013; Saad et al., 2013; Shanware et al., 2013). Multiple signal transduction pathways lead to a redundant activation of (mitochondrial) biogenesis factors (i.e. PGC-1α) (Fernandez-Marcos and Auwerx, 2011). Transmembrane signaling transduction like cytokine receptor interactions are often facilitated by redundant mechanisms (Kelso, 1994; Ozaki and Leonard, 2002). Intracellular signaling cascades often rely on common mechanism that influence multiple cellular responses (D'Souza et al., 2007; Glancy and Balaban, 2012; Lewis, 2001) leading to an integrated regulation of cellular metabolism and effector responses to extracellular signaling event. The capacity of cellular functions heavily relies on the availability and abundance of metabolites which are of critical importance in the regulation of enzyme activities, feedback loops and as signal transducers (Curi et al., 2016; Saad et al., 2013). Versatile bioenergetic capacities are critical to facilitate metabolic reprogramming and sustain immunological responses (Bengsch et al., 2016; O'Neill et al., 2016b). Mitochondria are often critical to integrate immunological signaling and metabolic adaptation (Duchen, 1999; Martínez-Reyes et al., 2016; Weinberg et al., 2015).

1.8 **Objective**

In recent years it is becoming more apparent that autoimmunity and autoimmune bullous skin diseases are affected by metabolic changes. Mitochondrial DNA polymorphisms are found to be associated with many autoimmune disorders, yet little is known about the functional consequences caused by the SNPs in the mtDNA. The aim of this work is to investigate the influences of the mutation mt7778G>T in the mitochondrial encoded *mt-Atp8* gene on the pathology of autoimmune bullous skin diseases. Here we use EBA as a prototypical example of AIBD to elucidate the underlying molecular mechanisms and pathways by which the *mt-Atp8* mutation shapes the disease phenotype.

2 METHODS

2.1 Mice

The conplastic mouse strain, C57BL/6J-mt$^{FVB/NJ}$ (B6-mtFVB), was previously generated (Yu *et al.*, 2009) and was continuously backcrossed for over 25 generations. C57BL/6J mice were purchased from Jackson laboratory (Bar Harbor, ME, USA). The animal facility was maintained at 21°C on a 12h light- 12h dark- cycle. Mice had *ad libitum* access to filtered water and autoclaved pellet diet (1314, Altromin, Eastern-Westphalia/Lippe, Germany). Animal use and procedures were approved by local authorities of the Animal Care and Use Committee (Kiel, Germany) and performed by certified personnel.

2.2 Generation and isolation of pathogenic anti-Col7c IgG

Antibodies were generated by immunizing rabbits with recombinant fragments of the NC1 domain of mouse type VII collagen (Col7). Sera of these rabbits were then affinity purified using protein G resin affinity chromatography.

2.2.1 Generation of immune sera

The recombinant NC-1 domain of murine type VII collagen, comprising of three different peptides was generated in our laboratory by the technician C. Kauderer according to an established protocol. Rabbit sera were

generated at Eurogentec GmBH (Germany) using New Zealand white rabbits that were immunized with a 250 µg equimolar mixture of the three recombinant proteins suspended in complete Freud's adjuvant by subcutaneous injection. After three boosts in 15 day intervals using the same injection mixture sera of the rabbits were obtained in regular intervals. The sera were used to isolate the IgG fraction which contains the pathogenic rabbit anti-mouse Col7c IgG.

2.2.2 **Affinity purification of total IgG of immunized rabbit sera**

IgG was purified from rabbit sera using protein G resin affinity chromatography. Protein G was used to bind the Fc region of the mammalian Immunoglobulin G.

100 mL rabbit serum was incubated with 5 mL of equilibrated protein G resin on a rocking plate for 1 hour at 4 °C. After washing out the unbound proteins with 2 column volumes of PBS, the IgG fraction was eluted using 0.1 M glycine buffer pH 2.8 and neutralized with 1 M Tris-base (pH>9). The buffer of the IgG fraction was exchanged to PBS and the solution was concentrated using amicon centrifugation tubes with a 30'000 Da filter pore size (Merck Millipore, Darmstadt, Germany). The IgG fraction was adjusted to a concentration of 30 mg/mL.

2.2.3 **Titer determination of isolated anti-Col7 IgG**

Cryo-embedded mouse tail sections were used to evaluate the binding efficiency of the isolated total antibody mix containing anti-Col7c IgG. Serial dilutions of the antibody solution were prepared. Sections on microscopy slides had been kept at -20 °C and were thawed and washed 5 min in PBS at

room temperature. Sections were surrounded with wax pen borders and 50 µL of antibody serial dilutions were distributed to multiple sections. After 60 min incubation in a dark incubation chamber at 4 °C sections were washed 2 times with PBS for 5 min. Next 50 µL of FITC-conjugated swine anti-rabbit IgG/F(ab')2 (1:100 dilution) were added to the sections and incubated for another 60 min at 4 °C. Sections were washed twice for 10 min with PBS in the dark. Excess liquid was removed and sections were mounted in 50% glycerol diluted PBS. To determine the IgG titer, the detection limit of green fluorescence at the dermal-epidermal junction was examined and compared to other batches.

2.3 **Antibody-transfer induced EBA**

Mice were subcutaneously injected with 3 mg of total IgG containing pathogenic rabbit anti-mCol7c IgG in 100 µL of in PBS on day 0 and day 2 of the experiment. After the first antibody injection, clinical signs of disease (erythema, alopecia, erosion, and crust formation) were scored on days 1, 2, 3, 4, 6, 8, 12 and 20 under anesthesia (150 µL/mouse of 10 mg/mL ketamine and 1.5 mg/mL xylazine). Mice were killed on day 20 of the experiment by cervical dislocation.

2.4 **Isolation of lymphocytes/splenocytes**

Animals were killed by cervical dislocation. Organ (lymph nodes or spleen) were removed and placed in a 15 mL Falcon tube filled with 5 mL RPMI1600++++ (RPMI1640 supplemented with 2mM L-Glutamine, 1mM Na-Pyruvate, 1x MEM non-essential amino acids (Gibco, 11140-050),

100 U/mL Penicillin and 100 µg/mL Streptomycin) and kept on ice. Tissue was disrupted by grinding it between two microscope glass slides using the rough surface of the white label area. Disrupted tissue was filtered through a 70 µm cell strainer to separate single cells from tissue debris and washed with RPMI1640++++. The cell suspension was then centrifuged at 400 g for 10 min at 4°C. The supernatant was discarded and the cell pellet was washed with 10 mL PBS and centrifuged again at 400 g for 10 min at 4°C. The supernatant was discarded and the cell pellet was finally resuspended in 2 mL RPMI++++ supplemented with 10% FCS and 50µM 2-Mercaptoethanol (lymphocyte culture medium). Cell number was determined using an improved Neubauer chamber and trypan blue staining to exclude dead cells from the whole counting.

2.5 **Stimulation of lymphocytes**

Anti-CD3 antibody (clone 145-2C11, eBioScience) was diluted to 1 µg/mL in PBS. 100 µL of antibody solution was added to each well and incubated overnight at 4°C. Afterwards wells were washed twice with PBS. To block unspecific binding the coated wells were incubated for 10 min at room temperature with RPMI1640 supplemented with 5% FCS. $4x10^5$-$1x10^6$ cells (lymphocytes/splenocytes) were added to each well in a volume of 100 µL lymphocyte culture medium. Anti-CD28 antibody (clone 37.51, eBioScience) was added to each well at a concentration of 0.2 µg/mL. Cells were stimulated for 24-48 hours at 37°C, 5% CO_2.

2.6 **Flow cytometry**

2.6.1 **Intracellular cytokine staining of leukocytes**

Stimulated cells (see 2.5) were detached from the culture surface by trituration and transfer to 15 mL falcon tubes. Cells were centrifuged for 5 min at 400 g at 4 °C, washed with ice cold PBS and centrifuged again. Approximately 10^6 cells were suspended in 50 µL FACS buffer (2% FCS in PBS), supplemented with anti-mouse CD16/CD32 IgG to a final concentration of 10 µg/mL and incubated for 10 min on ice. Then 50 µL antibody cocktail or isotype antibodies for surface marker staining (see table 1) were added to the cells. Samples were incubated for 10 min on ice. Then 1 mL of FACS buffer was added, samples were mixed and centrifuged at 400 g for 5min at 4 °C. Supernatant was discarded and cell were suspended in 100 µL Fixation/Permeabilization solution (eBioscience), vortexed and incubated for 1 hour at room temperature. Then 1 mL of Permeabilization buffer (eBioscience) was added and samples were centrifuged at 400 g for 7 min at 4 °C. Samples were suspended once more in Permeabilization buffer and centrifuged again as stated above. Supernatant was discarded and pellets were loosed by gentle vortexing. 100 µL of antibody cocktail or isotype antibodies (see table 1) suspended in Permeabilization buffer were added. Samples were vortexed and incubated for 20 min on ice. Samples were supplemented with 1 mL Permeabilization buffer centrifuged at 400 g for 7 min at 4 °C. Samples were washed once more as described and finally suspended in 500 µL FACS buffer. Samples were analyzed on a BD FACSCalibur flow cytometer (BD Biosciences, Heidelberg, Germany) and analyzed using FlowJo.

Table 3. Antibodies for intracellular staining for flow cytometry

purpose	surface marker antibody	conjugated fluorophore	clone	final concentration	isotype
intracellular cytokine staining	anti-mouseCD4 IgG	eFluor 710	RM4-5	1.25 µg/mL	Rat IgG2a
	intracellular marker antibody	conjugated fluorophore	clone	final concentration	isotype
	anti-mouseIFN-g IgG	FITC	XMG1.2	5 µg/mL	Rat IgG1
	anti-mouse/rat IL-17A IgG	PE	eBio17B7	1.25 µg/mL	Rat IgG2a
	anti-mouse IL-4 IgG	APC	11B11	5 µg/mL	Rat IgG1

purpose	surface marker antibody	conjugated fluorophore	clone	final concentration	isotype
staining of Treg cells	anti-mouseCD4 IgG	APC	RM4-5	1.25 µg/mL	Rat IgG2a
	anti-mouseCD25 IgG	PerCP-Cy5.5	PC61.5	2.5 µg/mL	Rat IgG2a
	intracellular marker antibody	conjugated fluorophore	clone	final concentration	isotype
	anti-mouse/rat FoxP3 IgG	Alexa 488	FJK-16s	2.5 µg/mL	Rat IgG2a

2.6.2 **Cell proliferation detection by BrdU incorporation**

Cells that were stimulated for 48 hours (see section 2.5) were supplemented with 5-Bromo-2′-deoxyuridine (BrdU, Sigma Aldrich, Darmstadt, Germany) at a final concentration of 10 µM and incubated for another 12 hours at 37 °C and 5% CO_2. Cells were then collected from the 96 well plate by trituration and transferred into 15 mL falcon tubes supplemented with 1 mL FACS buffer (2% FCS in PBS) and centrifuged at 400 g for 5 min at 4 °C. Approximately 10^6 cells were suspended in 50 µL FACS buffer (2% FCS in PBS), supplemented with anti-mouse CD16/CD32 IgG to a final concentration of 10 µg/mL and incubated for 10 min on ice. Then 50 µL of surface marker antibody cocktail or isotype antibodies were added (see table 2) and samples were incubated for another 15 min on ice. Samples were supplemented with 1 mL FACS buffer, vortexed and centrifuged at 400 g for 5 min at 4 °C. Supernatant was discarded and the

cell pellet was loosened by gentle vortexing. Samples were supplemented with 100 µL BD Cytofix/Cytoperm buffer (BD Biosciences, Heidelberg, Germany) and incubated for 30 min at room temperature. Samples were washed twice by adding 1 mL BD Perm/Wash buffer (BD Biosciences, Heidelberg, Germany), vortexing and centrifugation at 400 g for 7 min at 4 °C. Supernatant was discarded and the final cell pellet was loosened by gently vortexing. Samples were supplemented with 100 µL BD CytoPerm Permeabilization Buffer Plus (BD Biosciences, Heidelberg, Germany), vortexed and incubated for 10 min on ice. Samples were washed twice with BD Perm/Wash buffer as described before. Samples were re-fixed in 100 µL BD Cytofix/Cytoperm buffer for 5 min and washed twice with BD Perm/Wash buffer as described before. Cell pellets were suspended in 100 µL PBS containing 30 µg DNase (Sigma Aldrich, Darmstadt, Germany) and incubated for 1 hour at 37 °C and afterwards washed twice with BD Perm/Wash buffer as described before. The loosened cell pellet was then incubated for 20 min at room temperature with anti-BrdU antibody or isotype antibody in 50 µL BD Perm/Wash buffer. Afterwards samples were washed with 1 mL BD Perm/Wash buffer, centrifuged at 400 g for 7 min at 4 °C and finally suspended in 500 µL FACS buffer. Samples were analyzed on a BD FACSCalibur flow cytometer (BD Biosciences, Heidelberg, Germany) and analyzed using FlowJo.

Table 4. Antibodies for surface marker staining and intracellular staining of BrdU

purpose	surface marker antibody	conjugated dye	clone	final concentration	isotype
intracellular cytokine staining	anti-mouseCD4 IgG	APC	RM4-5	1.25 µg/mL	Rat IgG2a
	anti-CD8a	eFluor710	53-6.7	2 µg/mL	Rat IgG2a
	anti-CD25	PE	PC61.5	2.5 µg/mL	Rat IgG1
	intracellular marker antibody	conjugated dye	clone	final concentration	isotype
	anti-BrdU	FITC	B44	readyl-to-use	IgG1

2.6.3 **MitoSOX/TMRE/MitotrackerGreen/AnnexinV-APC staining of live cells**

Freshly isolated cells or cells that were cultured or stimulated for 24 hours (see section 2.5) were used to determine mitochondrial ROS levels and mitochondrial membrane potential. To detect mitochondrial ROS levels MitoSOX (Life Technologies), a superoxide sensitive dye that preferentially accumulates inside the intermembrane space of mitochondria, was used. The mitochondrial membrane potential (MMP) was determined using TMRE, a dye segregating preferentially into mitochondria dependent on the mitochondrial membrane potential, and was used in conjunction with MitotrackerGreen FM (Life Technologies), a dye that that segregates into mitochondria independent of other factors, to determine the MMP as normalized to the content of mitochondria per cell in lymphocytes.

The cells were detached from the 96 well plate (see section 2.5) by trituration, pooled into a 15 mL falcon tube, supplemented with 1 mL FACS buffer (2% FCS in PBS) and centrifuged at 400 g for 5 min at 4 °C. Cell pellets were suspended in FACS buffer and approximately $5x10^5$ cells in a volume of 100 µL were used for each staining procedure.

2.6.3.1 Mitochondrial ROS

Mitochondrial superoxide was determined by staining approximately $5x10^5$ cells for 10 min at 37 °C with 5µM MitoSOX followed by addition of 2.5 µL Annexin V- APC (BMS306APC, eBioscience) and incubation for 15 min at room temperature. Samples were diluted with 300 µL FACS buffer and analyzed using a BD FACSCalibur flow cytometer (BD Biosciences, Heidelberg, Germany) and analyzed using FlowJo.

2.6.3.2 Mitochondrial membrane potential

Mitochondrial membrane potential was determined by staining approximately $5x10^5$ cells for 15 min at 37 °C with 150 nM TMRE and 100 nM Mitotracker Green FM. Samples were washed with 1 mL FACS buffer and centrifuged at 400g for 5 min at 4 °C. Supernatant was removed and samples were washed and centrifuged again as described before. Final cell pellets were suspended in FACS buffer and analyzed using a BD FACSCalibur flow cytometer (BD Biosciences, Heidelberg, Germany) and analyzed using FlowJo.

2.7 **Microscopy**

2.7.1 **Paraffin sections and hematoxylin & eosin staining**

In the following study, the clinical phenotype of EBA in mice was confirmed by histopathology and direct immunofluorescence technique. Skin biopsies of EBA lesional skin (see section 2.3) were collected after euthanasia. Lesional skin biopsies were fixed in 4% histofix solution and embedded in paraffin blocks. 6 µm skin paraffin sections were cut using a microtome (Leica Mikrosysteme Vertrieb GmbH, Germany) and stained for hematoxylin and eosin (H&E) according to a standard protocol used in the routine histopathological laboratory at the Department of Dermatology, Lübeck. All sections were visualized using the BZ-9000E series Keyence microscope (Keyence Deutschland GmbH, Neu-Isenburg, Germany).

2.7.2 **Cryo Sections and immune fluorescence microscopy**

Frozen tissue pieces were embedded in Tissue-Tek O.C.T. compound cryo fixative (Sakura Finetek, Torrane USA). Sections of 6 µm thickness were cut on a cryo-microtome (Leica CM3050 S, Leica Mikrosysteme Vertrieb GmbH, Germany) and transferred on Superfrost microscope slides. Sections were stored at -20°C until further use.

For indirect immune fluorescence microscopy (IIF) sections were thawed shortly and fixed in ice cold acetone for 20 min. Dried slides were then washed 3 times in TBS-T (50 mM Tris, 150 mM NaCl, 0.05 % (v/v) Tween-20, pH 7.6) for 5 min. Unspecific binding was blocked in TBS-T supplemented with 5% (w/v) biotin-free BSA for 45 min at room temperature. Immediately after, sections were incubated with primary antibodies diluted in TBS-T for 1 hour at room temperature (see table 3). After incubation sections were washed 3 times in TBS-T for 15 min and incubated with Dylight488 conjugated streptavidin for 30 min at room temperature. Sections were washed again 3 times in TBS-T for 15 min.

Sections were incubated with a second antibody (see table 3) diluted in TBS-T for 1 hour at room temperature. After incubation sections were washed 3 times in TBS-T for 15 min and incubated with Dylight594 conjugated streptavidin for 30 min at room temperature. Sections were washed again 3 times in TBS-T for 15 min. After washing the sections were mounted with DAPI Fluoromount G (Southern Biotech, Birmingham, USA) and coverglass was applied to the microscopy slides. Sections were left to dry/solidify overnight. Sections were analyzed with a Keyence BZ-9000E (Keyence Deutschland GmbH, Germany).

Table 5. Biotinylated antibodies and fluorophore-conjugated streptavidin for IIF.

antibody	clone	Isotype	vendor	dilution
Biotin anti-mouse CD3ε Antibody	145-2C11	Armenian Hamster IgG	Biolegend	1:100
Biotin anti-mouse TCR γ/δ Antibody	GL3	Armenian Hamster IgG	Biolegend	1:100
Streptavidin Protein, DyLight 594 conjugate			Life Technologies	1:200
Streptavidin Protein, DyLight 488 conjugate			Life Technologies	1:200

2.8 **Isolation of liver mitochondria**

The liver of euthanized mice was removed, sliced into small pieces and transferred into an Potter-Elvehjem glass homogenizer (Kimble Chase, Rockwood, USA) together with 5 mL ice-cold mitobuffer (0.2 mM EDTA, 0.25 M sucrose, 10 mM Tris-HCl pH 7.8) supplemented with 1x Halt™ Protease & Phosphatase Inhibitor (Life Technologies GmbH, Germany). When using moderate force to homogenize the tissue the clearance between the pestle and tube wall is small enough to break the tissue and plasma membrane yet large enough to leave subcellular compartments (i.e., mitochondria) intact. The tissue is ground to a homogeneous suspension on ice and then centrifuged at 1000 g for 10 min at 4 °C. After the first centrifugation step large particles and debris (i.e. remaining fibrous tissue fragments, nuclei and plasma membrane) are sedimented at the bottom whereas the mitochondria, suspended in a dense sucrose solution and centrifuged at a moderate speed (1000 g) will remain in the supernatant. A layer of fat bodies that were present on the surface of the buffer were removed and the supernatant containing the mitochondria was transferred into a fresh tube and centrifuged again at 1000 g for 10 min at 4 °C to sediment any remaining contamination of larger particles, like nuclei. After these two centrifugation steps at moderate speed the supernatant containing the mitochondria was centrifuged at 10'000 g for 15 min at 4 °C. At this speed the mitochondrial fraction were sedimented leaving

remaining cytoplasmatic components in the supernatant. The mitochondrial pellet was washed with mitobuffer and centrifuged again at 10'000 g for 15 min at 4 °C. Finally, the mitochondria were resuspended in mitobuffer and the protein concentration was determined by BCA protein assay.

2.8.1 **Protein concentration measure by BCA assay**

Protein concentration was assessed using the Pierce™ BCA Protein Assay Kit (Life Technologies GmbH, Germany) according to the manufacturer's instructions. Measurements of mitochondrial content were done in triplicates and compared to a BSA standard curve. An aliquot of mitochondria was diluted 1:25 in mitobuffer and 25 µL were added to a 96 well plate. 200 µL of working reagent (50 parts reagent A and 1 part reagent B) were added to each well, incubated for 30 min at 37 °C and finally absorption was measured using a plate reader at 562 nm wavelength. Mitochondria were snap frozen in liquid nitrogen and stored at -80°C.

2.9 **Determination of ROS in isolated mitochondria**

2.9.1 **Hydrogen peroxide - Amplex Red**

Hydrogen peroxide (H_2O_2) production in isolated mitochondria was measured using the fluorescent properties of AmplexRed dye upon reaction with H_2O_2 and horseradish peroxidase following the method of (Lin et al., 2012). 20 µg of isolated mitochondria were placed into 150 µL ice cold assay buffer (125 mM KCl, 2 mM K_2HPO_4, 20 mM HEPES, 1 mM $MgCl_2$, 100 µM EGTA, 0.025 % BSA, 5 mM succinate and 1.25 µM oligomycin (or 5 mM malate and 5 mM glutamate), (pH 7.0) and the mix was supplemented with

2.5 µM Amplex Red and 0.2 U/mL HRP. Separate reactions were inhibited with 4 µM rotenone. The production of H_2O_2 was assayed kinetically at 37 °C and excitation and emission wavelengths 550 nm and 590 nm, respectively, in a Tecan Infinite M200 PRO spectrophotometer (Tecan Deutschland GmbH, Mainz, Germany).

2.9.2 **Superoxide - MitoSOX**

Superoxide generation in isolated mitochondria was measured using the MitoSOX dye according to Cadwell et al. (Johnson-Cadwell et al., 2007). 20 µg of isolated mitochondria were placed into 150 µL ice cold assay buffer (125 mM KCl, 2 mM K_2HPO_4, 20 mM HEPES, 4 mM $MgCl_2$, 50 µM EGTA, 5 mM malate, 5 mM pyruvate (or 5 mM malate and 5 mM glutamate; or 5 mM succinate) (pH 7.0) and supplemented with 200 nM MitoSOX. Separate reactions were inhibited with 15 µM antimycin A. The production of superoxide detected by MitoSOX was assayed kinetically at 37°C and excitation and emission wavelengths 510 nm and 580 nm, respectively, in a Tecan Infinite M200 PRO spectrophotometer (Tecan Deutschland GmbH, Mainz, Germany).

2.10 **Chemiluminescence detection of ATP and ADP**

2.10.1 **ATP/ADP in isolated cells**

Levels of ATP and ADP were measured using the EnzyLight™ ADP/ATP Ratio Assay Kit (ELDT-100, BioAssay Systems, Hayward, USA) according to the manufacturer's instruction. In short, 10 µL of sample (i.e. 10^4 cells from section 2.3) or ATP standard were placed into an opaque 96 well plate. ATP

reagent was prepared by mixing 95 µL Assay Buffer with 1 µL Substrate, 1 µL Co-substrate and 1 µL ATP Enzyme. 90 µL of the ATP reagent were added to the sample well the plate shortly before measurement. The plate was mixed by gently tapping and after waiting for 1 min to equilibrate the reaction luminescence was measured using a Tecan Infinite M200 PRO spectrophotometer (Tecan Deutschland GmbH, Mainz, Germany). This signal corresponds to the ATP present in the sample volume (RLU A). To allow the measurement of the ADP concentration in the same sample the luminescence reaction of the ATP reaction has to deplete sufficiently during a 10 min waiting period. In the meantime the ADP reagent was prepared by diluting 1 µL in 5 µL dH_2O. Before measuring the ADP reaction a baseline is determined to account for residual activity of the ATP reaction (RLU B). Then the ADP reagent is added to the sample mix and after waiting for 1 min to equilibrate the reagents the luminescence of the ADP reaction is measured (RLU C). The ADP specific signal is determined by subtracting the background activity RLU B from the ADP reaction signal RLU C. The ratio of ADP/ATP can then be calculated as $\frac{RLU\ C - RLU\ B}{RLU\ A}$.

2.10.2 **ATP detection in isolated mitochondria**

ATP in isolated mitochondria was detected using CellTiter-Glo® Luminescent Cell Viability Assay Kit (Promega GmbH, Mannheim, Germany). Assay was prepared on ice and shortly before measurement supplemented with pre-warmed reaction buffer and measured at 37 °C. Total ATP content was determined using the 20µg isolated mitochondria, diluted in 100 µL ice cold assay buffer (125 mM KCl, 2 mM K_2HPO_4, 20 mM HEPES, 1 mM $MgCl_2$, 100 µM EGTA, 0.025 % BSA, pH 7.0). ATP production was determined by diluting 20 µg isolated mitochondria in assay buffer

supplemented with 2.5 mM malate, 2.5 mM glutamate, 2.5 mM succinate, and 3 mM ADP. In separate reactions the ATP synthesis was inhibited by addition of 2.5 µM oligomycin and 2.5 µM FCCP. An ATP standard curve was included using a serial dilution of ATP in the assay buffer. To detect ATP content/production the reaction mix was supplemented with 100 µL CellTiter-Glo reaction buffer (containing a Luciferin/Luciferase mix). Chemiluminescence was detected in a time kinetic manner using a Tecan Infinite M200 PRO spectrophotometer (Tecan Deutschland GmbH, Mainz, Germany).

2.11 **Cellular flux kinetics - extracellular flux analyzer**

Using the Seahorse XF24 Extracellular Flux Analyzer (Agilent Technologies Deutschland GmbH & Co. KG, Waldbronn, Germany) it is possible to measure cellular flux processes by measuring the oxygen and proton concentration in the medium which is in equilibrium with the sample material (cells or mitochondrial particles). Exploiting this system by adding a variety of inhibitor and chemical modulators (i.e. uncouplers) it is possible to determine the activity of the respiratory chain activity to determine mitochondrial oxygen respiration function as well as glycolytic flux as determined by extracellular acidification through lactate coupled proton exocytosis (Chacko et al., 2013; Kramer et al., 2014; Rogers et al., 2011).

2.11.1 **Oxygen Consumption Rates in primary lymphocytes**

When measuring lymphocytes in the extracellular flux analyzer the assay plates are coated with CellTak™ (Corning, Corning, USA). CellTak was diluted to 22 µg/mL in 0.1M Na-bicarbonate buffer, pH 8.0 to activate the sticking properties of the proprietary protein mixture and immediately after 50 µL were pipetted to each well of a 24 well flux assay plate. Plates were coated with CellTak for a minimum of 20 min to ensure sufficient binding of the protein mix followed by 2 washing steps wish distilled water. The plates were then air dried in the laminar flow hood under sterile conditions and stored at 4 °C overnight. The calibration plate was supplemented with flux assay calibrant solution (pH 7.4) and incubated at 37 °C, without CO_2 overnight. The extracellular flux analyzer was switch on one day in advance to allow the machine to stably equilibrate to working temperature.

Inguinal, axillary, brachial and mesenteric lymph nodes were collected from euthanized animals and kept shortly in RPMI1640 medium on ice. Cells were isolated from lymph nodes by disrupting the lymph node integrity rubbing the lymph nodes between the rough, white label areas of two microscopy slides in medium. The disrupted tissue suspension was then filtered through a 70 µm cell strainer. Cell were centrifuged twice at 300 g for 5 min at 4 °C and washed with DMEM. Cell number of single cell suspension was determined using the improved Neubauer chamber and trypan blue staining and adjusted to 1.5 x 10^6 cells per 525 µL.

From 24 wells of the flux assay plate 4 wells were reserved for background correction. The other wells were supplemented with 1.5 x 10^6 cells in 525 µL of DMEM. To facilitate fast attachment of the cells to the coated well surface the assay plate was centrifuged shortly at 40 g at room

temperature. Once 40 g were reached the centrifugation was stopped without breaks to allow a gentle deceleration. The plate was turn by 180° to and centrifuged 80 g at room temperature, without breaks to allow the cells to sediment equally across well surface. Cells were then incubated for 1 hour at 37 °C, 5 % CO_2 to allow the cells to recover from the isolation process. Subsequently the cells were washed with Seahorse assay medium (DMEM, 4.5 g/L glucose, 2mM glutamine, 1 mM pyruvate, without bi-carbonate). Cells were washed by partially removing the medium and leave a remaining volume of 50 µL in each well to prevent detachment of cells and wash the wells twice with 600 µL assay medium. Finally cells were supplemented with Seahorse assay medium to a final volume of 525 µL and cells were incubated at 37 °C without CO_2, for 1 hour.

The injection ports of calibration plate were supplemented with 75 µL as follows:

Port A: 8 µM **oligomycin** (final concentration in assay **1 µM**)

Port B: 10.8 µM **FCCP** (final concentration in assay **1.2 µM**)

Port C: 10 µM each, **antimycin A/rotenone**, (final concentration in assay each **1 µM**)

The calibration plate was placed into the Extracellular Flux Analyzer and calibration was automatically performed to adjust for variations in the calibration plate. After the 1 hour incubation the cells in assay plate were placed into the Extracellular Flux Analyzer and oxygen consumption was measured (Figure 5a). Solutions in the injection ports of the calibration plate were automatically injected subsequently in between measurements to differentiate between basal oxygen consumption rate (OCR), reduced OCR due to inhibition of ATP synthase by oligomycin A, maximum OCR by injection of the uncoupler FCCP, and non-mitochondrial OCR after injection of antimycin A, and rotenone. Basal respiration was determined by

subtracting the non-mitochondrial respiration from the initial, uninhibited respiration. OCR attributed to ATP production was calculated as the difference between basal OCR and oligomycin A inhibited OCR. Spare respiratory capacity was calculated as the difference between basal OCR and FCCP uncoupled maximum respiration. Proton leak was calculated as the difference between oligomycin A inhibited OCR and non-mitochondrial respiration.

2.11.2 **Extracellular acidification rate (Glycolysis assay) in primary lymphocytes**

The initial steps of the glycolysis assay using the extracellular flux analyzer and lymphocytes are identical to the Mitostress assay (see 2.12.1). After pelleting the cells in the assay plate and incubation step for 1 hour at 37 °C and 5% CO_2 cells were washed with modified glycolysis assay buffer (DMEM, 2mM glutamine; without glucose and without bi-carbonate). Cells were further washed and treated as described above (see 2.12.1).

The injection ports of calibration plate were supplemented with 75 µL as follows:

Port A: 80 mM **glucose** (final concentration in assay **10 mM**)

Port B: 9 µM **oligomycin A** (final concentration in assay **1 µM**)

Port C: 1M **2-Deoxyglucose (2-DG)** (final concentration in assay **100 mM**).

The calibration plate was placed into the Extracellular Flux Analyzer and calibration was automatically performed to adjust for variations in the calibration plate. After the 1 hour incubation the cells in assay plate were placed into the Extracellular Flux Analyzer and extracellular acidification rate (ECAR) was measured (Figure 5b). Solutions in the injection ports of the calibration plate were automatically injected subsequently in between

measurements to differentiate between non-glycolytic ECAR, glycolytic activity after injection of glucose, maximum glycolytic activity after inhibition of mitochondrial respiration with oligomycin A, and complete block of glycolysis after injection of 2-DG.

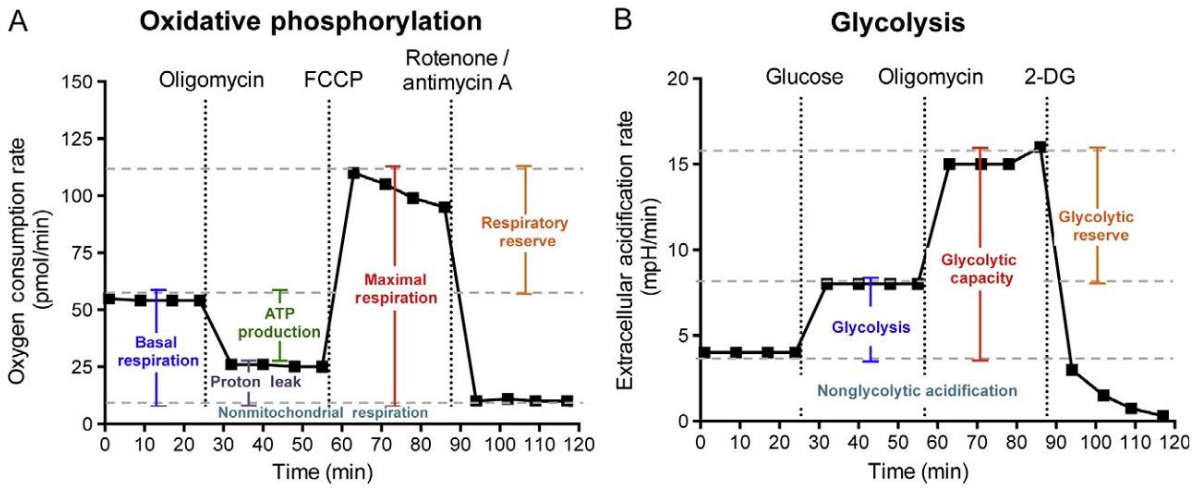

Figure 5. Profiles of mitochondrial respiration and glycolytic activity obtained with the XF Extracellular Flux Analyzer. (A) Graph of the mitochondrial stress test detailing the four key parameters of mitochondrial function (basal respiration, ATP turnover, proton leak, and maximal respiration) with the sequential use of oligomycin (ATP synthase inhibitor), FCCP (mitochondrial uncoupler), and rotenone +antimycin A (complex I and III inhibitors). The difference between the maximal and the basal respirations constitutes the respiratory reserve, the capacity of a cell to generate ATP via oxidative phosphorylation in response to increased demand for energy. Substrate oxidation and cell surface oxygen consumption result in non-mitochondrial respiration. (B) Graph of the glycolytic stress test detailing the parameters of cellular glycolysis (glycolysis, glycolytic capacity, and glycolytic reserve) obtained with the sequential use of glucose, oligomycin (to block mitochondrial respiration and force the cells to rely on glycolysis for ATP production), and 2-deoxyglucose (2-DG, glucose analog and inhibitor of glycolytic ATP production). Glycolytic reserve amounts to the difference between the glycolytic capacity and glycolysis and is indicative of the cellular ability to increase the glycolytic rate upon increased energy demand. Acidification of carbon dioxide, the end product of the TCA cycle, which can be converted to bicarbonate, contributes to non-glycolytic acidification(Pelletier et al., 2014).

2.11.3 **Oxygen Consumption Rate in isolated mitochondria**

The calibration plate was supplemented with flux assay calibrant solution (pH 7.4) and incubated at 37 °C, without CO_2, overnight. The extracellular flux analyzer was switched on one day in advance to allow the machine to stably equilibrate to working temperature. Oxygen consumption of isolated mitochondria was measured in mitochondrial assay solution (MAS: 10 mM succinate, 2 µM rotenone, 70 mM sucrose, 220 mM mannitol, 10 mM KH_2PO_4, 5 mM $MgCl_2$, 2 mM HEPES, 1.0 mM EGTA and 0.2% (w/v) fatty acid-free BSA, pH 7.2 at 37°C).

The injection ports of calibration plate were filled with 50, 55, 60, and 65 µL, respectively, as follows:

Port A: 40 mM **ADP** (final concentration in assay **4 mM**)

Port B: 31.6 µM **oligomycin A** (final concentration in assay **3.16 µM**)

Port C: 40 µM **FCCP** (final concentration in assay **4 µM**)

Port D: 40 µM **antimycin A** (final concentration in assay **4 µM**)

The calibration plate was placed into the Extracellular Flux Analyzer and calibration was automatically performed to adjust for variations in the calibration plate.

Freshly isolated mitochondria (see section 2.9) were diluted in ice cold MAS to a concentration of 0.1 mg/mL and 5 µg (50 µL) were pipetted into the 24 well Extracellular Flux Assay plate and centrifuged at 2000 g for 20 min at 4 °C. After centrifugation 450 µL pre-warmed (37 °C) MAS buffer was added to each well and the assay plate was placed into the Extracellular Flux Analyzer and oxygen consumption rate was measured. Solutions in the injection ports of the calibration plate were automatically injected subsequently in between measurements to differentiate between. Addition

of ADP induces respiration (state 3 respiration) by facilitating the depletion of the mitochondrial membrane potential through complex V mediated ATP synthesis. Addition of oligomycin A inhibits complex V and respiration decreases to a quasi-exhausted state (state 4o respiration). Addition of FCCP uncouples respiration and APT synthesis by artificially depleting the mitochondrial membrane potential, thus allowing unrestricted activity of the respiratory chain (state 3u respiration).

2.12 **OXPHOS enzyme activity measurements**

Enzyme activity of the oxidative phosphorylation system (respiratory chain enzyme complexes and ATP synthase) and citrate synthase were measured in isolated mitochondria using a Tecan Infinite M200 PRO spectrophotometer (Tecan Deutschland GmbH, Mainz, Germany). Mitochondrial samples were frozen and thawed three times to disrupt membrane integrity and make exogenous substrates more accessible to the enzyme complexes. Reactions were measured in a volume of 200 µL in triplicates. To determine the specific activity of substrate use for each enzyme complex specific inhibitors were used to distinguish unspecific substrate use and OXPHOS enzyme activity. Methods were adapted from (Barrientos et al., 2009; Spinazzi et al., 2012)

2.12.1 **Complex I, rotenone-sensitive NADH-decylubiquinone oxidoreductase**

The reaction mix for complex I consisted of 50 mM Potassium phosphate (pH 8), 2.5 mg/mL BSA, 250 µM KCN, electron donor NADH (150 µM) and

the electron acceptor decylubiquinone (50 µM). Inhibition of complex I activity was measured in separate reaction by the addition of 20 µM rotenone. Reactions are started by pipetting 10 µg of isolated mitochondria into an empty well and adding the reaction mix to that well. Complex I activity was measured at 37°C in a volume of 200 µL by following the conversion of NADH to NAD^+ and the consequent decrease in absorbance at 340 nm over a time of 15 min.

2.12.2 Complex III, antimycin A-sensitive decylubiquinol-cytochrome c reductase

To measure Complex III activity the electron donor decylubiquinone has to be prepared fresh by reducing the stock solution of decylubiquinone (Spinazzi et al., 2012). To accomplish this 100 µL of 10 mM decylubiquinone were supplemented with a minimal amount of lithium borohydride (the amount of a pipet tip dipped in the powder, ~1 mg). Additionally 4 µL of 0.1 M HCl were added to catalyze the redox reaction. The reaction produces elemental H_2 which rises in bubbles and the solution changed color from yellow to transparent indicating the successful reduction of decylubiquinone to decylubiquinol. The solution was then centrifuged at 10'000 g for 1 min to sediment reaction side product the supernatant was transferred to a clean reaction tube and the reduced decylubiquinol was stabilized by addition of 4 µL of 1 M HCl centrifuged again at 10'000 g for 1 min.

The reaction mix for complex III consisted of 50 mM Potassium phosphate (pH 7.8), 500 µM KCN, 10 µM rotenone, 250 µM EDTA, the electron acceptor oxidized cytochrome c (50 µM), and the electron donor decylubiquinol (50 µM). Inhibition of complex III activity was measured in separate

reaction by the addition of 37.5 µM antimycin A. Reactions are started by pipetting 10 µg of isolated mitochondria into an empty well and adding the reaction mix to that well. Complex III activity was measured at 37°C in a volume of 200 µL by following the conversion of oxidized cytochrome c to reduced cytochrome c and the consequent increase in absorbance at 550 nm over a time of 3 min.

2.12.3 **Complex IV, Cyanide-sensitive cytochrome c oxidase**

To measure complex IV activity cytochrome c was reduced shortly before measurement (Spinazzi et al., 2012). To a stock solution of 1 mM cytochrome c (dissolved in 20 mM potassium phosphate buffer, pH 7) a few crystals of sodium dithionite (the amount of a pipet tip) were added and the color of the solution turned from brown to orange-pink. Effective cytochrome c reduction was checked by calculating the ratio of the absorbance values at 550 nm versus 565 nm of this solution at a final concentration of 20 µM. A ratio greater than 6 indicates effective cytochrome c reduction.

The reaction mix for complex IV consisted of 10 mM Potassium phosphate buffer (pH 7.0), and the electron donor reduced cytochrome c (50 µM). Inhibition of complex IV activity was measured in separate reaction by the addition of 500 µM potassium cyanide. Reactions are started by pipetting 10 µg of isolated mitochondria into an empty well and adding the reaction mix to that well. Complex IV activity was measured at 37°C in a volume of 200 µL by following the conversion of reduced cytochrome c to oxidized cytochrome c and the consequent decrease in absorbance at 550 nm over a time of 3 min.

2.12.4 **Complex V, oligomycin-sensitive F_0F_1-ATP Synthase activity**

To measure Complex V activity the reverse reaction of the ATP Synthase activity is combined in a coupled enzyme reaction setup to allow the measurement of the ATP synthase activity using spectrophotometer techniques. The isolated mitochondria were uncoupled using CCCP allowing the reverse reaction of the ATP synthase. ATP is hydrolyzed to ADP which is used by the pyruvate kinase (PK) to convert phosphoenolpyruvate (PEP) into pyruvate which is subsequently converted by the lactate dehydrogenase (LDH) to lactate thereby converting NADH to NAD^+. LDH and PK are added in excess making the ATP synthase of the isolated mitochondria the rate limiting enzyme in this reaction and thus allowing the correlation of NADH/NAD^+ conversion with the ATP synthase reverse activity of ATP hydrolysis.

The reaction mix for complex V consisted of 10 mM Tris-HCl (pH 8.0), 2.5 mg/mL BSA, 4 mM $MgCl_2$, 10 mM KCl, 2 µM CCCP, 18.5 µM antimycin A, 2.5 µM rotenone, 2 mM PEP, 1 mM ATP, 0.8 units LDH, 0.8 units PK, and 200 µM NADH. Inhibition of complex V activity was measured in separate reaction by the addition of 25 µM oligomycin. Reactions are started by pipetting 10 µg of isolated mitochondria into an empty well and adding the reaction mix to that well. Complex V activity was measured at 37°C in a volume of 200 µL by following the conversion of NADH to NAD^+ and the consequent decrease in absorbance at 340 nm over a time of 15 min.

2.12.5 **Citrate synthase**

The reaction mix for citrate synthase activity assay consisted of 10 mM Tris-HCl (pH 8.0), 0.2 % (w/v) Triton X-100, 100 µM DTNB, 300 µM Acetyl-CoA and 500 µM oxal acetic acid. Mitochondria were added to the reaction mix and the baseline was determined for 3 min. To start the reaction oxal acetic was added to the mix and the activity was determined at 30°C by following the increase in absorbance at 412 nm resulting from the reaction of DTNB with the free thiol group of coenzyme A. CoA became available after the citrate synthase combined the acetyl-group of acetyl-CoA with the oxal acetic acid to produce citrate.

2.13 **Protein isolation and electrophoresis techniques**

2.13.1 **Denatured protein isolation for SDS-PAGE/Western blot**

250 µg (50 µL) of isolated mitochondria were mixed with 450 µL RIPA buffer (150 mM sodium chloride, 1.0% NP-40, 0.5% sodium deoxycholate, 0.1% SDS, 50 mM Tris, pH 8.0) supplemented with Pierce™ Protease and Phosphatase Inhibitor (Thermo Fisher Scientific) and 1g/g ratio of protein/detergent (n-Dodecyl β-D-maltoside; DDM; Sigma Aldrich). Samples were vortexed and incubated for 30 min on ice. Samples were then centrifuged at 16'000 g for 20 min at 4 °C. The supernatant was collected and the concentration of soluble protein was measured by BCA assay (see section 2.8.1). 20 µg of soluble mitochondrial protein were mixed with 1/5 sample volume of 5x SDS loading dye (0.25M Tris-HCl, 15 % SDS, 50 % glycerol, 25 % β-mercaptoethanol, 0.01 % bromophenol blue, pH 6.8). Samples were heated at 50 °C or 95 °C depending on which western blot antibody detection was performed later on.

2.13.2 **SDS-PAGE**

Sodium dodecylsulfate-polyacrylamide gel electrophoresis was performed using precast 4-20% ExpressPlus™ PAGE Gels (GenScript, USA). 20 µg of solubilized, denatured proteins, mixed in loading dye, were loaded to the gels. Spectra Multicolor BR protein ladder (Thermo Fisher Scientific) was used as a size marker. Electrophoresis was performed using MOPS running buffer (50 mM Tris, 50 mM MOPS, 0.1 % SDS, 1 mM EDTA). Gels were separated at 50 V for 15 min and another 1-2 h at 100 V.

2.13.3 **Western Blot**

Proteins separated in SDS-PAGE were transferred to 0.45 µm nitrocellulose membranes (Bio-Rad Laboratories GmbH, Munich, Germany) by electroblotting. Gels were placed on nitrocellulose membranes and both were sandwiched between one layer of Whatman paper and one layer of sponges. Electroblotting was performed at 4 °C with WET transfer buffer (15 mM Tris, 66 mM glycine, 20 % ice cold methanol) at a constant voltage of 70 V for 1.5 hours.

Membranes were removed and shortly rinsed in distilled water. Then membranes were incubated for 10-30 sec in Ponceau S staining solution (0.2 % Ponceau S, 30 % trichloracetic acid, 30 % sulfosalicylic acid) to reversibly stain the total protein content on membranes to evaluate blotting efficiency and protein content for each sample lane. The membranes were de-stained in TBS-T (50 mM Tris-HCl, 150 mM NaCl, 0.05 % Tween-20, pH 7.6) to remove unspecific staining until sharp protein

bands were visible which were then quantified using a QUANTUM ST4 1100 imaging system (Vilber Lourmat Deutschland GmbH, Eberhardzell, Germany). Afterwards, membranes were completely de-stained by extended incubation in TBS-T. Thereafter, membranes were blocked by incubation in 5% (w/v) BSA in TBS-T at 4 °C, overnight on a rocking plate. Membranes were then incubated with primary antibodies (see table 4) diluted in 1% (w/v) BSA TBS-T for 2 hours at room temperature on a rocking plate. After washing 3 times 10 min with TBS-T, the membranes were incubated with HRP-conjugated secondary antibodies (see table 4) diluted 1:2000 in 1% (w/v) BSA TBS-T for 2h at room temperature on a rocking plate. Membranes were then washed 3 times for 10min in TBS-T and rinsed shortly in TBS (50 mM TrisHCl, 150 mM NaCl, pH 7.6). Antibody binding was visualized using the Clarity™ Western ECL Substrate (Bio-Rad Laboratories GmbH, Munich, Germany) to detect HRP induced luminescence. Signals were detected using a CCD camera documentation system (FUSION Fx7, Vilber Lourmat Deutschland GmbH, Eberhardzell, Germany)) applying variable exposure times. Images were evaluated using Image J v1.50b (Schneider et al., 2012). Detected protein signals were normalized to the total protein content per lane (Ponceau S stained membrane).

Table 6. Antibodies for western blot analysis

Antibody	Dilution	Clone	Vendor
MitoProfile® Total OXPHOS Rodent WB Antibody Cocktail	1:1000	20E9DH10C12, 21A11AE7, 13G12AF12BB11, 1D6E1A8, 15H4C4	MitoScience
Rabbit, anti-mouse IgG antibody, HRP conjugate	1:2000	polyclonal	DAKO
Rabbit, anti-mouse-*mt-Atp8* antibody	1:1000	polyclonal	Biorbyt
Goat, anti-rabbit-IgG antibody, HRP conjugate	1:2000	polyclonal	DAKO

2.13.4 **CN-PAGE and in-gel ATP synthase activity**

Clear native polyacrylamide gel electrophoresis (CN-PAGE) was performed using precast 3-12% SERVAGel™N Native Gel (SERVA Electrophoresis GmbH, Heidelberg, Germany) precast vertical gels. Samples of isolated mitochondria that were kept in high sucrose containing mitobuffer (see above) were centrifuge at 20'000 g for 10 min at 4 °C to collect the mitochondria. The pellets were solubilized using solubilization buffer (50 mM NaCl, 2 mM 6-aminocaproic acid, 1 mM EDTA, 50 mM Bis-Tris, 10 µM PMSF pH 7.6) containing digitonin at a ratio of 1 g/g detergent to sample-protein-content. Samples were vortexed and kept on ice for 15 min to facilitate the release of proteins and complexes from the mitochondrial membranes. Samples were then centrifuged at 20'000 g for 30 min at 4 °C. Supernatants were supplemented with 10% (v/v) glycerol and 0.01% (v/v) Ponceau S and loaded to the gel pockets.
Electrophoresis was performed using a cathode buffer containing 50 mM Tricine, 15 mM Bis-Tris (pH 7), and an anode buffer containing 50 mM Bis-Tris (pH 7). Samples were separated for 15 min at 100 V, 2 h 200V with the current ranging between 5-15 mA.

After separating the native proteins the gels were rinsed in distilled water and were pre-incubated in 270 mM glycine, 35 mM Tris-HCl (pH 8.4) for 3 h at room temperature. To measure the ATP synthase activity of native enzyme complexes in the polyacrylamide gel, the gels were incubated in 270 mM glycine, 35 mM Tris, 8 mM ATP, 14 mM $MgSO_4$, 0.2% $Pb(NO_3)_2$ (pH 8.4). The ATP is hydrolyzed by the ATP synthase complexes and $Pb(NO_3)_2$ reacts with the phosphate to form a white precipitate. Reactions were stopped after approximately 1 h by incubating the gels in 50 % methanol in

water for 30 min followed by 30 min incubation in distilled water. Gels were then documented by densitometry using a QUANTUM ST4 1100 imaging system.

Afterwards gels are de-stained overnight in 50 % methanol and 10 % acetic acid. Then the total protein separated on the gel was visualized by incubation in 0.2% Coomassie G-250 dye in 50 % methanol and 10 % acetic acid for 1-2 h. Unspecific Coomassie staining was removed by incubation in 10 % methanol and 10 % acetic acid. Coomassie stained bands in the gel were documented using a QUANTUM ST4 1100 imaging system. Images were evaluated using Image J v1.50b (Schneider et al., 2012). In gel ATP synthase activity was normalized to the total protein content per lane (Coomassie stained gel).

2.14 **Mitochondrial DNA copy number**

The number of mtDNA copies per cell was determined using the NovaQUANT™ Mouse Mitochondrial to Nuclear Ratio kit (Novagen, Merk Millipore, Darmstadt, Germany). Mitochondrial encoded genes (*trLEV* and *12S rRNA* gene) and nuclear encoded genes (*BECN1* and *NEB*) were amplified and quantified by qPCR as per manufacturer's instructions.

2.15 **Indirect calorimetric cage analysis**

Mice were allocated to the experimental room system 4 days before measurements to let them acclimatize. Activity of mice was monitored using open-circuit indirect calorimetry systems (PhenoMaster System™, TSE, Bad Homburg, Germany) for additional 5 days. The average values of records taken during last 3 days were used for the analysis. Calorimetric measurements were normalized to the metabolic weight (weight raised to 0.75) as a commonly used normalization (Arch et al., 2006). O_2 consumption, CO_2 production, food/water intake, and locomotor activity were continuously monitored. The respiratory exchange ratio (RER) was estimated from the ratio of CO_2 produced (mL/h) to O_2 consumed (mL/h) and can be used as an indication for the type of energy source that is being used by the organism. A reference framework for the RER has been derived from known values for a variety of substrates. A low RER of 0.7 indicates lipids as a predominant source of energy, while a RER of 1 indicates carbohydrates as predominant oxidation product for energy production. Energy expenditure (EEx) was calculated as following: $(3.941 + 1.106 \times RER) \times O_2$ consumed and normalized to body weight (Weir, 1949). The energy expenditure (EEx) estimates how much energy is released by the organism derived from the expected contribution of substrates to the oxygen and carbon dioxide flux.

2.16 **Metabolic analysis of fatty acids**

Tissue samples of wild-type mice and *mt-Atp8* mutant mice (5 animals per sex per strain) of brain, liver, ear, lymph node, thymus as well as blood plasma were collected and analyzed in cooperation with the Hemholtz Center Munich. Samples were analyzed using the Absolute*IDQ*® p150 Kit (Biocrates Life Sciences AG, Innsbruck, Austria) for reference substances and sample handling was performed with assistance of Hamilton robotics and detected using LC-MS/MS AB-Sciex mass spectrometer at the Hemholtz Center Munich, Genome Analysis Center, Metabolomics Core Facility. List of metabolites shown in (

Table 11, see section 6.1). Data was normalized based on probabilistic quotient normalization (PQN) (Di Guida et al., 2016) .

2.17 **Skin microbiome assessment by next generation sequencing**

2.17.1 **Sampling of microbial skin swabs**

Swabs were collected from wild-type mice (B6) and *mt-Atp8* mutant mice (B6-mtFVB) which were kept under standard housing conditions (see section 2.1). Mice were handled separately using a fresh pair of sterile gloves for each mouse to minimize cross contamination.

Swabs were collected using Catch-All sample collection swabs (Biozym Scientific GmbH, Germany) and SCF-1 solution (50 mM Tris, 1 mM EDTA, 0,5% Tween-20, pH 8.0; Teknova, USA). The swab was removed from the outer packing and immersed into a 1.5 mL tube filled with 600 µL sterile SCF-1 solution. The moistened swab was rubbed on the mouse ear for

approximately 30 seconds, rubbing both inner and outer side of the ear. The swab tip was then placed into the 1.5 mL tube filled with SCF-1 solution and the upper part of the swab was removed by breaking it away. Samples were stored for later DNA isolation at -20 °C. The following preparation was supported by Stephanie Dahl.

2.17.2 **Extraction of DNA from the mouse ear swabs**

The DNA was extracted from the swab samples with the PowerLyzer® UltraClean® Microbial DNA Isolation Kit (MO BIO Laboratories, USA).

The swabs tubes were thawed overnight at 4 °C and shortly vortexed for 15 sec. The tubes were briefly centrifuged and supernatant (600 µL) were transferred into a clean 2 mL Collection Tubes. Internal isolation controls were included by running the isolation procedure in parallel with fresh/sterile SCF-1 solution in an additional 2 mL Collection Tube. The tubes were then centrifuged for 3 min at 10'000 g at room temperature. The supernatants were discarded and pellets containing the bacteria were resuspended in 300 µL MicroBead Solution followed by gentle vortexing. The resuspended bacterial suspensions were transferred into a MicroBead Tubes together with 50 µL MD1 solution and 20 µL protein kinase K. The MicroBead Tubes were vortexed for 15 sec and incubated for another 10 min at 70 °C to loosen bacterial cell wall components. Bacteria lysis was further facilitated by mechanical lysis with microbeads using a Precellys24 Homogenizer (Bertin Instruments, Rockville, USA), shaking the tubes twice for 15 sec at 5000 rpm. Tubes were centrifuged for 30 sec and supernatants (300-350 µL) were transferred into new Collection Tubes containing 100 µl MD2 solution. The tubes were shortly vortexed to mix the solutions and incubated for 5 min at 4 °C. After incubation, tubes were centrifuged for

1 min at 10’000 g to precipitate the non-DNA organic and inorganic material. The supernatants (400-450 µL) were transferred into a new 2 mL Collection Tubes containing 900 µL MD3 solution and shortly vortexed. 700 µL of the mixture were then loaded onto a Spin Filter and centrifuged at 10’000 g for 30 sec. The flow-through was discarded and the process was repeated with the remaining mixture. To wash, 300 µL of MD4 solution were added to the Spin Filter and samples were centrifuged for 30 sec at 10’000 g. Flow-through was discarded and the Spin Filter Tubes were centrifuged for 1 min at 10’000 g to remove remaining traces of MD4 solution. The Spin Filters were placed in new 2 mL Collection Tubes and 40 µL of MD5 solution was pipetted onto the middle of the Filter. The tubes were centrifuged for 30 sec at 10’000 g to elute the isolated DNA from the filter. The eluted DNA was stored at 4°C, if the next step was performed within the next days or at -20°C.

2.17.3 **Library preparation for 16S rDNA NGS sequencing**

Individual bacterial DNA samples were amplified with primers commonly used in microbiome studies for amplification of the V1 and V2 region of the bacterial 16S rRNA gene (Table 7). These primers additionally contain unique identification extensions to allow the simultaneous sequencing in the final library. After initial amplification samples are purified, quantified, and pooled together in several steps to ensure an equal molar ratio between all samples.

Table 7. Illumina sequencing primers for amplification of V1 and V2 region of the bacterial 16S rRNA gene containing the actual primer sequence preceded by sequencing primer, unique multiplex identifiers (MID) and adaptor sequences. MIDs comprise a unique combination of 8 nucleotides to allow the identification of sequences belonging to a particular biological sample).

	Adaptor sequence	MID (8nt)	Sequencing primer	16S rRNA gene primers
Forward (27F)	5'-AAT GAT ACG GCG ACC ACC GAG ATC TAC AC	1 to 16	TATGGTAATTGT	AGAGTTTGATCCTGGCTCAG-3'
Reverse (338R)	5'-CAA GCA GAA GAC GGC ATA CGA GAT	A to X	AGTCAGTCAGCCT	GCTGCCTCCCGTAGGAGT-3'

2.17.4 **Amplification of the 16S rRNA gene fragment by PCR**

Samples were assigned to primer pairs with unique combinations of Multiplex identifiers (MIDs) to allocate individual sequences to the respective sample after the library has been sequenced by NGS.

Isolated DNA from the swab samples was used undiluted. First, 1 µL of the template DNA was place into a well of a 96 well PCR plate. Then 4 µL (8 picomoles) of each primer was pipetted into the wells according to the individual assignments for each sample. The remaining 16 µL of master mix were added to each well as outlined in Table 8.

Table 8. Reaction mix for PCR amplification of V1-V2 region 16S rRNA gene

Reaction component	Volume	Final concentration/ amount
RT-PCR Grade Water	10.25 µL	
5X Phusion HF Buffer	5 µL	1X
dNTPs (10 mM each)	0.5 µL	200 µM each
Forward Primer (27F - 2 µM)	4 µL	0.32 µM
Reverse Primer (338R - 2 µM)	4 µL	0.32 µM
Template DNA	1 µL	
Phusion Hot Start II DNA	0.25 µL	0.5 units
Total volume	25 µL	

The plate was covered with an adhesive PCR plate seal, gently vortexed, and spun down. PCR amplification in the Thermocycler was performed using the following program:

Table 9. PCR program for V1-V2 16S rRNA gene amplification.

Cycle step	Temperature	Duration	
1. Initial denaturation	98°C	30 sec	
2. Denaturation	98 °C	9 sec	
3. Annealing	50 °C	1 min	30
4. Extension	72 °C	1 min 30 sec	cycles
5. Final extension	72 °C	10 min	
6. Hold	12 °C	∞	

2.17.5 **Quantification and normalization of PCR amplicons**

PCR products of the 16S rRNA gene fragments with an estimated size of approximately 450 bp were separated by agarose gel electrophoresis. Agarose gels (1.5 %) prepared with TAE buffer (40 mM Tris-HCl, 20 mM acetic acid, 1 mM EDTA) containing SYBR® Safe DNA Gel Stain (SYBR, Thermo Fisher Scientific) were loaded with 5 µL sample supplemented with 1 µL 6X Loading Dye (Thermo Fisher Scientific). As a fragment size marker, 1 µL GeneRuler 100 bp Plus DNA Ladder (Thermo Fisher Scientific) were mixed with 1 µL 6X Loading Dye and 4 µL ddH_2O and loaded on the gel.

The electrophoresis was performed at 120 V for 5 min and continued at 110 V for another 70 min. PCR fragment intensity was then assessed with the QUANTUM ST4 1100 imaging system (Vilber Lourmat Deutschland GmbH,

Eberhardzell, Germany). The fragment bands were analyzed with the software Quantum Capt v16.04 (Vilber Lourmat Deutschland GmbH, Eberhardzell, Germany). Using the known concentration of the size marker bands, the relative concentration of the PCR products was estimated in relation to the 500 bp marker band. Samples that were analyzed on the same gel image were then pooled together at equimolar ratios using aliquots from the original PCR products. These initial subpools of the PCR product were separated on another agarose gel as described above to separate residual primer and potential off-target fragments. The desired 16S rDNA gene fragments were cut out from the gel with X-TRACTA Tips placed into 2 mL tubes and purified using the GeneJET Gel Extraction Kit (Thermo Fisher Scientific). To this end samples were supplemented with 400 µL of Binding Buffer and incubated for 10 min at 60 °C to melt the gel slices. 400 µL of 100% isopropanol were added and the mixtures mixed by vortexing. Up to 800 µL of the mixtures were loaded to the GeneJET purification columns and the columns were centrifuged at 12'000 g for 1 min. The flow-through was discarded and the step was repeated with the remaining sample mixture. Another 100 µL of Binding Buffer was added and the tubes were centrifuged for 1 min at 12'000 g. The flow-through was discarded and 700 µL of Wash Buffer was added to each column. Samples were centrifuged at 12'000 g for 1 min and the flow-through discarded. To remove residual buffer from the filter, the column was centrifuged again for 1 min, turned by 180° and centrifuged for another minute. The GeneJET purification columns were placed into clean 1.5 mL reaction tubes and 15-20 µL of Elution Buffer were added to each column. Samples were centrifuged at 12'000 g for 1 min. The eluate was placed another time on the column membrane and centrifuged a second time to increase the yield. The purified DNA was stored at -20 °C until further use.

The PCR fragments were then quantified with the Qubit® dsDNA HS Assay Kit (Thermo Fisher Scientific). The Qubit working solution was prepared by diluting the Qubit® dsDNA HS Reagent 1:200 in Qubit® dsDNA HS Buffer. For each sample and standard 200 µL of the working solution were used. 10 µL of both standards (S1 and S2) were mixed with 190 µL of the working solution, respectively. The standard solutions were measured in the Qubit® Fluorometer to calibration further the measurements. Samples were diluted 1:100 in working solution in a final volume of 200 µL and measured in the Qubit® Fluorometer. Subpools were then all pooled together at equimolar ratio and comprised all sampled of the NGS library.

2.17.6 **16S rRNA gene NGS library purification and preparation**

Subsequently, the library pool was purified using the Agencourt® Ampure® XP Kit (Beckman Coulter). Using 100% ethanol and ultra-pure water, a 75 % Ethanol solution was freshly prepared. 40 µL of the library were placed into a 96-well plate. The AMPure XP suspension (containing magnetic beads that binds DNA) was resuspended thoroughly and 70 µL of the solution were added to the sample well and mix by pipetting followed by 10 min incubation period. The reaction plate was then placed onto an AgencourtSPRIPlate 96 Super Magnet Plate for 2 min to collect the DNA bound beads at the plate wall. The sample solution was aspirated and discarded. The plate was removed from the magnetic stand and 200 µL of 75 % ethanol were added, mixed and the plate was incubated for 30 sec. The plate was placed onto the magnetic stand for another 2 min to collect the DNA bound beads at the plate wall and the ethanol was removed. This washing step was repeated once more. The beads in the plate were left to dry for 5 to 10 min before the plate was removed from the magnetic stand.

20 µL elution buffer were added to the sample and mixed thoroughly. The sample was incubated for 2 min to dissociate the DNA from the magnetic beads. The plate was placed once again onto the magnetic stand to collect the magnetic beads to the plate wall during a 1 min incubation period. The solution containing the DNA was transferred to a new 1.5 mL reaction tube.

After the purification, the samples were analyzed with the Agilent High Sensitivity DNA Assay Kit using the Agilent 2100 Bioanalyzer to determine the average fragment size and concentration of the 16S rRNA gene fragment NGS library. To this end the kit components were used to prepare the gel-dye mix by pipetting 15 µL of the dye concentrate into a vial with the High Sensitivity DNA gel matrix. The vial was vortexed and the gel-dye mix was transferred into a tube with the spin filter. The spin filter was centrifuged for 10 min at 2240 x g and room temperature. The filter was discarded and 9 µL of the gel-dye mix were applied to the High Sensitivity DNA chip onto a well, marked by a bold G. Using a syringe and the chip priming station, pressure was applied to the well on the chip for 60 sec. This step was repeated for additional wells on the chip for additional DNA samples or the High Sensitivity DNA ladder. Each well was supplemented with 5 µL of the High Sensitivity DNA marker. 1 µL of the High Sensitivity DNA ladder was added to the well which was marked with the ladder symbol. Into each sample well 1 µL of sample was pipetted. The chip was then vortexed for 60 sec at 2400 rpm, inserted into the 2100 Agilent Bioanalyzer and the run was started.

The 16S rRNA gene fragment NGS library was quantified using the Qubit® dsDNA HS Assay Kit as described above (section **Quantification and normalization of PCR amplicons** and an aliquot of the library was dilute to a concentration of 4 nM.

2.17.7 **Final preparation of the library**

The 16S rRNA gene fragment NGS library was prepared to be analyzed on a MiSeq desktop sequencer (Illumina, San Diego, USA) using the MiSeq Reagent Kit v3 (Illumina, San Diego, USA). The reagent cartridge and the HT1 buffer were removed from the freezer and thawed at room temperature prior to the library preparation. 5 µL of the 16S rRNA gene fragment NGS library (sample library) were mixed with 5 µL of 0.2 N NaOH solution, briefly vortexed and incubated for 5 min at room temperature to denature the DNA. 990 µL of ice-cold HT1 buffer was added and the library was further diluted in HT1 buffer to the final concentration of 15 pM (450 µL denatured DNA library + 150 µL HT1 buffer).

An internal quality control, the PhiX control library was prepared by mixing 2 µL of the 10 nM PhiX library with 3 µL of 10 mM Tris-HCl (pH 8.5) containing 0.1 % Tween 20. The 4 nM PhiX control library was denatured by mixing 5 µL PhiX control library with 5 µL 0.2 N NaOH, vortexed briefly and centrifuged at 280 x g for 1 minute and incubated for another 5 min at room temperature. Then 990 µL of the HT1 buffer were added and the PhiX control library was diluted to a final concentration of 12.5 pM (375 µL of 20 pM denatured PhiX control library + 225 µL HT1 buffer).

The sample library and the PhiX control library were then combined by mixing 540 µL of the 15 pM denatured sample library with 60 µL of the 12.5 pM denatured PhiX control.

The custom-made primers, 27F, Index and 338R, were diluted to 0.5 µM by adding 3 µL of 100 µM primer stock solution to 597 µL HT1 buffer.

On the reagent cartridge, the reservoir positions 12, 17, 18, 19 and 20 were opened with a tip. The read1-primer contained in position 12 was taken out

and transferred into a new tube. 60 µL of the read1 primer were combined with 540 µL of the 27F primer (0.5 µM). The diluted and denatured sample library (containing 1.25 pM PhiX control library) was transferred into the reservoir position 17. The 27F primer mixed with the read1-primer was loaded to position 18, the index primer to position 19, and the 338R primer (0.5 µM) was loaded to reservoir position 20 of the reagent cartridge.

The Flowcell was cleaned and inserted into the MiSeq desktop sequencer. The bottle with the Incorporation buffer and the reagent cartridge were inserted into the MiSeq. A digital sample sheet was uploaded to MiSeq software application and the run was started and sequencing data was transferred to the BaseSpace Sequence Hub platform provided by Illumina.

2.17.8 **NGS analysis of microbiome data**

Data processing and statistical analysis of NGS data was performed and coordinated by Axel Künstner and assisted by Stephanie Dahl.

The 16S rRNA gene fragment NGS library was processed using the software mothur v1.38.0 (Schloss et al., 2009) using the SILVA database (Quast et al., 2013; Yilmaz et al., 2014), usearch v8.1.1861(Edgar, 2010) and vsearch v2.02 (Rognes et al., 2016) and Fasttree v2.1 (Price et al., 2010). The data processing workflow is outlined in Figure 6. Sequencing data sorted according to the MIDSs and converted to fastq-files using the internal MiSeq conversion, and fastq-files were downloaded for further processing. Forward and reverse reads of the same DNA string were merged together and reads with a bad quality score were removed. Chimeric sequence artifacts that occurred during PCR amplification by annealing of two template DNA strands from different bacterial origins, which form non-

naturally-occurring 16S rRNA fragments, were detected using tools included in the vsearch pipeline and were removed. After keeping just one copy of each sequence fragment (dereplication) sequences were clustered into operational taxonomical units (OTUs) by assigning taxonomic relations to all sequences based on sequence similarity using a 97% cut-off. Additionally a phylogenetic tree was calculated from all OTUs identified in the processed NGS library data.

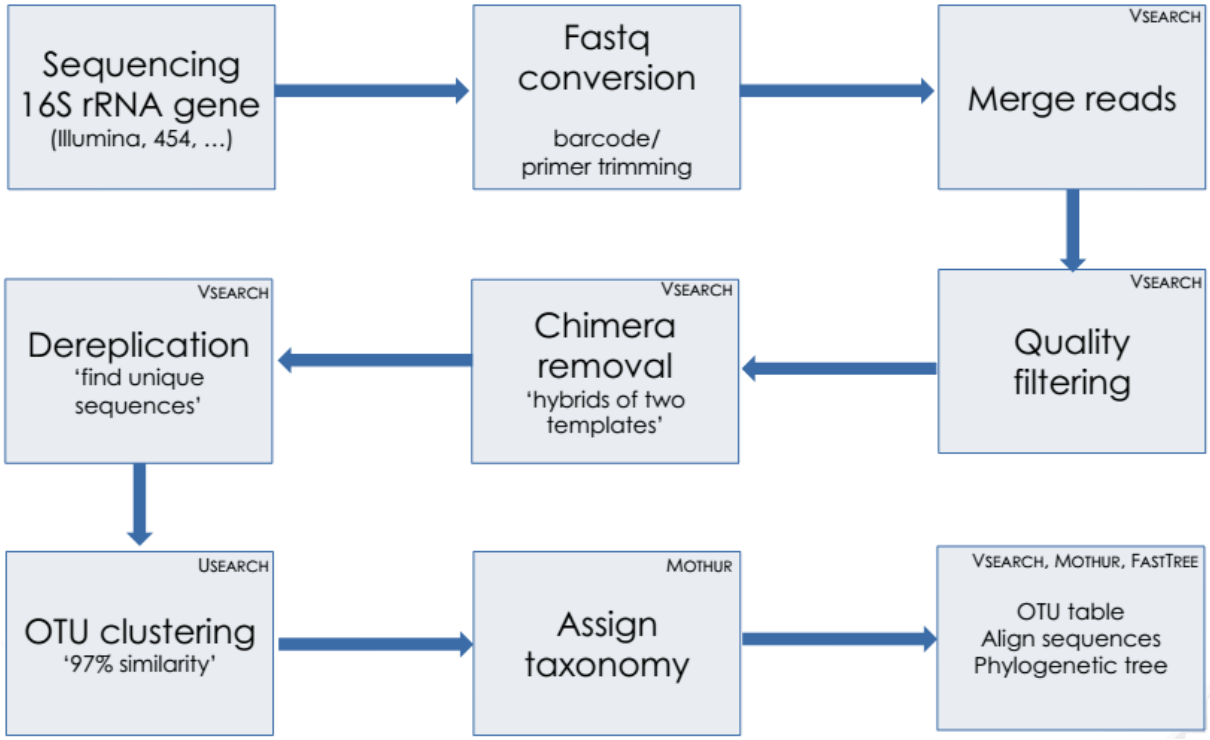

Figure 6. 16S rDNA NGS Data preprocessing pipeline. Sequencing data obtained from the sequencing of the V1-V2 region of bacterial 16S rDNA region on an Illumina MiSeq. Data is filtered through several steps and clustered into operational taxonomic units (OTUs).

Samples sizes were rarefied to an even sequencing depth (random subsampling of 10'000 contigs without replacement). Samples that had less than the minimum contig count of 10'000 were discarded. Additionally, singleton OTUs were removed. Singletons are OTUs, which occurred once in one of the samples and are commonly considered to be at the noise threshold and do not contribute to the further analysis. The phylum

abundance and the family abundance in the different groups were plotted and compared based on abundance.

To assess alpha diversity in the individual samples Chao1 and Shannon indices were calculated and tested for significance differences using Wilcoxon rank-sum test (Hill, 1973; Whittaker, 1960).

To compare beta-diversity between samples Bray-Curtis dissimilarity as well as unweighted UniFrac and weighted UniFrac were calculated. Significant difference in theses metrics between the strains were evaluated using permutational based multivariate analysis of variance (perMANOVA; R: Adonis command) or constrained analysis of principal coordinates (CAP; R: Capscale) using the R package 'vegan' (Oksanen et al., 2016). Tests were performed with 999 permutations. Data visualization was done in R applying Principle coordinate analysis (PCoA) on Bray-Curtis dissimilarities or using Capscale ordination.

Indicator species analysis was performed using the R package 'indicspecies' (Bakker, 2008; Cáceres and Legendre, 2009; Dufrene and Legendre, 1997).

2.18 **Statistical analysis**

Statistical analysis was performed using GraphPad Prism v6. A p-value of <0.05 was considered significant. Data is presented as mean±SEM (mean values and standard error of mean) unless otherwise stated. Applied statistical methods are mentioned in the respective figure and tables.

Using the preprocessed data further analysis was conducted in the R software environment v3.3.1 (R Core Team, 2016).

3 RESULTS

3.1 The *mt-Atp8* mutation ameliorates the pathogenesis in the antibody-transfer EBA model

Since it was already reported that mutations in the *mt-Atp8* gene are associated with AIBDs in human, the work presented here, aimed to identify causative influences of the mutation and identifying mechanisms by which it alters disease phenotypes. Using conventional C57BL/6J (B6) wild-type mice and conplastic C57BL/6J-mt$^{FVB/NJ}$ (B6-mtFVB) mice carrying a single nucleotide mutation in the *mt-Atp8* gene (Table 1) it was possible to correlate the influence of the mutation in a controlled genetic environment.

To investigate the influence of a point mutation in the *mt-Atp8* gene in AIBD, the mouse model of EBA was applied and disease was induced in mice by repeated injection of pathogenic antibodies directed against type VII collagen. Injection of the pathogenic antibodies replicates the development of typical disease hallmarks comparable to the human disease phenotype, i.e. erythema, inflammation, erosion, and crust formation, in both strains. The disease phenotype is significantly reduced in the *mt-Atp8* mutant strain compared to the wild-type strain as indicated by an ameliorated clinical score based on affected body surface area (Figure 1).

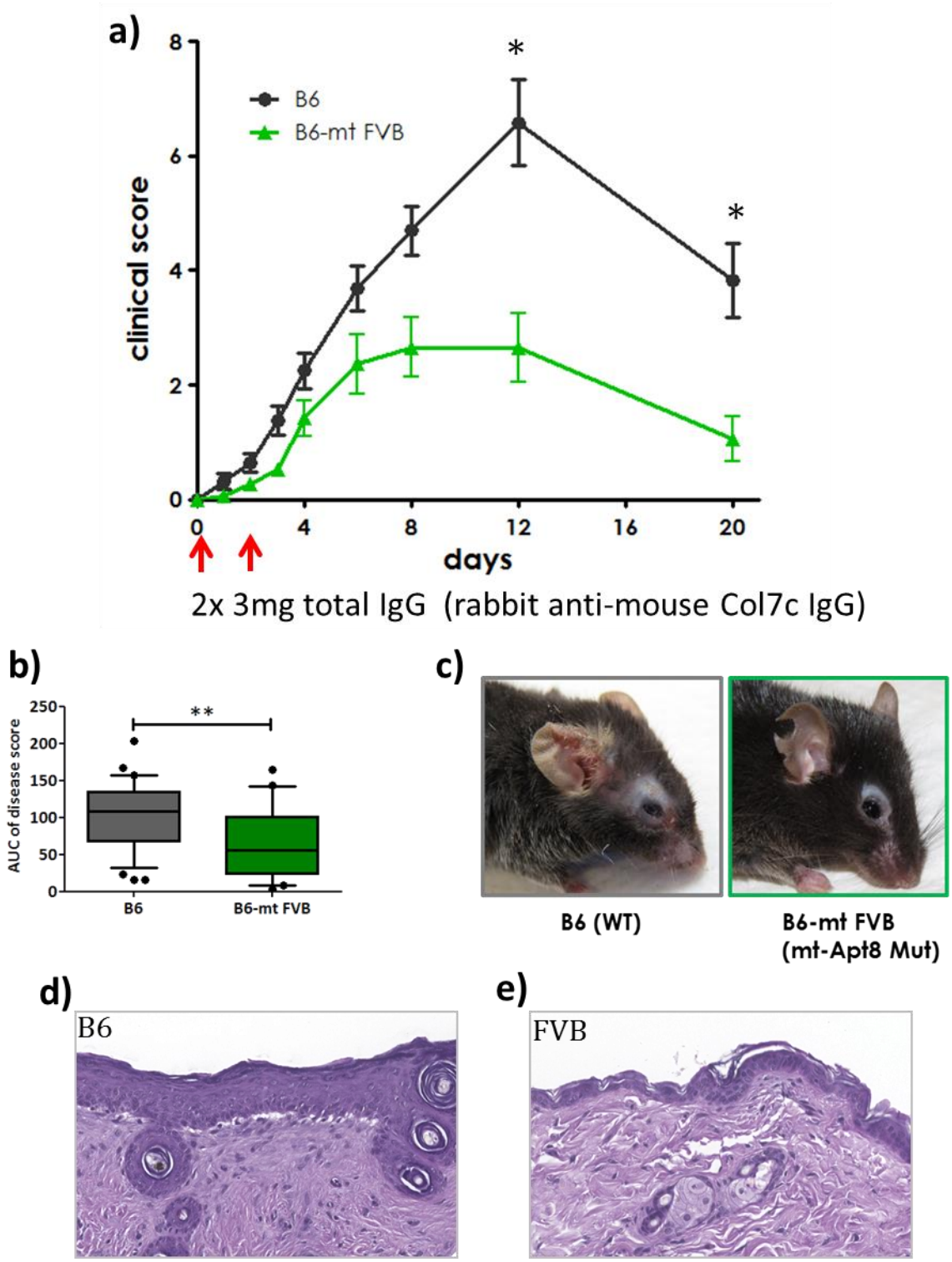

*Figure 7. Effect of the mt-Atp8 mutation in the antibody-transfer induced EBA model. Mice were subcutaneously injected with 2x 3mg pathogenic anti-murine type VII collagen antibodies on day 0 and day 2 respectively. Clinical disease phenotype was scored as the percentage of erythema, erosion, alopecia and crust formation developing on the body surface. Red arrows indicate the time points at which antibodies were injected into the mice. Disease progression over time (a) and area under the curve (AUC) of disease score (b). (c) representative clinical phenotype of disease severity at day 12 of wild-type and mutant mice. (d-e) representative images of HE stained skin sections of inflamed skin in the EBA model from B6 and B6-mtFVB mouse skin at the end of the experiment. (a) * p-value <0.05 2-way ANOVA; (b) ** p-value <0.01 student's t-test.*

3.2 **Immune cell phenotypes**

Although the historical interpretation of the EBA disease phenotype attributes a major role for the disease severity to neutrophil granulocytes function, a screening of neutrophil cell function between the mutant and wild-type strain did not show any significant differences (data unpublished, personal communication Prof. Ibrahim). It was concluded that the neutrophil cell function that was not sufficiently altered by the *mt-Atp8* mutation could not conclusively explain the reduced disease severity. A cell type with previously neglected importance therefore must play a crucial role in modulating the immune response and inflammation processes seen in the B6-mtFVB strain.

As it was already well known in the literature that T cells rely on mitochondria-dependent signaling mechanisms during activation (Kamiński et al., 2013; Sena et al., 2013a; Weinberg et al., 2015) and that mitochondrial metabolic control influences T cell function (Bengsch et al., 2016; O'Neill et al., 2016b; Scharping et al., 2016) the function of T cells was evaluated in the B6-mtFVB strain. We set out to investigate whether this cells type was sufficiently affected by the *mt-Atp8* mutation to influence inflammatory processes.

3.2.1 ***mt-Atp8*** **mutation alters T cell function**

Evaluation of the lymphocyte stimulation reveals a significant influence of the *mt-Atp8* mutation on T cell phenotypes. Upon in vitro stimulation of lymph node derived T cells with anti-CD3/anti-CD28 antibodies, cells of the *mt-Atp8* mutant strain (B6-mtFVB) demonstrate reduced proliferation rate and reduced percentage of IL-17^+ and IL-4^+ T cell populations (Figure 8a,b).

While mitochondrial membrane potential shows a trend of decrease in the *mt-Atp8* mutant strain (Figure 8c), the mitochondrial ROS levels showed a more complex pattern. Unstimulated lymphocytes had an increased mitochondrial ROS level as detected with MitoSOX by flow cytometry. However, stimulated cells of the B6-mtFVB strain had a significantly reduced mitochondrial ROS level (Figure 8d).

Recent unpublished data demonstrates an important role of T cell populations in the pathogenesis of the antibody-transfer induced EBA model, as knockout and depletion of T cells and T cell subpopulations ameliorates the disease severity (personal communication Prof. Ralf Ludwig).

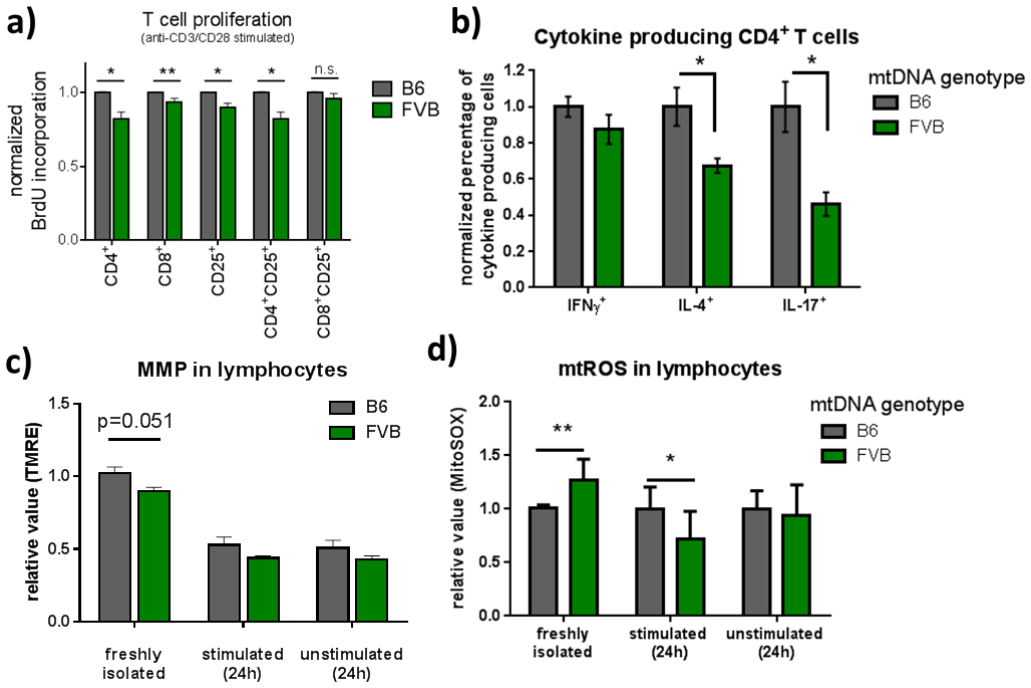

*Figure 8. Lymphocyte phenotype. Cells were isolated from lymph nodes of mice and stimulated in vitro with anti-CD3/anti-CD28 antibodies for 24-48 hours to determine cell proliferation, Cytokine expression, mitochondrial membrane potential (MMP), and mitochondrial ROS production (mtROS). Cell proliferation was determined by incubating the stimulated cells with BrdU for overnight and detected by anti-BrdU antibodies (a). Cytokine producing T cells were evaluated using intracellular antibody-staining (b). Mitochondrial membrane potential (MMP) was determined with TMRE dye (c). Mitochondrial ROS was determined with MitoSOX dye (d). Cells were measured by flow cytometry.B6: wild-type strain; FVB: mt-Atp8 mutant strain * p value < 0.05, ** p value < 0.01, student's t-test.*

3.2.2 *mt-Atp8* influence on immune cell homeostasis in the skin

Following the observation of an altered immune cell response between *mt-Atp8* mutant and wild-type strains, we sought to investigate the distribution of skin resident immune cells. Not only the function of immune cells but also their energy state and the consequential life expectancy define the steady state of the immune milieu in any given tissue, i.e. the skin barrier. The distribution of immune cells at the skin barrier is influenced by the exposure to environmental stimuli as well as metabolic status of the organism itself. The postulated effect of the mtDNA mutation in the *mt-Atp8* gene on the metabolism of B6-mtFVB strain therefore may alter the equilibrium of the immune milieu at the skin barrier and alter the distribution of immune cells. To investigate this, T cell populations were stained in skin sections of healthy mice and their distribution in the skin was evaluated. As mouse skin is characterized by a resident population of γδT cells in the epidermal skin layer this population made up the majority of T cells in the skin of healthy mice. The comparison of the amount of T cells per length of the epidermal skin section revealed a decrease in the density of T cells in the skin, indicating a potential alteration in the equilibrium of the immune milieu of the skin.

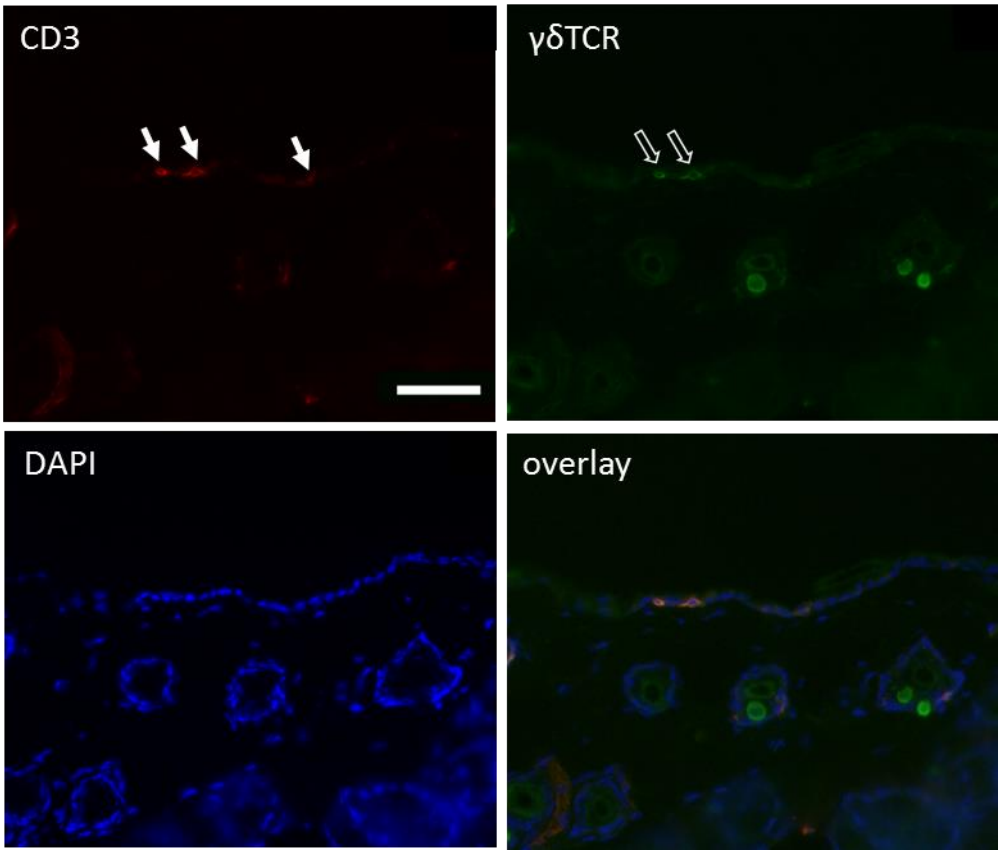

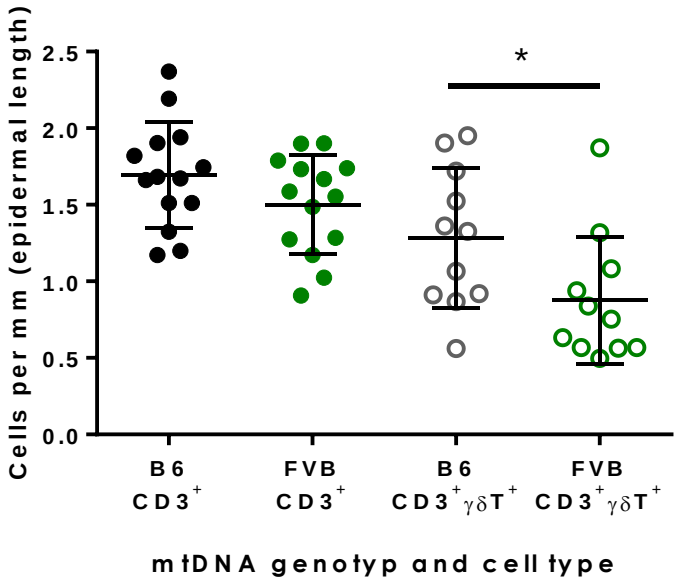

*Figure 9. T cells in skin total CD3⁺ cells, CD3⁺gdTCR⁺ T cells. Cryo-sections of ears were incubated with primary biotin-conjugated antibodies: anti-mouse CD3ε IgG, anti-mouse TCRγ/δ IgG and fluorophore-labelled with streptavidin-Dylight594 or streptavidin-Dylight488. Sections were counterstained with DAPI and mounted using Fluoromount. Cell counts in the epidermal layer were normalized to the length of the epidermis on the sections. Scale 100 µm. Data points represent median cell counts from all images from individual mouse ears, with 5-20 images evaluated for each animal. Mean values and standard deviation. Solid arrows CD3⁺ cells; open arrows gdTCR⁺ cells. * p-value <0.05, Wilcoxon rank-sum test.*

3.3 **Mitochondrial phenotypes**

It was already published that the *mt-Atp8* mutation in mice affects a variety of disease models and alters cellular phenotypes. To elucidate how the mutation of a protein involved in the oxidative phosphorylation system and part of a metabolically essential cellular organelle could influence inflammatory processes the influence of the mutation on the mitochondrial function was investigated in more detail.

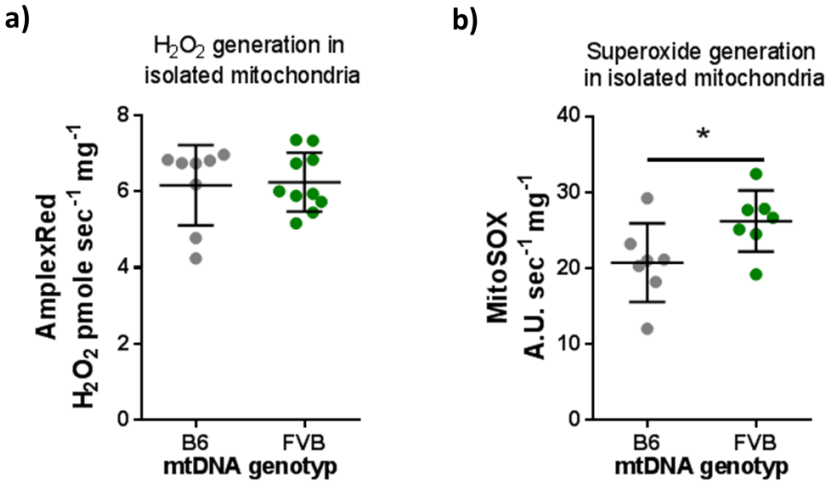

*Figure 10. ROS production in isolated mitochondria. Mitochondria were isolate from liver tissue and the generation of reactive oxygen species was determined under conditions of substrate excess. Hydrogen peroxide (H_2O_2) generation was determined by the increase of AmplexRed fluorescence upon the conversion of H_2O_2 by the horseradish peroxidase (HRP)(a). Superoxide radical production was determined by the increase of fluorescence of the mitochondrial superoxide-selective fluorophore MitoSOX (b). A.U., arbitrary units. * p-value<0.05, student's t-test.*

Mutations related to mitochondrial proteins, especially the ones affecting the oxidative phosphorylation system (OXPHOS) affect the production of reactive oxygen radical/species (ROS). Mitochondrial ROS (mtROS) is also a

crucial factor in immunological signaling processes (Akira et al., 2013; Kamiński et al., 2013; Sena et al., 2013a; Zhou et al., 2011). Therefore, mutation-induced alterations in the mtROS equilibrium are of importance to the interplay of mitochondria and immune signaling. While isolated mitochondria do not show alteration in the production of hydrogen peroxide, the generation of superoxide under excess substrate conditions is significantly increased in the *mt-Atp8* mutant strain (Figure 10).

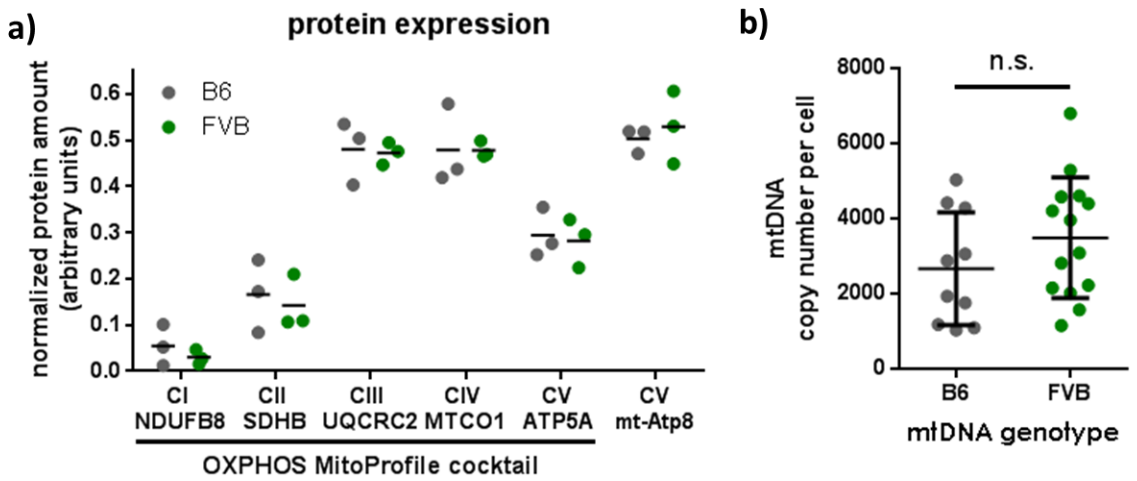

Figure 11. Western blot analysis of OXPHOS subunits and mtDNA copy number analysis. (a) Isolated mitochondria were separated by SDS-PAGE, blotted onto nitrocellulose membranes and proteins were labelled with MitoProfile antibody cocktail (Mitosciences), and anti-mouse-mt-Atp8 antibody (Biorbyt) followed by corresponding HRP conjugated secondary antibodies and measured by chemiluminescence detection using a CCD imaging system. Protein signals were normalized against the total protein content in the sample lane. MitoProfile antibody cocktail allows the simultaneous detection of complex I (CI) subunit Ndufb8, Complex II (CII) subunit Sdhb, Complex III (CIII) subunit Uqcrc2, Complex IV (CIV) subunit mt-Co1 and Complex V (CV) subunit Atp5a. (b) mtDNA copy number in liver determined by qPCR reactions quantifying mtDNA as well as nuclear DNA encoded genes using NovaQUANT™ Mouse Mitochondrial to Nuclear Ratio kit. B6: wild-type strain, FVB: mt-Atp8 mutant strain. n.s. : no significance, Student's t-test.

Analysis of protein expression of OXPHOS system subunits by Western blotting did not show significant differences between B6 wild-type and conplastic B6-mtFVB mice (Figure 11a). Similarly, mitochondrial DNA copy

number, assessed by qPCR of mtDNA and nDNA encoded genes, did not showed differences between wild-type and mutant strain (Figure 11b).

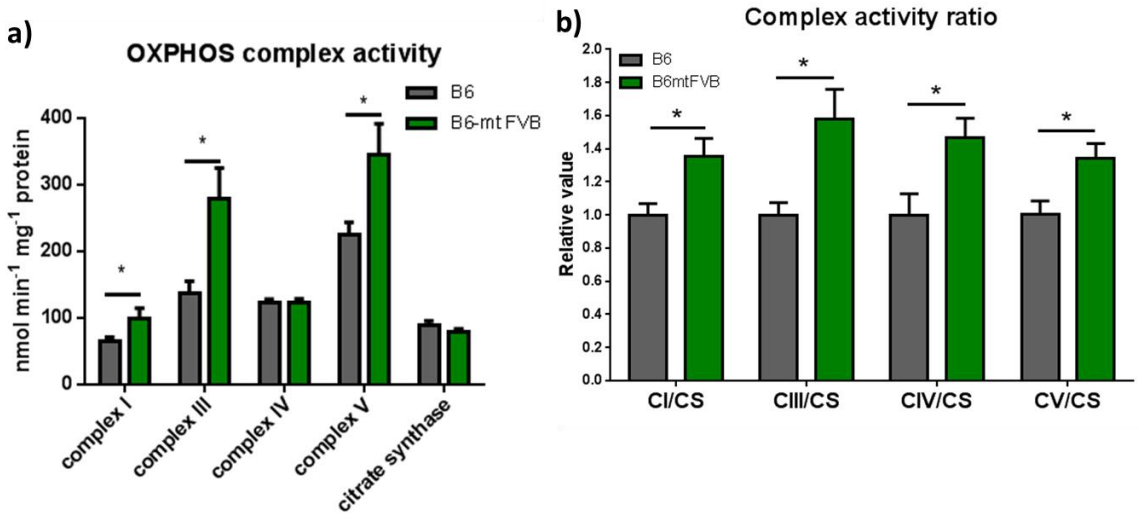

*Figure 12. OXPHOS enzyme activity in isolated mitochondria. Enzyme activities were assessed in a plate based method using a spectrophotometer. Enzyme activities for complex I, III, IV and V were assessed at 37°C and citrate synthase (CS) activity was measured at 30 °C. Enzyme reaction were performed using enzyme specific electron donor and acceptor pairs as well as using enzyme specific inhibitors in parallel reactions to confirm the specificity of the reaction. Measured enzyme activity (a) and ratio of enzyme activity compared to the citrate synthase (b). * p-value <0.05 student's t-test, p-value adjusted by Benjamini-Hochberg correction for multiple testing.*

Measurement of the enzyme activity of the OXPHOS enzyme complexes indicates a systematic alteration in the respiration complexes (Figure 12). The ATP synthase, Complex V of the OXPHOS system, which in the B6-mtFVB mouse strain comprises the mutated A6L subunit encoded by the *mt-Atp8* gene shows an altered enzyme activity not only for complex V but all other measured enzyme complexes as well.

Isolated enzyme activities are measured *in vitro* under excess substrate conditions, thus regulatory mechanisms by intrinsic feedback loops *in vivo* are circumvented. The results hint at regulatory mechanisms that limit the catalytic activity of the OXPHOS system *in vivo*. Additionally the organization of enzyme complexes potentially influences the efficiency of

the respiration system by facilitating “substrate channeling”. The formation of individual OXPHOS complexes into supercomplexes therefore affects *in vivo* efficiency as well as accessibility to artificial substrate *in vitro*.

Wittig *et al.* described a mechanism by which the lack of *mt-Atp8* expression alters the suprastructural organization of the ATP synthase complex which provide further insight to the findings of Bornhövd *et al.* who described the importance of ATP synthase oligomerization for cristae formation, membrane potential and consequently the organization of other supercomplexes in the OXPHOS system (Bornhövd et al., 2006; Wittig et al., 2010). The proposed model provides an appealing hypothesis for a mechanism by which the mutation in the *mt-Atp8* gene influences the supramolecular structures of the OXPHOS system and affects its catalytic activity in opposing directions *in vivo* and *in vitro*: namely by reducing the stability of ATP synthase supracomplexes and thereby reducing efficiency *in vivo* and providing improved substrate accessibility for individual enzyme complexes *in vitro*. To address this issue the ATP synthase oligomer state in wild-type and *mt-Atp8* mutant mice mitochondria was assessed by clear native polyacrylamide gel electrophoresis (CN-PAGE) and in gel enzyme activity analysis. Although the shift is only minor the comparison of wild-type and *mt-Atp8* mutant mice indicates a shift from oligomeric ATP synthase complexes towards the monomeric state of the ATP synthase in the *mt-Atp8* mutant strain (Figure 13).

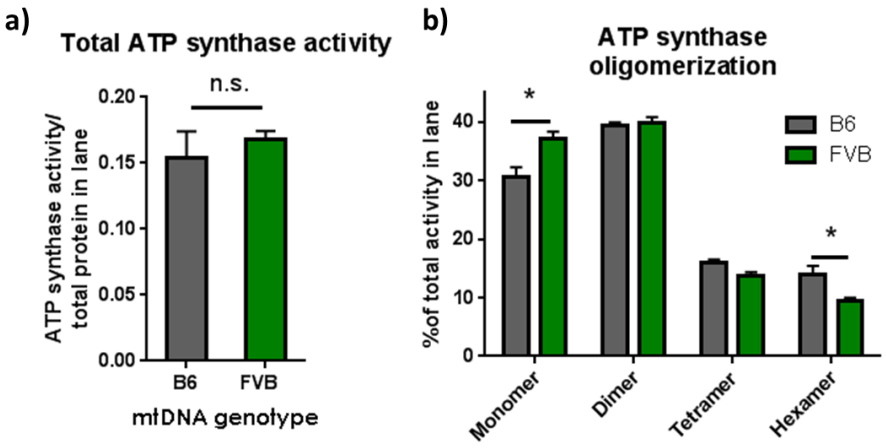

*Figure 13. In-gel ATP synthase activity to identify oligomer states. Mitochondria were solubilized with digitonin to release oligomeric supercomplexes which were then separated by clear native polyacrylamide gel electrophoresis. The ATP synthase supercomplexes, separated by size, were assayed by in gel ATP hydrolysis activity and quantified by densitometric imaging. (a) Total ATP synthase activity normalized to the total protein content in the sample lane, n.s.: no significance, student's t-test. (b) ATP synthase activity of different oligomeric states as percentage of total ATP synthase activity in the sample lane, * p-value<0.05, 2-way ANOVA.*

3.4 **Energy flux and metabolism**

3.4.1 **Respiration and energy flux in lymphocytes**

The energy metabolism is an essential part of any cellular response to external stimuli and mitochondrial compartment plays a central role in facilitating metabolic demands and providing ATP for the cell.

The mt7778G>T mutation in the *mt-Atp8* gene affects a major enzyme complex in the OXPHOS system and the mutation alters a variety of cellular responses. To get a better understanding how the mutation influences so many phenotypes, further investigations focused on potential alterations in the energy metabolism.

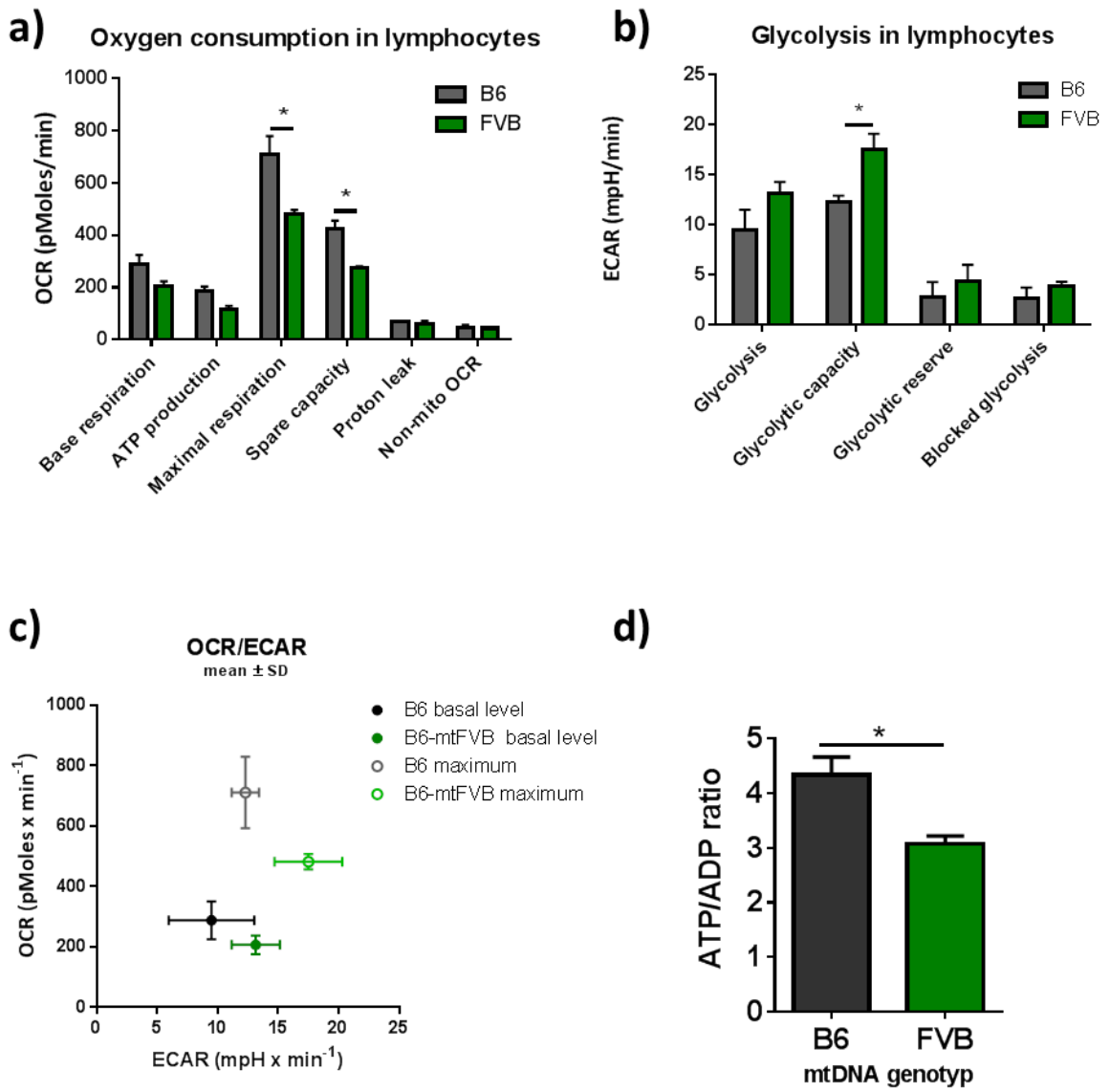

*Figure 14. Metabolic flux analysis of oxygen and protons. Oxygen consumption and extracellular acidification measurements were performed using freshly isolated lymph node cells in a Seahorse XF24 Extracellular Flux Analyzer (Agilente Technologies). (a) To derive multiple aspects of mitochondrial respiration function specific OXPHOS inhibitors were sequentially injected as follows: 1 µM oligomycin, 1.3 µM FCCP, and 1 µM each of rotenone and antimycin A. (b) To assess glycolytic activity substrates and inhibitors were injected sequentially as follows: 10 mM glucose, 1 µM oligomycin, 100 mM 2-deoxyglucose. (c) Plot showing basal levels and maximum capacity of respiration and glycolysis, respectively. (d) ATP/ADP ratio in lymphocytes was measured by enzymatic chemiluminescence reactions. B6: wild-type strain; FVB: mt-Atp8 mutant strain. (a) & (b) *p-value<0.05, 2-way ANOVA; (d) * p-value<0.05, student's t-test.*

Measurement of mitochondrial respiration in isolated lymphocytes revealed a significant decrease in the utilization of oxygen and mitochondrial oxidative phosphorylation to produce energy in the *mt-Atp8* mutant strain (Figure 14a).

The assessment of the glycolytic flux rate in isolated lymphocytes reveals an increased glycolytic capacity which indicates a compensatory mechanism that seems to partially counterbalance the decreased OXPHOS utilization in the *mt-Atp8* mutant mice (Figure 14b), while the overall energy balance in the mutant strain is decreased, compared to the wild-type (Figure 14d).

3.4.2 **Respiration and energy flux in isolated mitochondria**

Oxygen consumption measurements were performed using isolated mitochondria to analyze the activity and plasticity of the oxidative phosphorylation system independent of any cellular regulation processes. Similar to the observations in lymphocyte respiration, isolated mitochondria of the *mt-Atp8* mutant strain demonstrate a slight reduction in maximal respiration (state 3u) as well as a decrease in the spare capacity (Figure 15). The respiration of isolated mitochondria under excess substrate conditions only partially reproduces the observation made in intact cells indicating an influential role of metabolic balance and flux inside the cellular environment.

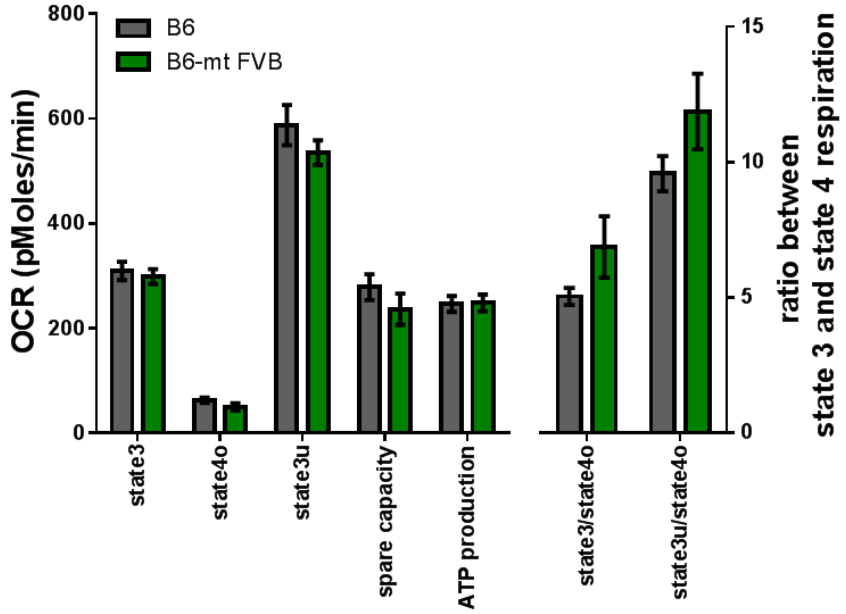

Figure 15. Oxygen consumption measured in isolated mitochondria. Isolated mitochondria (5 µg/well) were suspended in MAS buffer and pelleted on the bottom of the assay plate by centrifugation. After addition of pre-warmed assay buffer the mitochondria were immediately measured in the flux analyzer. Mitochondrial respiration states and functions were evaluated by sequential injection of ADP (state3), oligomycin (state4o), FCCP (state 3u), rotenone/antimycin A (block all respiration). ATP production was estimated from the difference between state 3 and state 4o respiration. Spare respiratory capacity was estimated from the difference between state 3u and state 4o respiration.

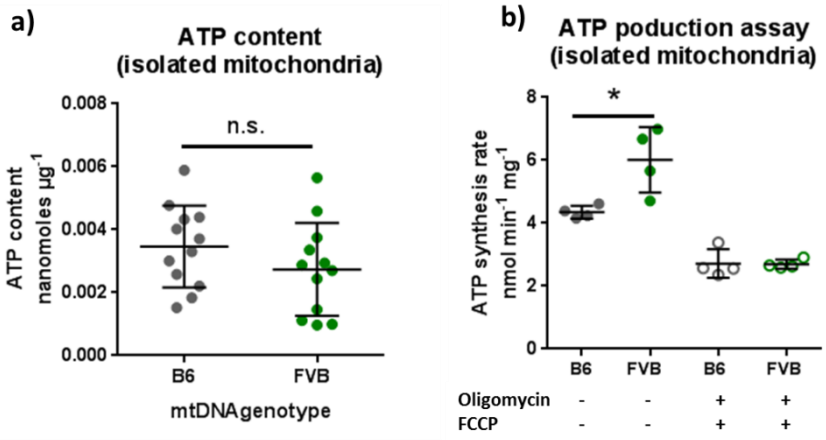

*Figure 16: ATP content and production rate in isolated mitochondria. ATP content (a) and ATP production rate (b) in isolated liver mitochondria. (b) ATP production was inhibited by addition of oligomycin (oligo) and FCCP to abolish ATP synthase activity and evaluate the specificity of the reaction. ATP was detected by chemiluminescence reactions and normalized to the sample protein amount. * p-value<0.05, Wilcoxon rank-sum test.*

The measurement of the ATP content in freshly isolated mitochondria indicates a minor decrease in the steady state energy level that was also observed in whole cells and corresponds with the decreased respiratory in the cells. Measurement of ATP production in freshly isolated mitochondria under excess of artificial substrates however highlights a significantly increased ATP production rate in the *mt-Atp8* mutant strain compared to the wild-type strain (Figure 16) and is in contrast to the observed reduced ATP/ADP ratio in cells. These findings indicate a differential regulation of mitochondrial respiration and energy production *in vivo* implying regulatory processes that restrain metabolic flux and OXPHOS activity *in vivo*.

The altered mitochondrial respiration complex activities as well as the mitochondrial oxygen consumption and increased glycolytic flux indicate a systematic effect of the mtDNA mutation on the energy equilibrium and nutrient utilization. *In vitro* measurements oxygen consumption and enzyme activity in isolated mitochondria reveal a discordant relation between the individual enzyme activities and the integrated activity of the combined respiratory chain, indicating a complex regulatory influence *in vivo* that is not reproduced under excess conditions *in vitro*.

3.4.3 **Metabolite analysis**

As the obvious alterations in the respiration and glycolytic activity already indicate a significant shift in the metabolic balance induced by the *mt-Atp8* mutation and *in vitro* measurements indicate a differential influence of metabolic flux that modulate OXPHOS activity *in vivo,* a metabolic profile in different tissues was evaluated to investigate a potential systemic influence of the *mt-Atp8* mutation on the metabolic equilibrium. Tissue samples of

liver, lymph nodes, skin, thymus, and brain as well as blood plasma were prepared for mass spectrometric analysis using the AbsoluteIDQ® p150 Kit (Biocrates Life Sciences AG, Innsbruck, Austria) and analysis platform at the Helmholtz center, Munich. Metabolite data was normalized by PQN (Figure 17) and significantly altered metabolite profiles were evaluated (Figure 18). Most significant differences between wild-type and *mt-Atp8* mutant mice were observed in liver skin, and thymus tissue, showing a certain degree of overlap in the significant metabolites (Figure 18a,b).

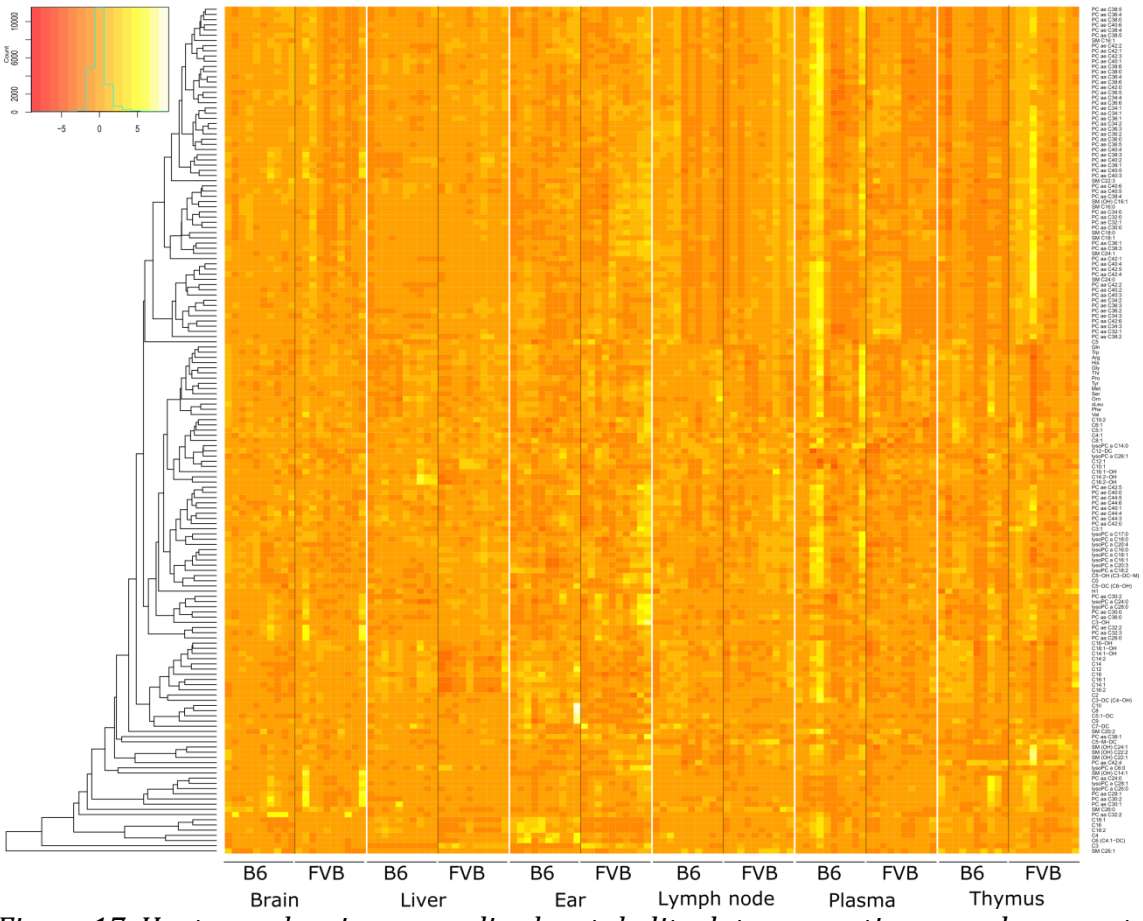

Figure 17. Heatmap showing normalized metabolite data across tissues and mouse strains. Heat map depicting metabolite data of ear tissue sample wise Data was normalized by median probabilistic quotient normalized (PQN) (Dieterle et al., 2006; Di Guida et al., 2016). *Heatmaps created with R package 'gplots'* (Warnes et al., 2016). *B6: wild-type strain; FVB: B6-mtFVB, mt-Atp8 mutant strain.*

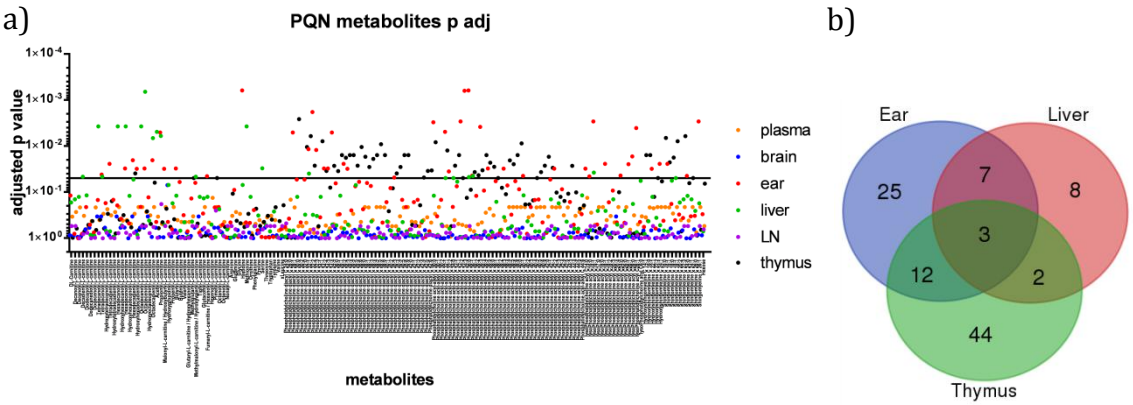

Figure 18. Metabolites showing significant differences between the mt-Atp8 genotype across multiple tissues. (a) Manhattan plot showing adjusted p-values for each normalized metabolite in individual tissue. PQN normalized data was compared between the strains for each tissue by 2-way ANOVA, p-values were adjusted for multiple testing using the Benjamini-Hochberg correction, cut-off at 0.05. (b) Venn Diagram of overlapping metabolites in the three tissues showing the significant differences dependent on the mt-Atp8 genotype.

Due to the selection of metabolite markers evaluated in the screening, the majority of significant differences were observed in phospholipids. The overlap of differentially abundant metabolites between the ear, liver, and thymus hints at a systematic change in the metabolic balance of the *mt-Atp8* mutant strain (Figure 18b). Brain, lymph node and blood plasma metabolites show only minor or no differences in the metabolite profile, indicating a tissue specific influence of the metabolic changes. In the next step the analysis was focused on subsets of metabolites and specific interactions of metabolites with cellular functions were evaluated.

3.4.4 **Short chain fatty acids**

The metabolites data set contains a variety of fatty acids. Although the majority of the analysis focuses on long chain fatty acids it also includes a variety of short-chain acyl-carnitines related to short chain fatty acids

(SCFA) (Taylor et al., 2014). Acetate, propionate, and butyrate are short chain fatty acids and are metabolites used as energy source and as potent regulators of gene expression. The metabolite dataset contains a variety of SCFA associated acyl-carnitines. The concentration of Acetyl-, propionyl-, and butyryl-carnitine were used to assess difference in the concentrations of SCFA between *mt-Atp8* mutant and wild-type tissues (Figure 19).

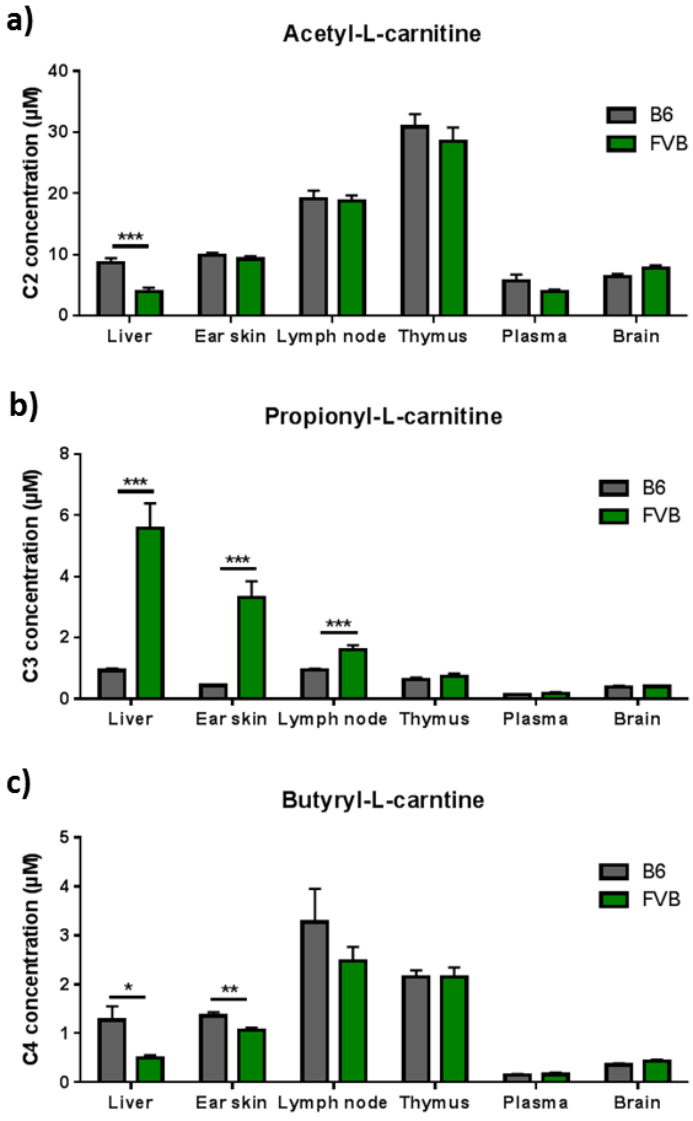

*Figure 19: Short chain fatty acids (SCFA) in tissues of healthy mice. Tissues metabolites were isolated and detected at the Helmholtz Center Munich using the Absolute kit IDQ p150 kit. SCFA concentration of acetate (C2), propionate (C3), and butyrate (C4) were correlated with the concentration of acetyl-, propionyl-, butyryl-carnitine, respectively. * p-value<0.05, ** p-value<0.01, *** p-value<0.001, t-test correct for multiple comparison (FDR).*

Similar to the observation in metabolite profile of PQN normalized data the concentration of SCFA associated metabolites shows the most prominent changes in liver tissue whereas no major changes were observed in blood plasma, brain, as well as thymus (Figure 19). The comparison of SCFA in different tissue revealed several significant changes in the *mt-Atp8* mutant strain. The concentration of acetate (C2) is reduced in liver (Figure 19a). Similarly the concentration of butyrate (C4) is significantly decreased in liver and ear skin tissue of *mt-Atp8* mutant mice (Figure 19c). On the other hand, the concentration of propionate (C3) is strongly increased in liver, skin, and lymph node tissue of the *mt-Atp8* mutant strain (Figure 19b).

3.4.5 **Fatty acid saturation**

The focus of the metabolite analysis on mostly fatty acids enables a detailed observation of the their saturation level. It has been published that the balance between polyunsaturated and saturated fatty acids influences the expression of IL-17 and plays a critical role in the polarization and pathogenicity of Th17 immune response (Wang 2015, Cell). A high ratio of PUFA to SFA indicates downregulation of IL-17 expression. Similarly the ratio of PUFA/SFA in the skin and thymus of *mt-Atp8* mutant mice was significantly increased compared to the ratio in wild-type. In lymph node, brain and plasma no significant differences were observed. In the liver a significant reduction in the ratio of PUFA/SFA was observed (Figure 20).

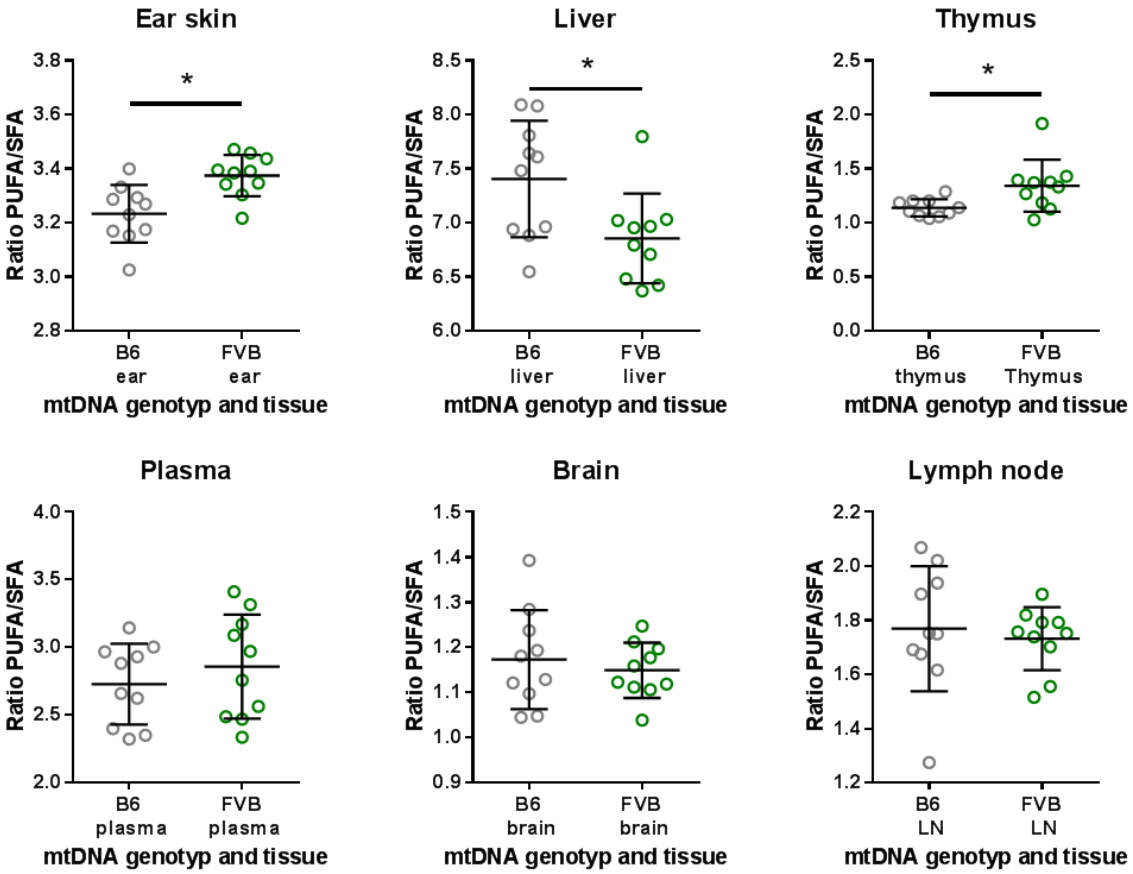

*Figure 20. Ratio of concentrations of polyunsaturated fatty acids (PUFA) to saturated fatty acids (SFA) in different tissues of wild-type and conplastic mt-Atp8 mutant mice. * p-value<0.05, student's t-test, p-value adjusted by Benjamini-Hochberg correction for multiple testing.*

These observations indicate a tissue specific modulation of the saturation grade of fatty acids and may play a role in a potential tissue specific influence on the polarization of Th17 responses. Lymph node tissues of healthy wild-type and *mt-Atp8* mutant mice do not show differences in the PUFA/SFA ratio. However, in the skin of *mt-Atp8* mutant mice a significant alteration to this immunomodulatory potential is seen which hints at a putative dysregulation in the skin. This in turn may shape the organ-specific immune response that will be translated to the lymph nodes upon inflammation.

3.4.6 **Acyl-carnitine ratio and fatty acid oxidation**

An increased ratio of $[C_0]/[C_{16\text{-}18}]$ acyl-carnitines is associated with CPT-I deficiency and decreased fatty acid oxidation (Fingerhut et al., 2001). In metabolite data the ratio of free carnitine (C_0) to the sum of all palmitoyl- and stearoylcarnitines (C_{16}-C_{18}) acyl-carnitines is significantly increased in ear, liver, and lymph node tissue (Figure 21). While ear and lymph node tissues only show a moderate increase in the ratio, there is a dramatic increase in the liver tissue. These observations may indicate a reduced β oxidation activity in the *mt-Atp8* mutant strain which is further supported by the metabolically related decrease in OXPHOS activity.

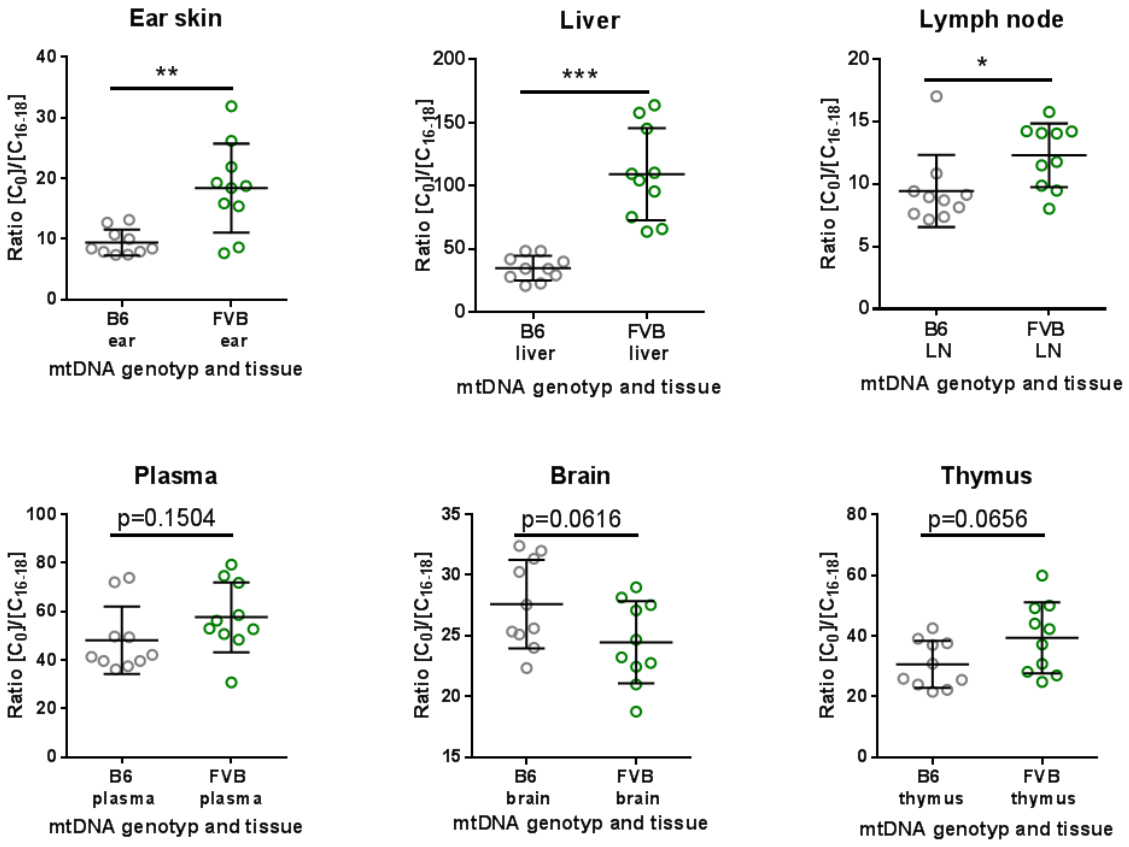

*Figure 21. Ratio of free carnitine to palmitoyl- and stearoylcarnitines as an indicator of CPT-I and β oxidation activity. The ratio was determined by dividing the concentration of free carnitine (C_0) with the sum of the concentration of palmitoyl- and stearoylcarnitines C_{16} to C_{18} ($[C_0]/[C_{16\text{-}18}]$). B6: wild-type strain; FVB: B6-mtFVB strain. * p<0.05, ** p<0.01, *** p<0.001, student's t-test, p-value adjusted by Benjamini-Hochberg correction for multiple testing.*

3.4.7 **Indirect calorimetry**

The skewed energy metabolism and the balance of metabolites in the *mt-Atp8* mutant mice indicate a systemic alteration of metabolic activity in the mice. To investigate the systemic metabolic activity of these mice indirect calorimetric measurements were performed. Mice that have been acclimatized to the calorimetric box were monitored for oxygen consumption, carbon dioxide production, food and water intake, as well as locomotor activity to assess metabolic activity of the mice. The *mt-Atp8* mutant strain shows a significant increase in the RER compared to the wild-type strain (Figure 22a,c) indicating a shift in the composition of oxidation substrates with less use of lipid oxidation and/or an increased glycolysis activity in the *mt-Atp8* mutant mice. However, no significance was detected when comparing the energy expenditure (EEx) or water intake between the wild-type and *mt-Atp8* mutant strain (Figure 22c,d,i,j) and only a minor increase in the food intake was observed in the mutant mice (Figure 22g,h). However, locomotor activity, monitored by infrared sensors, was significantly decreased in the mutant mice (Figure 22e,f).

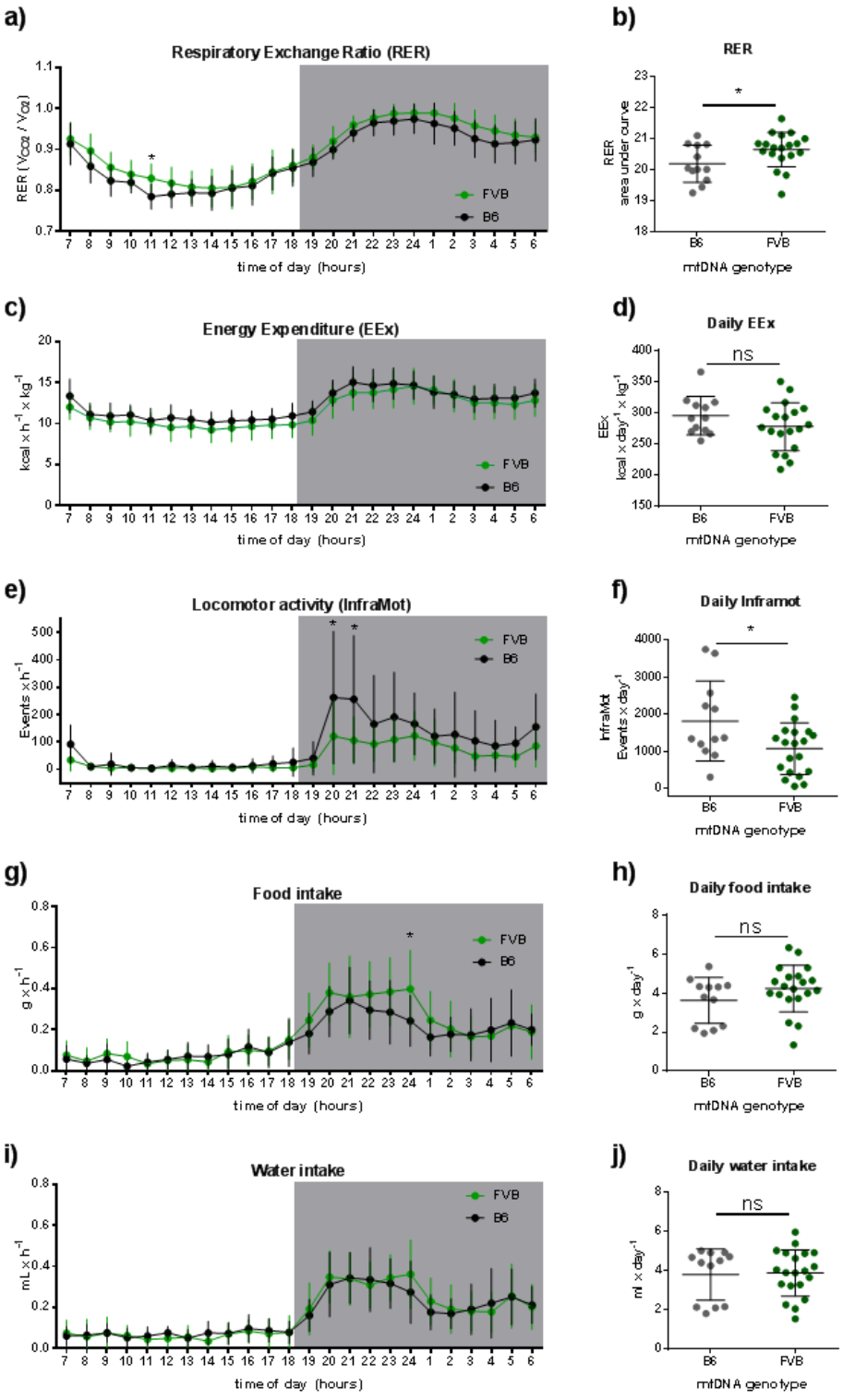

*Figure 22. Indirect calorimetric measurements of mt-Atp8 mutant and wild-type mice. Mice were assessed in open-circuit indirect calorimetry systems for metabolic activity: respiratory exchange rate (RER) (a,b), energy expenditure (EEx) (c,d), spontaneous locomotor activity (InfraMot) (e,f), food intake (g,h) and water intake (i,j). Summarized data by hourly average values (a,c,e,g,i) and daily average values (b,d,f,h,j). * p-value<0.05; 2-way ANOVA for (a,c,e,g,i) or student's t-test for (b,d,f,h,j).*

Previous work has shown behavioral differences and increased anxiety in *mt-Atp8* mutant mice (Gimsa et al., 2009). The reduced locomotor activity in the confined space of the calorimetric cage might reflect the previously described observation. Although no significant correlation was found between locomotor activity and RER in both strains, locomotor activity shows significant correlation with EEx in the *mt-Atp8* mutant mice but not in the wild-type strain (Figure 23; B6-mtFVB: EEx vs. InfraMot Pearson r=0,6687, p=0.0017). This observation might indicate that the mutant mice retain a certain degree of metabolic balance but have a limited capacity to adapt to increasing stress by e.g. exercise. The *mt-Atp8* mutant strain shows similar levels of energy expenditure while exhibiting significantly less locomotor activity, indicating that the mutant mice consume more nutrients to maintain their energetic balance. Additionally, the higher RER indicates a shift in the composition of nutrients that are metabolized to sustain energy demand in the *mt-Atp8* mutant mice. However, the effects of anxiety induced behavioral changes and the limits in the exercise capacity of the *mt-Atp8* mutant mice have to be further evaluated to enable conclusive interpretation of the observation in this indirect calorimetric evaluation.

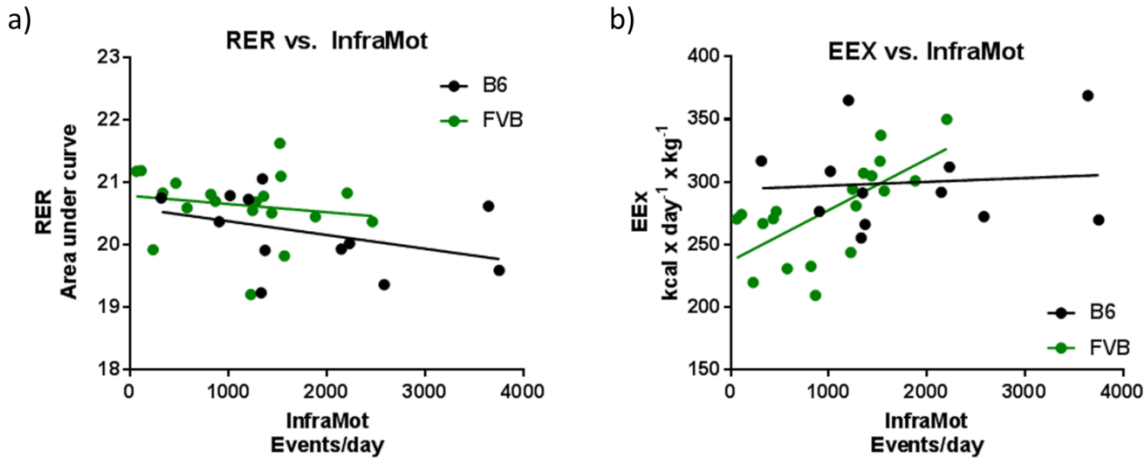

Figure 23. Correlation between (a) RER and InfraMot or (b) EEx and InfraMot. No correlation in B6. For the mt-Atp8 mutant strain, no correlation between RER and InfraMot, significant correlation between EEx and InfraMot (Pearson r=0,6687; p=0.0017)

3.5 **Microbial community structure at the skin barrier**

As described above, the *mt-Atp8* mutation in the B6-mtFVB strain affects a variety of immune cell phenotypes and additionally changes the immune milieu at the skin barrier. As it is already well known that commensal bacteria interact with the immune system and can alter the immune milieu of their host (Belkaid and Naik, 2013; Naik et al., 2015) it was considered a strong possibility that the structure of the skin microbiome community was altered in the *mt-Atp8* mutant strain. General distribution of the various identified bacterial phyla and families did not show obvious deviations between the wild-type and the *mt-Atp8* mutant strain (Figure 24). However, analysis of the diversity between the skin microbial communities of the wild-type and *mt-Atp8* mutant mice revealed significant differences in alpha diversity, assessed by Chao1 and Shannon diversity indices (Figure 25a,b), and beta diversity (Figure 25c-h, Table 10). Performing an indicator species analysis revealed the presence of multiple OTUs in the skin microbiota that segregate dependent on the *mt-Atp8* genotypes (Figure 26). Previous, unpublished analyses comparing the skin microbiota between *mt-Atp8* wild-type and mutant mice have revealed similar patterns in the differences between the strains. Comparison of these independent replications revealed recurrent associations of OTUs from specific bacterial families with the *mt-Atp8* wild-type or mutant strain, respectively (Figure 27). The overlap in the comparison provides stronger confidence in the reliability of the skin microbiota associated with the *mt-Atp8* genotypes. Although there is considerable overlap at the level of bacterial families that are associated with wild-type and *mt-Atp8* mutant mice across the three replicated microbiota analyses (Table 12) the repeated association of particular OTUs with the wild-type or mutant strain provides initial indications for stable skin microbiota environments in both strains. Through the indicator

species analysis preliminary predictions can be further formulated concerning the importance of identified OTUs resolved to the bacterial genus level and allow the postulation of the functional relevance of bacterial species. This allows better predictions of the potential function of indicator species in the skin environment of the wild-type and mutant mice. Bacteria belonging to the genus *Staphylococcus* have been consistently associated with the wild-type strain in all three microbiota analyses. In previous analyses these OTUs associated with the wild-type strain were classified as the bacterium *Staphylococcus epidermidis* (Figure 28*a*). The analysis of the skin microbiota in this work identified an OTU associated with the wild-type strain that was classified as *Staphylococcus xylosus*. Although, these two species of the *Staphylococcus* genus show marked differences in their genetic repertoire and possibly diverge in their pathogenic potential (Tan et al., 2014) the true identity of these OTUs associated with the wild-type strain have not been validated (i.e. by sequencing the whole length 16S rRNA gene of bacterial isolates). Similarly, OTUs associated with the *mt-Atp8* conplastic strain have been classified as bacteria belonging to the genera *Gordonia* and *Dietzia* in earlier skin microbiota analyses (Figure 28b). The *mt-Atp8* genotype-associated correlations with potential immune modulatory bacteria further strengthens the postulated hypothesis that the *mt-Atp8* mutation alters the homeostasis at the skin barrier and affects the disease phenotype through multiple pathways and functional modalities.

The classification of OTUs is dependent on the information provided in reference databases and thus complete annotation of the OTUs in the microbiota dataset at the resolution of the bacterial species level is unlikely. Replication of the microbiota analysis can provide additional confidence in the results and reduce the number of false positive associations.

Additionally, indicator species analysis provides further insight in possible connection between the *mt-Atp8* genotype and the potential function of bacterial associations. These theoretical predictions are limited by the confidence in the association and the inaccuracy of the OTU classifications. Still, the identity of OTUs, associated with the *mt-Atp8* genotypes has to be confirmed by further efforts in sequencing additional regions of the 16S rRNA gene or by isolating and culturing the respective bacterial species. Nonetheless, the analysis provides novel insight into potential pathways that affect the immune milieu at the skin barrier.

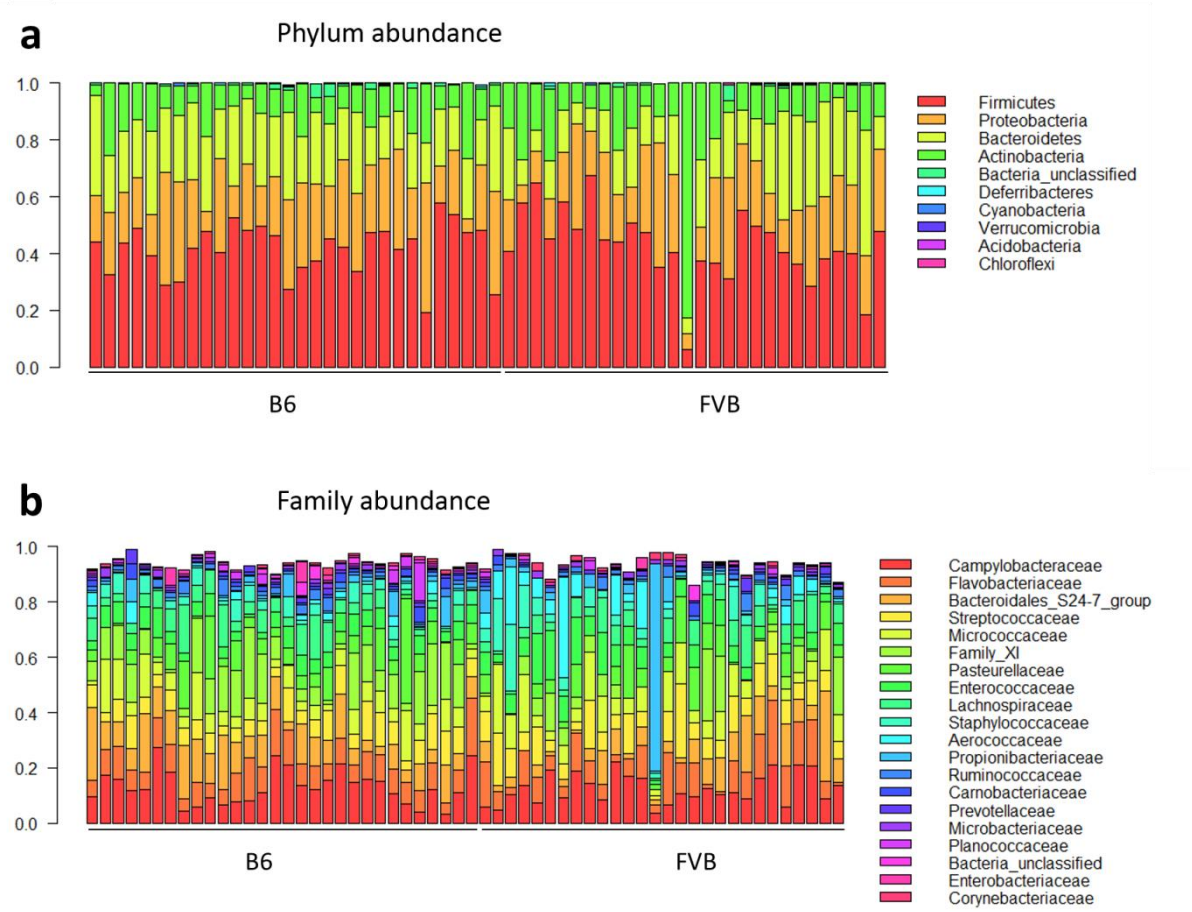

Figure 24. Composition of microbial communities at the skin barrier. Relative abundance of dominant bacterial phyla (a) and bacterial families (b). B6: wild-type strain; FVB: conplastic B6-mtFVB strain.

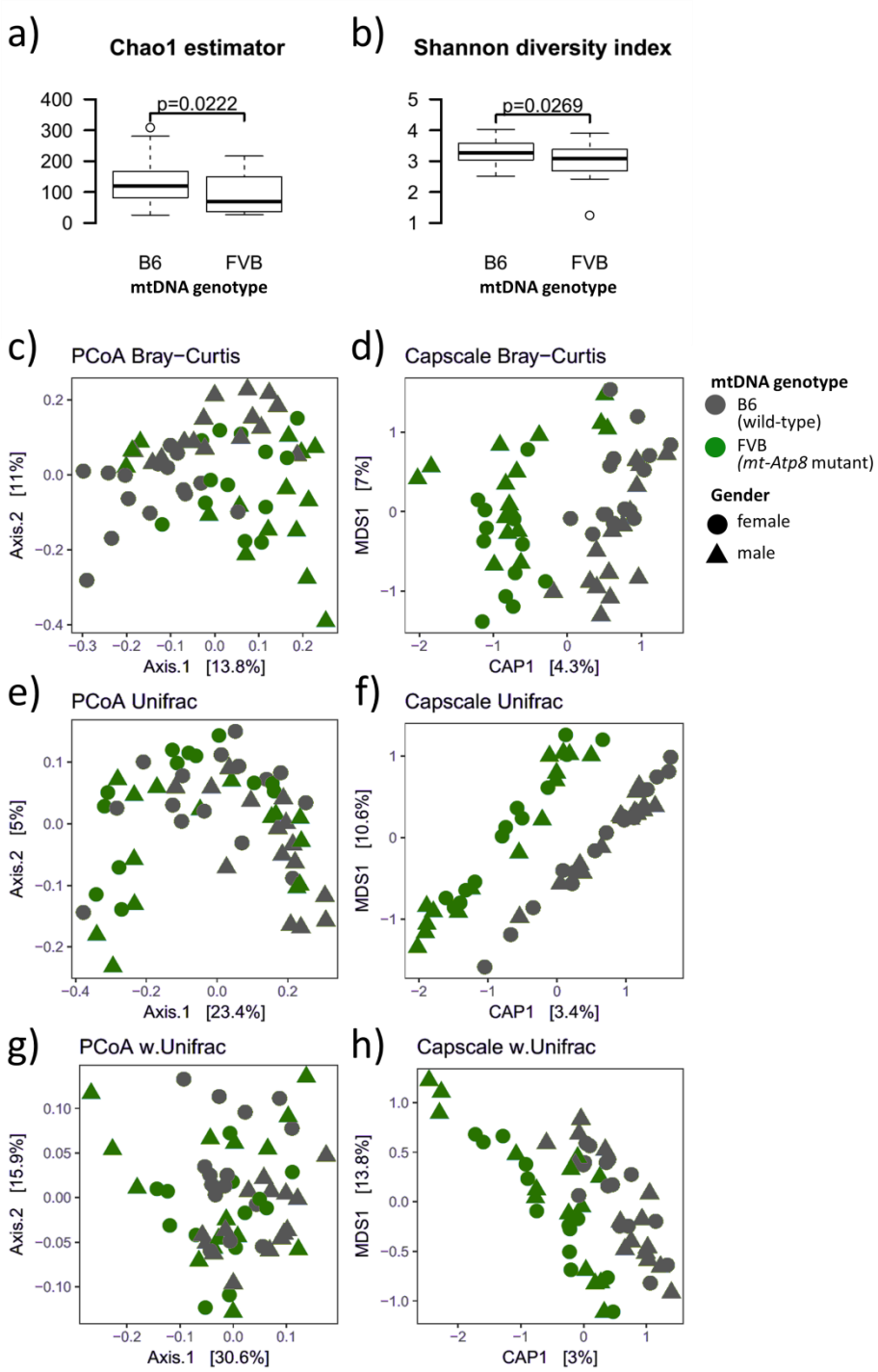

Figure 25. Alpha- and beta-diversity of skin microbiota in conplastic mice. Skin microbiota of conplastic mt-Atp8 mutant mice (FVB) and wild-type mice (B6) was evaluated by next generation sequencing of the V1-V2 region of the bacterial 16S rRNA gene. Alpha-diversity was assessed by calculating chao1 Index (B6 vs. FVB: Wilcoxon rank sum test p =0.02216) (a) and Shannon diversity index (B6 vs. FVB: Wilcoxon rank sum test p =0.0269) (b). Beta-diversity was evaluated by calculating Bray-Curtis dissimilarities (c,d), weighted (e,f) and unweighted UniFrac (g,h) matrices and analyzing statistical differences between the mouse strains by perMANOVA (c,e,g) or Constrained Analysis of Principal Coordinates (d,f,h) (see section 2.22.4). Data was visualized by ordination methods PCoA (c,e,g) or capscale (d,f,h) using the software R. B6: wild-type strain; FVB: mt-Atp8 mutant strain, (B6-mtFVB); circles: female; triangles: male. Summary of the statistical significance is shown in (Table 10)

Table 10. Statistical analysis of beta diversity based on multiple distance metrics and comparison methods. Ordinated metrics visualized in Figure 25.

Statistical test	Distance matrix	Comparison factor	p-values
perMANOVA (adonis)	Bray-Curtis	Strain	0.001
		Strain and gender	0.001
	unweighted UniFrac	Strain	0.002
		Strain and gender	0.006
	weighted UniFrac	Strain	0.014
		Strain and gender	0.003
ANOVA on constrained analysis of principal coordinates (capscale)	Bray-Curtis	Model	0.001
		Strain	0.001
		Strain and gender	0.001
	unweighted UniFrac	Model	0.003
		Strain	0.004
		Strain and gender	0.002
	weighted UniFrac	Model	0.011
		Strain	0.025
		Strain and gender	0.018
Goodness of fit (PCoA)	Bray-Curtis	Strain	0.001
		Strain and gender	0.001
	unweighted UniFrac	Strain	0.015
		Strain and gender	0.001
	weighted UniFrac	Strain	0.048
		Strain and gender	0.021

OTU	resolved to	OTU classifcation	corrected p value	Indicator for
Otu20	Family	Bacteroidales_S24-7_group	0,001999	B6
Otu241	Family	Clostridia_unclassified	0,001999	B6
Otu297	Family	Lachnospiraceae	0,001999	B6
Otu48	Genus	Prevotellaceae_UCG-001 sp.	0,001999	B6
Otu88	Genus	Alloprevotella sp.	0,001999	B6
Otu103	Species	Sporosarcina soli	0,003996	B6
Otu16	Species	Staphylococcus xylosus	0,003996	B6
Otu234	Genus	Incertae_Sedis sp.	0,003996	B6
Otu71	Species	Atopostipes suicloacalis	0,003996	B6
Otu216	Genus	Lachnospiraceae_UCG-001 sp.	0,005991	B6
Otu32	Genus	Lachnospiraceae_NK4A136_group sp.	0,005991	B6
Otu51	Family	Bacteria_unclassified	0,007984	B6
Otu608	Species	Sporosarcina soli	0,007984	B6
Otu7	Species	Gemella palaticanis	0,007984	B6
Otu66	Species	Roseburia inulinivorans	0,009975	B6
Otu182	Family	Lachnospiraceae	0,011964	B6
Otu189	Species	Sporosarcina soli	0,013951	B6
Otu248	Family	Bacteria_unclassified	0,013951	B6
Otu960	Family	Bacteroidales_S24-7_group	0,015936	B6
Otu245	Family	Bacteroidales_S24-7_group	0,017919	B6
Otu40	Species	Atopostipes suicloacalis	0,0199	B6
Otu422	Species	Blautia producta strain	0,0199	B6
Otu1203	Family	Ruminococcaceae	0,021879	B6
Otu22	Species	Streptococcus acidominimus	0,021879	B6
Otu328	Genus	Lachnospiraceae_NK4A136_group sp.	0,025831	B6
Otu1332	Species	[Clostridium] aminophilum	0,027804	B6
Otu36	Genus	Allobaculum sp.	0,031744	B6
Otu92	Family	Bacteroidales_S24-7_group	0,031744	B6
Otu411	Family	Lachnospiraceae	0,033711	B6
Otu717	Species	Atopostipes suicloacalis	0,035676	B6
Otu10	Family	Bacteroidales_S24-7_group	0,037639	B6
Otu112	Species	Butyricicoccus pullicaecorum	0,037639	B6
Otu748	Species	[Clostridium] clostridioforme	0,037639	B6
Otu113	Species	Marinilactibacillus piezotolerans	0,0396	B6
Otu154	Genus	Lachnospiraceae_NK4A136_group sp.	0,045471	B6
Otu519	Species	Intestinimonas butyriciproducens	0,047424	B6
Otu13	Species	Aerococcus viridans	0,001999	FVB
Otu98	Genus	Alloprevotella sp.	0,001999	FVB
Otu15	Species	Staphylococcus arlettae	0,003996	FVB
Otu86	Species	Bacteroides sartorii; Bacteroides chinchillae	0,009975	FVB
Otu83	Family	Bacteroidales_S24-7_group	0,011964	FVB
Otu137	Genus	Prevotellaceae_UCG-001 sp.	0,013951	FVB
Otu37	Family	Lachnospiraceae	0,015936	FVB
Otu18	Species	Streptococcus henryi	0,017919	FVB
Otu348	Family	Firmicutes_unclassified	0,0199	FVB
Otu41	Genus	Prevotellaceae_NK3B31_group sp.	0,021879	FVB
Otu406	Family	Bacteroidales_S24-7_group	0,023856	FVB
Otu1431	Family	Bacteroidales_unclassified	0,027804	FVB
Otu64	Family	Bacteroidales_S24-7_group	0,031744	FVB
Otu76	Genus	Roseburia sp.	0,033711	FVB
Otu11	Species	Enterococcus gallinarum	0,045471	FVB

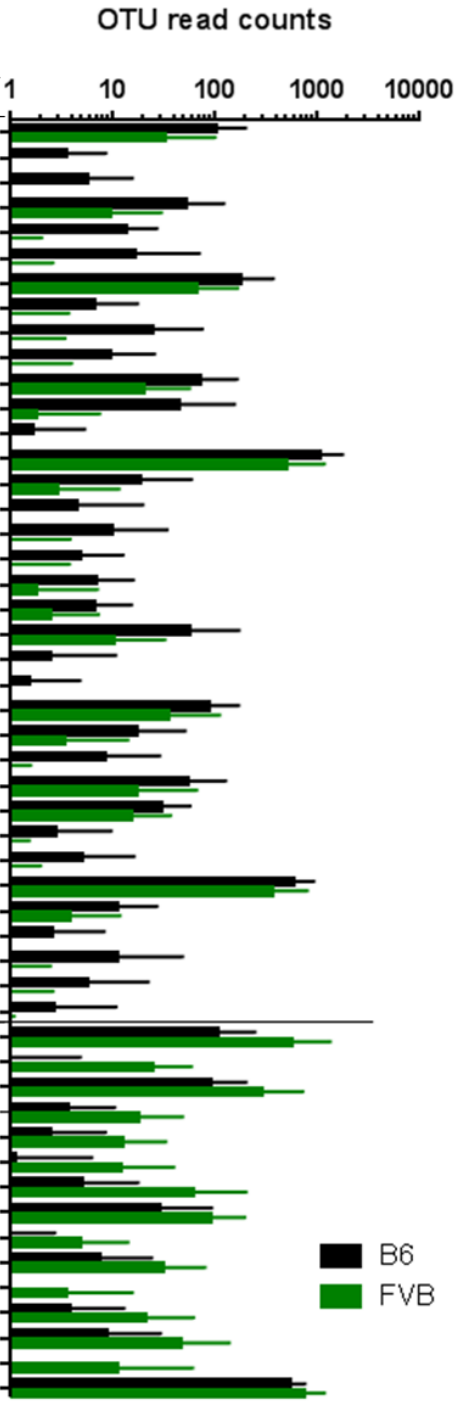

Figure 26. Microbial indicator species analysis. Significant OTUs distinguishing between wild-type and mtAtp8 mutant mice. Arbitrary OTU number and the corresponding OTU classification, corrected p-value, and the associated mtDNA genotype. Plotted are the average Read counts and standard deviation of each significant OTU.

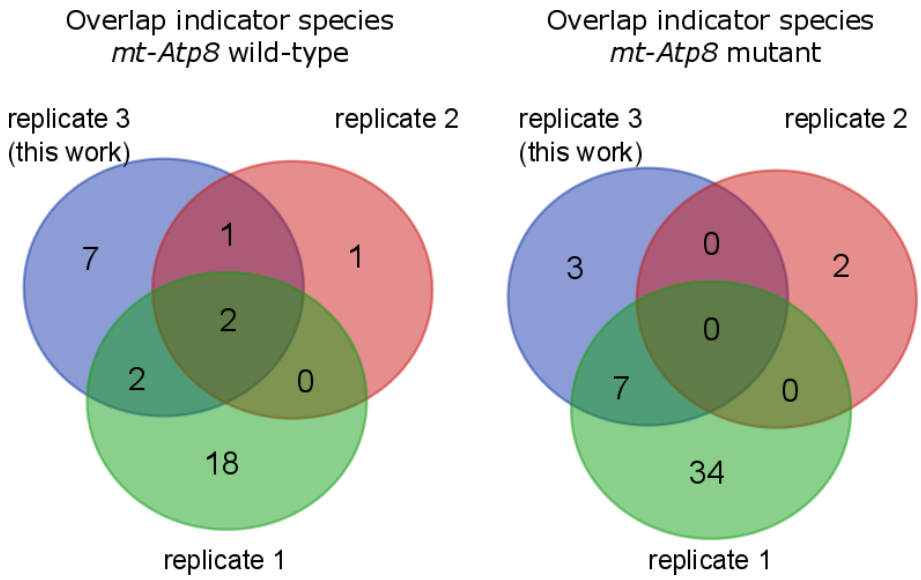

Figure 27. Overlap of indicator species associated with the mt-Atp8 wild-type and mutant. Recurrent families identified in indicator species analysis in three independent replications of skin microbiota analyses comparing mt-Atp8 wild-type and mt-Atp8 mutant mice. Bacterial families listed in Table 12 (see section 6.1)

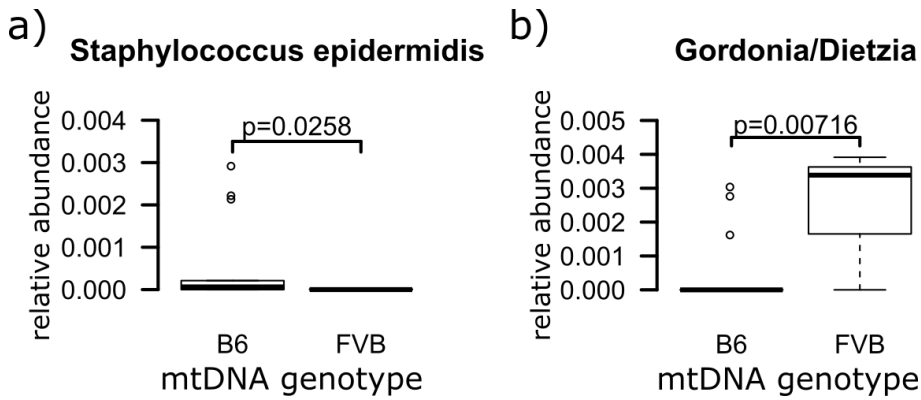

Figure 28. Analysis of previous dataset of skin microbiota in mt-Atp8 wild-type and mutant mice. Indicator species associated with the wild-type (Staphylococcus epidermidis) (a) or mt-Atp8 mutant (Gordonia/Dietzia) (b) genotypes. Analysis performed on previous skin microbiota datasets by Julia Bischof (unpublished data). Significance tested by Wilcoxon rank sum test.

4 DISCUSSION

4.1 Mutation in the *mt-Atp8* gene ameliorates experimental EBA and suppresses immune cell function

As previously reported, the mitochondrial function in B6-mtFVB mice is altered due to a single nucleotide polymorphism in the *mt-Atp8* gene at position mt7778G/T leading to an amino acid exchange from aspartate to tyrosine. Multiple publications have demonstrated that this mtDNA mutation influences the severity of multiple mouse models while healthy untreated mice are not impaired by the mutation (Eipel et al., 2011; Scheffler et al., 2012; Weiss et al., 2012b; Yu et al., 2009a, 2009b). The observed effects of the mutation in the mt-Atp8 gene are apparent in a variety of nuclear genome environments demonstrating that the non-synonymous mutation in the mtDNA has a dominant effect on mitochondrial function independent of the nuclear genome environment. Similarly in a human association study it was shown that particular mitochondrial haplotypes in the *MT-ATP8* gene are associated with bullous pemphigoid or are associated with the control groups. These results highlight that mutations in the mtDNA and the *MT-ATP8* gene in this particular case can be associated with a protective phenotype (Hirose et al., 2015). As demonstrated in this work, a mutation in the mouse *mt-Atp8* gene in the conplastic mouse strain B6-mtFVB results in a reduced disease score in antibody-transfer induced EBA (Figure 7) when compared to the genetic control strain. Injections of a low dose (2x3mg) of total rabbit anti-mouse type VII collagen IgG is considerably lower than in other published protocols for this disease model (Sitaru and Zillikens, 2005) and induces a milder phenotype. Under these conditions modulatory influences like the

mtDNA mutation in the *mt-Atp8* gene in the B6-mtFVB strain are likely to become more apparent and a significant decrease in EBA disease severity has been observed. Similarly the *mt-Atp8* mutation is protective in another antibody-transfer induced inflammation model (antibody-induced arthritis, unpublished data). The unaltered functional phenotypes of neutrophil granulocytes in the *mt-Atp8* mutant strain indicate that the phenotype observed in the experimental EBA model (Figure 7) is not mediated by altered neutrophil function and therefore the ameliorated disease phenotypes in the *mt-Atp8* mutant strain are likely mediated through other functional consequences of the mutation.

Published work shows that the downregulation and deficiency of T cells and their specific subpopulations reduces the disease severity in the antibody-transfer induced EBA mouse model (Bieber et al., 2016).

Mitochondrial functions also play a critical role in T cell activation as well as in T cell metabolism (Buck et al., 2016; Kamiński et al., 2013; Sena et al., 2013b; van der Windt et al., 2012). The *mt-Atp8* mutation in the B6-mtFVB mice affects the metabolism of T cells as seen by the decreased oxygen consumption and increased glycolysis with an overall decrease in the energy balance seen by the decrease of the ATP/ADP ratio (Figure 14). Additionally naïve T cells of the *mt-Atp8* mutant strain produce a higher amount of ROS. These functional changes in the mitochondria affect T cell activation and stimulation as seen by a decreased proliferation, and a reduced fraction of IL-17 producing T cells in the *mt-Atp8* mutant (Figure 8). IL-17 is a critical factor in pemphigoid diseases (Arakawa et al., 2011; Fischer-Stabauer et al., 2012; Zebrowska et al., 2013) and has been implicated in the pathogenesis of EBA model (unpublished data, personal communication by Prof. Ralf Ludwig, LIED, University of Lübeck). The

decreased IL-17^{+} T cell population supports the observed decrease in the EBA phenotype in the B6-mtFVB mice.

Additionally, resident T cell populations in the skin are potential factors for the immunomodulation at the skin barrier in the EBA model. The skin forms a critical barrier to protect the body from unwanted exposure to exogenous hazards and infectious agents. To efficiently fulfill this role the skin barrier is comprised of a diverse set of immune cells that help in recognition of pathogens, first line defense and recruitment and regulation of immune cells and inflammatory mediators.

Among those cells are skin resident dendritic epidermal T cells (DETC) a population of γδT cells that are generated in the fetal thymus and colonize the epidermal skin layer as well as dermal γδT cells which in general have restricted TCR usage and are involved in immunosurveillance and wound repair (Girardi, 2006; Heath and Carbone, 2013; Ribot et al., 2009; Sharp et al., 2005; Sumaria et al., 2011). The observed, reduced numbers of γδT cells in the *mt-Atp8* mutant strain (Figure 9) likely result in reduction of chemokine production and thereby limit the amount of immune cell infiltration and inflammation.

γδT cells produce IL-17 upon skin injury and although this process can facilitate wound healing (MacLeod et al., 2013), IL-17 has been implicated to be important in pemphigoid diseases and skin inflammation models like the antibody-transfer induced EBA model (Arakawa et al., 2011; Fischer-Stabauer et al., 2012; Zebrowska et al., 2013). DETCs play a critical role in skin inflammation as a source of IL-17 and deficiency of these cells can ameliorate inflammation (Nielsen et al., 2014).

4.2 **Bioenergetic flux and shift of equilibria in *mt-Atp8* mutant mice**

Regulation of mitochondrial ROS (mtROS) is critical for activation and survival of T cells (Chen et al., 2016). The altered regulation and production of mtROS in the *mt-Atp8* mutant mice is a potential influential factor in the homeostasis of immune cell regulation. *In vitro* and *in vivo* measurements of the OXPHOS system show a certain degree of disparity (higher enzyme activity in isolated mitochondria [Figure 12], yet lower cellular respiration [Figure 14a]) indicating a potential metabolic control on the flux of the respiratory chain *in vivo* that is unhinged under *in vitro* conditions of artificial substrates at excess concentrations (Curi et al., 2016). The increased mitochondrial OXPHOS activity *in vitro* was measured under excess substrate conditions and does not reflect that substrate regulation *in vivo*. The increased OXPHOS activity might indicate an adaptation in the conplastic *mt-Atp8* mutant mice to compensate for the induced metabolic dysregulation. The structural organization of the ATP synthase is crucial for mitochondrial structure and organization and consequently for the metabolic activity. It was shown that the complete lack of both mtDNA encoded ATP synthase subunits a and A6L (the genes *mt-Atp6* and *mt-Atp8*, respectively) still allows the full assembly of the monomeric enzyme complex. However, oligomer formation is impaired when the subunit A6L is missing, implying the requirement of the *mt-Atp8* encoded subunit A6L for oligomerization of the ATP synthase into supracomplexes (Wittig et al., 2010). The organization of ATP synthase enzyme complexes into multimers or supracomplexes affects flux and facilitates “substrate channeling” in the respiratory chain (Bornhövd et al., 2006). It was shown that the complete lack of expression of mtDNA encoded ATP synthase subunits mt-Atp6/8 in a human cybrid cell line reduces oxidative phosphorylation and diminishes

expression and function of complex II, III, and IV. Nuclear expression of the *MT-ATP8* encoded protein A6L through an exogenous vector was able to reconstitute the structural assembly and function of the OXPHOS complexes and restore normal respiratory function (Boominathan et al., 2016). Inability to form oligomeric ATP synthase supracomplexes is associated with decreased membrane potential, increase in membrane fluidity, and destabilization of other membrane complexes (i.e. OXPHOS complexes) (Bornhövd et al., 2006). This is in line with the observations in the *mt-Atp8* mutant strain showing a decrease in the mitochondrial membrane potential (Figure 8c), a shift from hexameric to monomeric ATP synthase complexes (Figure 13), and lower flux of substrates through the entire respiratory chain reducing the oxygen consumption in the cells of the *mt-Atp8* mutant mice (Figure 14).

Potential reorganization of ATP synthase complexes into dimers and oligomers affects mitochondrial organization, substrate channeling, the redox balance, and alters substrate flux. Shifting the metabolic balance cascades through multiple regulatory cycles of metabolic flux which influence and control respiration and mitochondrial ATP synthesis (Brown, 1992). Oxidative phosphorylation becomes less efficient and the energy balance decreases which presumably leads to metabolic adaptations that in turn potentially affect steady state gene expression and signaling homeostasis in immune cells and inflammation related pathways that in conjunction with altered mitochondrial function lead to altered immune cell phenotypes.

4.3 **Systemic metabolic adaptation**

Mice carrying the *mt-Atp8* mutant show a shift in the metabolic homeostasis that can be observed on a systemic level as seen by the increase of the RER in the mutant strain which is indicative of a shift in the composition of oxidation substrates towards carbohydrates (Arch et al., 2006; Simonson and DeFronzo, 1990). This is supported by measurements of glycolytic activity in lymphocytes which is increased in B6-mtFVB mice (Figure 8) while overall ATP/ADP ratio remains at a lower level compared to wild-type mice (Figure 14) and is consistent with similar findings in liver tissue under homeostatic conditions. The metabolic adaptation in the *mt-Atp8* mutant strain results in a shifted stress response and was shown to be protective in a murine model of acute endotoxemic liver failure (Eipel et al., 2011). Furthermore, it was shown that intracellular infections with *Chlamydia* bacteria favor a cellular environment that relies on glycolysis and consequently, fibroblasts of *mt-Atp8* mutant mice provided beneficial conditions for proliferation of the intracellular pathogen compared to fibroblasts of the wild-type strain (Käding, 2015). As pointed out by Gimsa et al., the *mt-Atp8* mutant mice suffer from elevated anxiety (Gimsa et al., 2009) which supports the observed significantly reduced locomotor activity seen in the mutant mice (Figure 22). Reduced motility of the mice should be concomitant with a decrease in energy demand as well as energy expenditure, however the *mt-Atp8* mutant mice do not show significant alterations to energy expenditure compared to wild-type mice which supports the notion that reduced OXPHOS efficiency due to the *mt-Atp8* mutation results in less efficient energy generation and higher rates of substrate oxidation in the *mt-Atp8* mutant strain.

4.4 **Adaptations of metabolite balance induced by *mtAtp8* mutation**

The concentrations of SCFA is highly skewed in the *mt-Atp8* mutant mice and the alterations in propionyl-carnitine and butyryl-carnitine indicate changes in the pool of free propionate and butyrate which are known to influence AMPK signaling, cholesterol metabolism, glucose, and fatty acid metabolism, as well as HDAC activity and regulation of gene expression (den Besten et al., 2013a, 2013b; Kim et al., 2016). Since SCFA can be produced by the mammalian metabolism as well as the gut microbiome the individual contribution of host and microbiome has not been addressed in the *mt-Atp8* mutant strain so far. Nonetheless, the alterations in SCFA concentrations, seen in the *mt-Atp8* mutant mice, point towards a regulatory mechanism influencing metabolic flux. Analysis of gene expression data comparing liver tissue of *mt-Atp8* mutant and wild-type mice reveals mostly changes in metabolic pathways like fatty acid oxidation, phospholipid and cholesterol metabolism, underlining the regulatory influences in the *mt-Atp8* mutant strain (Schröder et al., 2016 and unpublished data). Supporting the idea of an altered fatty acid metabolism is the observation of an increased ratio of free carnitine (C_0) to long chain acyl-carnitines ($C_{16\text{-}18}$), indicating a reduced oxidation of fatty acids (β-oxidation) due to a reduced activity of CPT-I (Fingerhut et al., 2001). This in turn diminishes the pool of available reducing equivalents for respiration and further supports the shift from mitochondrial respiration towards glycolysis. Thereby, leading to an increase in the RER and resulting in less efficient substrate oxidation and energy generation.

The balance of saturated and (poly-)unsaturated fatty acids influences the Th17 cells pathogenicity and IL-17 gene expression (Wang et al., 2015).

The observed tissue specific changes in the lipid composition (e.g. the PUFA/SFA ratio in skin, Figure 20) hint at organ specific alterations in the lipid homeostasis in the *mt-Atp8* mutant strain which additionally affects the immune cell homeostasis by potentially repressing fatty acid sensitive signaling pathways like the IL-17 gene expression (Wang et al., 2015). Metabolically induced changes in the skin immune homeostasis, potentially shape the signaling processes to polarize the inflammatory response in lymphoid organs upon induction of organ specific inflammation, i.e. antibody-transfer induced EBA.

Similarly, other dysregulations in the lipid metabolism and composition are implicated to correlate with innate immune cells functions. It was shown that the composition of lipids is regulated, interconnected and can be expressed as co-regulated networks in which opposing functions of individual lipids are integrated to patterns that correlate with innate immune cell functions. Co-regulated networks of sphingolipids have been applied to predict influences on TLR signaling and cytokine release (Köberlin et al., 2015).

4.5 **Effect of *mtAtp8* mutation on immunometabolism**

Inflammatory processes elevate the energy demand of cells and often influence distinct metabolic pathways to sustain signaling function and energy demand. Efficient function of highly active immune cells relies heavily on the interplay of metabolism and inflammation signaling processes. The observed reduction in mitochondrial respiration and the insufficient compensation by increased glycolysis and indirect evidence for increased beta oxidation in the *mt-Atp8* mutant mice hint at an imbalance in

metabolic activity on a systemic level that critically influences the capacity of immunological responses. Although glycolysis is an important factor in T cell stimulation (Kamiński et al., 2012; MacIver et al., 2008), the critical factor for sustained immunological function of immune cells and T cells is a sufficient metabolic supply (Yin et al., 2015). Given that the energy balance in the *mt-Atp8* mutant strain is decreased, immunological functions are likely to be restricted.

Mitochondrial-derived ATP is important for T cell activation (Ledderose et al., 2014). This finding correlates with the observed reduction in the availability of ATP in the mutant strain (Figure 14d), and a correlation with reduction of cell activation and proliferation in the *mt-Atp8* mutant strain (Figure 8a). Similarly, glucose metabolism is critical in regulation of lymphocyte survival and function (Frauwirth and Thompson, 2004; MacIver et al., 2008) and pharmacological modulation of T cell metabolism can improve clinical presentation of autoimmune disease (Yin et al., 2015). The critical point in these observations is the sustained availability of energy equivalents derived from upregulated, cell type specific, metabolic pathways. Metabolic dysregulation, induced by the mutation of mtDNA, may alter cellular capacity to adapt to induced signaling triggers and impair immune cell polarization by undersupplying metabolic demands. Metabolism is a critical part of many inflammatory processes as well as immune system related disease phenotypes. Mice suffering from immunization induced EBA show a distinct metabolite pattern which implicates the importance of energy metabolism and mitochondria related metabolites (Schönig et al., 2013).

Chronic metabolic modulation influences histone-methylation and affects gene regulation and T cell function (Oaks and Perl, 2014). Similarly, the systemic alterations in metabolism as well as changes in energy and ROS

balance observed in the *mt-Atp8* mutant mice regulate immune cell (i.e. T cell) function and potentially lead to changes in the epigenetic regulation. This may further restrict the flexibility of immune cells to respond during inflammatory signaling processes.

The data presented in this study support previously published, works highlighting the metabolic sensitivity of T cells and critical alteration in T cell function and survival. Similarly, the homeostatic survival of resident T cells in the skin compartment is likely to be impaired resulting in a decreased steady state density of T cells at the skin barrier. These findings are in line with published data stating that γδT cells are sensitive to hyperglycemia and cell density in skin decreases in obesity indicating a plasticity of the cell phenotype based on metabolic modulation. Sensitivity of γδT cells to metabolic changes results in diminished cytokine and growth factor signaling, reduced proliferation and homeostasis (Taylor et al., 2010).

Resident γδT cells in the skin are part of a complex regulatory network to balance the skin homeostasis by regulating keratinocyte differentiation and apoptosis (Sharp et al., 2005). γδT cells are important for the initiation of inflammation processes, release of cytokines (IL-1β, IL-6), and growth factors (PDGF, VEGF, IGF-1) (Schwacha et al., 2016). The observed alteration in the abundance of these cells in the skin of *mt-Atp8* mutant mice implies a potential functional consequence in the immune cell homeostasis in the skin and may be related to the altered skin inflammation progression in the mutant mice as observed in the antibody-transfer induced EBA mouse model.

4.6 *mt-Atp8* mutation induced indirect influence on skin microbiome

Ma *et al.* have described an association between mitochondrial haplogroups and the composition of microbial communities in the humans (Ma et al., 2014). These findings coincide and underline the findings in this work which equally identifies changes in the composition of skin colonization by bacteria dependent on an mtDNA encoded polymorphism in mice (Figure 24, Figure 25, Figure 26).

Performing an indicator species analysis revealed the presence of multiple bacterial species that show correlation with the mtDNA genotype. The altered abundance of commensal bacteria can have a severe impact on the balance of the skin immune milieu (Belkaid and Tamoutounour, 2016; Naik et al., 2012, 2015). Immunomodulatory functions of bacteria can thus alter and prime specific immunological profiles at the skin barrier, potentially altering the susceptibility to infection or auto-inflammatory/immune reaction.

Some of those identified indicator species are of specific interest in the proposed mechanism by which the mtDNA mutation derived phenotype segregates the disease outcome. *Staphylococcus xylosus* is a commensal bacterium of the skin and has been described as an opportunistic pathogen associated with skin pathologies and infections in mice lacking potent phagocyte functions caused by Nitric oxide synthase and NAPDH oxidase deficiency (Gozalo et al., 2010; Won et al., 2002). Although considered to be less pathogenic than other *Staphylococci*, *S. xylosus* has the potential to shape and influence the microbiota composition by biofilm formation (Planchon et al., 2006; Tan et al., 2014) and participate in the formation of the aforementioned pathologies. On the other hand, *Staphylococcus*

epidermidis is a commensal bacterium at the skin barrier and a putative pathogen during wound infections (Otto, 2009). The presence of this bacterium in mice is considered to be rare (Grice, 2015). However, *S. epidermidis* is able to colonize murine skin, as isolates of this bacterium persist on the skin and influence presence and activation status of immune cell populations in the skin and thereby affect the outcome of infectious episodes and wound healing (Belkaid and Tamoutounour, 2016; Naik et al., 2012, 2015). The presence of *S. epidermidis* on the skin was previously shown to induce the homing of IL-17$^+$ T cells to the skin (Naik et al., 2015).

On the skin of the *mt-Atp8* mutant strain, OTUs that have been classified as bacteria belonging to *Gordonia* or *Dietzia* were found to be more abundant. From the literature a certain anti-inflammatory potential is described (Click, 2012; Smaldini et al., 2014) and could potentially influence disease development in the EBA disease model by providing an anti-inflammatory stimulus to the skin milieu.

4.7 Interaction of microbiota, metabolism and immune system

In general the context of metabolic and inflammatory state may contribute to the emergence of aberrant skin microbiota composition and alter the local inflammatory milieu (Belkaid and Naik, 2013). Consequently, the microbial colonization of the skin and the skin immune milieu are in a fluid interaction developing a transient equilibrium in which any additional stimuli shift the balance again. The microbiome and immune cells interact at the skin barrier and influence each other. Regulation of this interaction involves DETCs as has been reported by MacLeod et al. (MacLeod et al., 2013). Changes in DETC populations, as observed in the *mt-Atp8* mutant

strain (Figure 9) are therefore a potential factor influencing the skin microbial composition.

Metabolism is heavily influenced by the composition of the gut microbiome. Alterations in the gut microbial structures are shaped by diet as well as the interaction with the immune milieu at the epithelial barrier (Belkaid and Hand, 2014). Metabolic profiles of the gut microbiome affect dietary degradation and thus influence the production of potent regulatory molecules like SCFA. The cause for the observed alteration of SCFA concentrations in the *mt-Atp8* mutant strains has not yet been conclusively identified. Skin and gut share extensive interactions which can affect inflammation at the skin barrier (Bowe and Logan, 2011; Kostic et al., 2013; Marrs and Flohr, 2016; O'Neill et al., 2016a). It is therefore likely that alterations of the skin microbiome in the *mt-Atp8* mutant strain are accompanied by alterations in the gut microbiome. This could potentially be associated with a shift in gut microbial metabolism and influence SCFA production by gut microbiota. The gut microbiome and SCFA can influence organ-functionality and systemic immune cell function by altering hematopoiesis (Trompette et al., 2014). Modulation of the immune homeostasis and autoimmunity by the microbiota has been recognized (Wu and Wu, 2012). Additionally, SCFA can directly influence inflammation by affecting GPR43 mediated cell recruitment in models of colitis, arthritis, and asthma (Maslowski et al., 2009). Thus, SCFA can be considered potent regulator of immune responses.

The postulated association of indicator species and their potential to modulate the immune homeostasis at the skin barrier is in line with observed alterations of the lipid composition (PUFA/SFA ratio, Figure 20) at the skin, indicating a potential role of microbial and metabolic connection to shape the inflammatory milieu at the skin barrier. Metabolic adaptations,

alteration in immune cell function and homeostasis, as well as differences in the structure of the skin microbiome are prominent changes observed in the *mt-Atp8* mutant mice. The interaction between these systems is flexibly regulated and kept in fluid equilibrium until it is disrupted by additional stimuli, i.e. induction of pathological conditions. The mutation in the *mt-Atp8* gene alters the mitochondrial function and causes the balance between metabolism, immune system, and environmental factors (i.e. microbiome at the skin barrier) that is regulated on many interrelated levels, to shift. The impact of the *mt-Atp8* mutation on the development of pathological conditions, like experimental EBA, arthritis, liver-failure, sepsis, metabolic disorder, steatosis, neuro-inflammation, etc. can be attributed to a variety of adaptations that are influencing each other and the response capacity of the system.

4.8 **Conclusion**

In conclusion, the mutation mt7778G/T in the mitochondrial encoded gene *mt-Atp8* in mice alters the mitochondrial function by changing the organization of the oxidative phosphorylation system, altering the activity of the component complexes and changing the flux through the respiratory chain. In the *mt-Atp8* mutant mice the steady-state metabolism is shifted and cellular energy status is reduced in addition to a dysregulation of the mitochondrial ROS homeostasis. Alterations in the cellular and systemic energy metabolism, alter the immune homeostasis, and influence the stimulation response of immune cells, i.e. T cells. The alterations in metabolism show tissue specific effects likely affecting the immune milieu in the skin. The homeostasis of immune cells in the skin is affected by the *mt-Atp8* mutation reducing the DETC population at the skin barrier, thus

likely affecting the interaction of the immune cells at the skin barrier with the environment. The microbial colonization on the skin is indirectly influenced by the mutation in the *mt-Atp8* gene, potentially caused by an interaction of metabolic changes as wells as immune cell responses altered by the mutation. The interaction of the skin microbiota with the skin barrier shapes the immune milieu and influences other inflammatory processes. A diminished capacity of the immune system to facilitate inflammatory processes in the *mt-Atp8* mutant strain ameliorates the severity of clinical phenotype of the antibody-transfer induced EBA model. Metabolic modulation and modulation of mitochondrial function are powerful targets for the modulation of inflammation and autoimmune diseases (Figure 29).

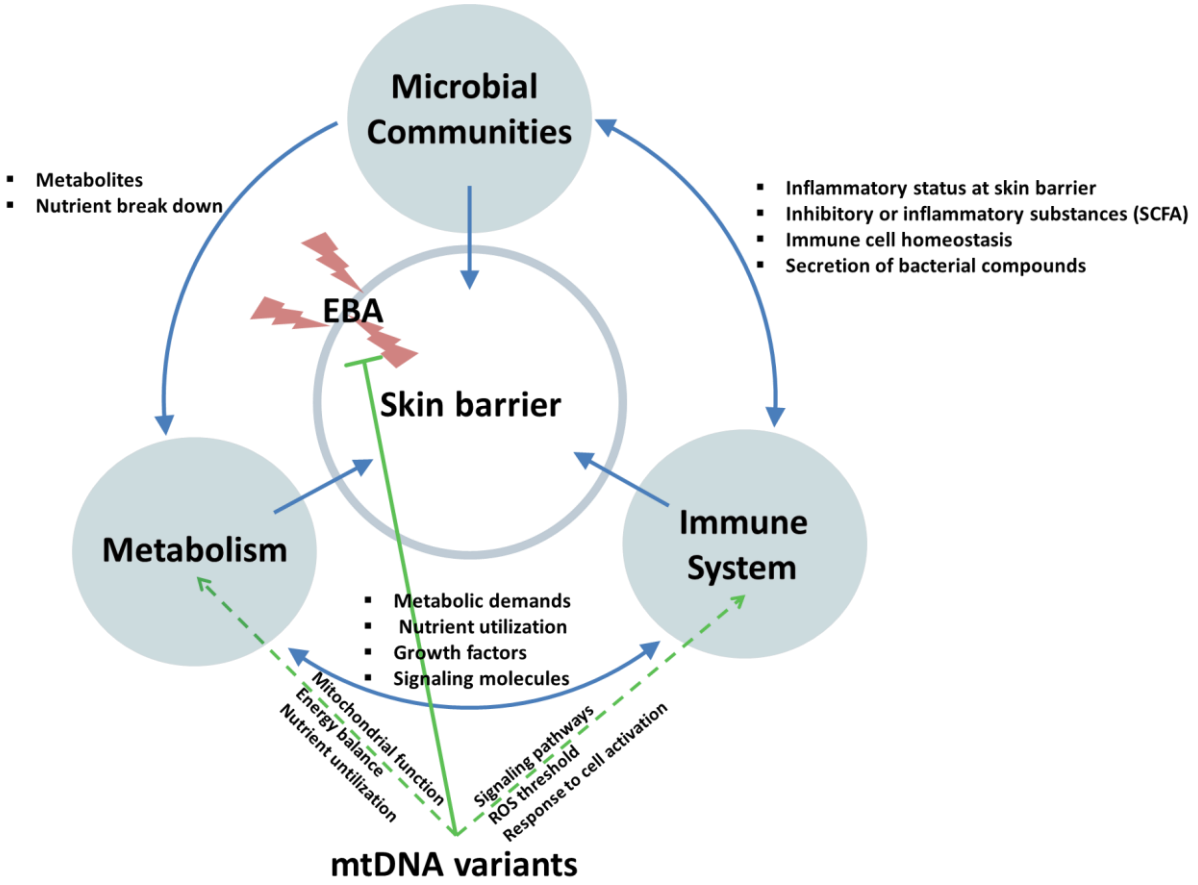

Figure 29. Theoretical model of the influence of mt-Atp8 mutation on experimental EBA through an interaction of the metabolism, immune system and microbiome at the skin barrier.

Further work is required to validate the identity of bacterial species that segregate in the *mt-Atp8* genotype. The impact of these bacteria on the homeostasis at the skin barrier has to be validated by isolation of bacterial indicator species. It is unlikely that individual bacteria in a homeostatic environment are the single cause of adaptive effects of the immune milieu. The changes of the microbial composition should be further analyzed to identify co-regulation between bacterial species that share an environment and form interdependent communities. Additionally, predictive functional profiling of microbial communities using the existing 16S rRNA NGS data should provide further insights into the capabilities of microbial communities to affect the host immune system. The influence of the *mt-Atp8* mutation is likely to affect additional phenotypes of skin pathologies and mitochondrial involvement in skin disorders and other autoimmune conditions in the skin. Mitochondrial metabolic adaptations are promising targets to modulate the immune response since metabolic control is critical for the inflammation process. Further investigations of the cellular adaptation induced by the *mt-Atp8* mutation may therefore help to identify novel strategies to modulate immune responses.

5 REFERENCES

Ahari, S.E., Houshmand, M., Panahi, M.S.S., Kasraie, S., Moin, M., and Bahar, M.A. (2007). Investigation on mitochondrial tRNALeu/Lys, NDI and ATPase 6/8 in Iranian multiple sclerosis patients. Cell. Mol. Neurobiol. *27*, 695–700.

Akira, S., Misawa, T., Satoh, T., and Saitoh, T. (2013). Macrophages control innate inflammation. Diabetes, Obes. Metab. *15*, 10–18.

Anderson, S., Bankier, A.T., Barrell, B.G., de Bruijn, M.H.L., Coulson, A.R., Drouin, J., Eperon, I.C., Nierlich, D.P., Roe, B.A., Sanger, F., et al. (1981). Sequence and organization of the human mitochondrial genome. Nature *290*, 457–465.

Arakawa, M., Dainichi, T., Ishii, N., Hamada, T., Karashima, T., Nakama, T., Yasumoto, S., Tsuruta, D., and Hashimoto, T. (2011). Lesional Th17 cells and regulatory T cells in bullous pemphigoid. Exp. Dermatol. *20*, 1022–1024.

Arch, J.R.S., Hislop, D., Wang, S.J.Y., and Speakman, J.R. (2006). Some mathematical and technical issues in the measurement and interpretation of open-circuit indirect calorimetry in small animals. Int. J. Obes. *30*, 1322–1331.

Auré, K., Dubourg, O., Jardel, C., Clarysse, L., Sternberg, D., Fournier, E., Laforêt, P., Streichenberger, N., Petiot, P., Gervais-Bernard, H., et al. (2013). Episodic weakness due to mitochondrial DNA MT-ATP6/8 mutations. Neurology *81*, 1810–1818.

Bakker, J.D. (2008). Increasing the utility of Indicator Species Analysis. J. Appl. Ecol. *45*, 1829–1835.

Bär, F., Bochmann, W., Widok, A., Von Medem, K., Pagel, R., Hirose, M., Yu, X., Kalies, K., König, P., Böhm, R., et al. (2013). Mitochondrial gene polymorphisms that protect mice from colitis. Gastroenterology *145*.

Barrientos, A., Fontanesi, F., and Díaz, F. (2009). Evaluation of the Mitochondrial Respiratory Chain and Oxidative Phosphorylation System Using Polarography and Spectrophotometric Enzyme Assays. In Current Protocols in Human Genetics, (Hoboken, NJ, USA: John Wiley & Sons, Inc.), pp. 1–13.

Belkaid, Y., and Hand, T.W. (2014). Role of the Microbiota in Immunity and Inflammation. Cell *157*, 121–141.

Belkaid, Y., and Naik, S. (2013). Compartmentalized and systemic control of tissue immunity by commensals. Nat. Immunol. *14*, 646–653.

Belkaid, Y., and Tamoutounour, S. (2016). The influence of skin microorganisms on cutaneous immunity. Nat. Rev. Immunol. *16*, 353–366.

Bengsch, B., Johnson, A.L., Kurachi, M., Odorizzi, P.M., Pauken, K.E., Attanasio, J., Stelekati, E., McLane, L.M., Paley, M.A., Delgoffe, G.M., et al. (2016). Bioenergetic Insufficiencies Due to Metabolic Alterations Regulated by the Inhibitory Receptor PD-1 Are an Early Driver of CD8+ T Cell Exhaustion. Immunity *45*, 358–373.

den Besten, G., Lange, K., Havinga, R., van Dijk, T.H., Gerding, A., van Eunen, K., Müller, M., Groen, A.K., Hooiveld, G.J., Bakker, B.M., et al. (2013a). Gut-derived short-chain fatty acids are vividly assimilated into host carbohydrates and lipids. Am. J. Physiol. Gastrointest. Liver Physiol. *305*, G900-10.

den Besten, G., van Eunen, K., Groen, A.K., Venema, K., Reijngoud, D.-J., and Bakker, B.M. (2013b). The role of short-chain fatty acids in the interplay between diet, gut microbiota, and host energy metabolism. J. Lipid Res. *54*, 2325–2340.

Bibb, M.J., Van Etten, R.A., Wright, C.T., Walberg, M.W., and Clayton, D.A. (1981). Sequence and gene organization of mouse mitochondrial DNA. Cell *26*, 167–180.

Bieber, K., Witte, M., Sun, S., Hundt, J.E., Kalies, K., Dräger, S., Kasprick, A., Twelkmeyer, T., Manz, R.A., König, P., et al. (2016). T cells mediate autoantibody-induced cutaneous inflammation and blistering in epidermolysis bullosa acquisita. Sci. Rep. *6*, 38357.

Boominathan, A., Vanhoozer, S., Basisty, N., Powers, K., Crampton, A.L., Wang, X., Friedricks, N., Schilling, B., Brand, M.D., and O'Connor, M.S. (2016). Stable nuclear expression of ATP8 and ATP6 genes rescues a mtDNA Complex V null mutant. Nucleic Acids Res. gkw756.

Bornhövd, C., Vogel, F., Neupert, W., and Reichert, A.S. (2006). Mitochondrial membrane potential is dependent on the oligomeric state of F1F0-ATP synthase supracomplexes. J. Biol. Chem. *281*, 13990–13998.

Bowe, W.P., and Logan, A.C. (2011). Acne vulgaris, probiotics and the gut-brain-skin axis - back to the future? Gut Pathog. *3*, 1.

Brown, G.C. (1992). Control of respiration and ATP synthesis in mammalian mitochondria and cells. Biochem. J. *284*, 1–13.

Buck, M.D., O'Sullivan, D., Klein Geltink, R.I., Curtis, J.D., Chang, C., Sanin, D.E., Qiu, J., Kretz, O., Braas, D., van der Windt, G.J.W., et al. (2016). Mitochondrial Dynamics Controls T Cell Fate through Metabolic Programming. Cell *166*, 63–76.

Cáceres, M. De, and Legendre, P. (2009). Associations between species and groups of sites: indices and statistical inference. Ecology *90*, 3566–3574.

Calvo, S.E., Clauser, K.R., and Mootha, V.K. (2016). MitoCarta2.0: an updated inventory of mammalian mitochondrial proteins. Nucleic Acids Res. *44*, D1251–D1257.

Chacko, B.K., Kramer, P.A., Ravi, S., Johnson, M.S., Hardy, R.W., Ballinger, S.W., and Darley-Usmar, V.M. (2013). Methods for defining distinct bioenergetic profiles in platelets, lymphocytes, monocytes, and neutrophils, and the oxidative burst from human blood. Lab. Investig. *93*, 690–700.

Chen, X., Song, M., Zhang, B., and Zhang, Y. (2016). Reactive Oxygen Species Regulate T Cell Immune Response in the Tumor Microenvironment. Oxid. Med. Cell. Longev. *2016*, 1–10.

Chinnery, P.F., and Hudson, G. (2013). Mitochondrial genetics. Br. Med. Bull. *106*, 135–159.

Chinnery, P.F., Elliott, H.R., Syed, A., and Rothwell, P.M. (2010). Mitochondrial DNA haplogroups and risk of transient ischaemic attack and ischaemic stroke: a genetic association study. Lancet Neurol. *9*, 498–503.

Čížková, A., Stránecký, V., Ivánek, R., Hartmannová, H., Nosková, L., Piherová, L., Tesařová, M., Hansíková, H., Honzík, T., Zeman, J., et al. (2008). Development of a human mitochondrial oligonucleotide microarray (h-MitoArray) and gene expression analysis of fibroblast cell lines from 13 patients with isolated F1Fo ATP synthase deficiency. BMC Genomics *9*, 38.

Click, R.E. (2012). A Potential "Curative" Modality for Crohn's Disease---Modeled after Prophylaxis of Bovine Johne's Disease. Mycobact. Dis. Tuberc. Lepr. *2*, 117.

Curi, R., Newsholme, P., MarzucaNassr, G.N., Takahashi, H.K., Hirabara, S.M., Cruzat, V., Krause, M., Ivo, P., and De Bittencourt, H. (2016). Regulatory principles in metabolism – then and now. Biochem. J *473*, 18451857.

D'Souza, A.D., Parikh, N., Kaech, S.M., and Shadel, G.S. (2007). Convergence of multiple signaling pathways is required to coordinately up-regulate mtDNA and mitochondrial biogenesis during T cell activation. Mitochondrion *7*, 374–385.

Damoiseaux, J.G.M.C., and Tervaert, J.W.C. (2002). The definition of autoimmune disease: are Koch's postulates applicable? Neth. J. Med. *60*, 266–268.

Dankowski, T., Schröder, T., Möller, S., Yu, X., Ellinghaus, D., Bär, F., Fellermann, K., Lehnert, H., Schreiber, S., Franke, A., et al. (2016). Male-specific association between MT-ND4 11719 A/G polymorphism and ulcerative colitis: a mitochondria-wide genetic association study. BMC Gastroenterol. *16*, 118.

Dieterle, F., Ross, A., Schlotterbeck, G., and Senn, H. (2006). Probabilistic Quotient Normalization as Robust Method to Account for Dilution of Complex Biological Mixtures. Application in 1 H NMR Metabonomics. Anal. Chem. *78*, 4281–4290.

Duchen, M.R. (1999). Contributions of mitochondria to animal physiology: from homeostatic sensor to calcium signalling and cell death. J. Physiol. *516 (Pt 1*, 1–17.

Dufrene, M., and Legendre, P. (1997). Species Assemblages and Indicator Species: The Need for a Flexible Asymmetrical Approach. Ecol. Monogr. *67*, 345.

Edgar, R.C. (2010). Search and clustering orders of magnitude faster than BLAST. Bioinformatics *26*, 2460–2461.

Edgar, D., and Trifunovic, A. (2009). The mtDNA mutator mouse: Dissecting mitochondrial involvement in aging. Aging (Albany. NY). *1*, 1028–1032.

Eipel, C., Hildebrandt, A., Scholz, B., Schyschka, L., Minor, T., Kreikemeyer, B., Ibrahim, S.M., and Vollmar, B. (2011). Mutation of mitochondrial ATP8 gene improves hepatic energy status in a murine model of acute endotoxemic liver failure. Life Sci. *88*, 343–349.

Feichtinger, R.G., Sperl, W., Bauer, J.W., and Kofler, B. (2014). Mitochondrial dysfunction: a neglected component of skin diseases. Exp. Dermatol. *23*, 607–614.

Fernandez-Marcos, P.J., and Auwerx, J. (2011). Regulation of PGC-1 , a nodal regulator of mitochondrial biogenesis. Am. J. Clin. Nutr. *93*, 884S–890S.

Fingerhut, R., Röschinger, W., Muntau, A.C., Dame, T., Kreischer, J., Arnecke, R., Superti-Furga, A., Troxler, H., Liebl, B., Olgemöller, B., et al. (2001). Hepatic carnitine palmitoyltransferase I deficiency: acylcarnitine profiles in blood spots are highly specific. Clin. Chem. *47*, 1763–1768.

Fischer-Stabauer, M., Boehner, A., Eyerich, S., Carbone, T., Traidl-Hoffmann, C., Schmidt-Weber, C.B., Cavani, A., Ring, J., Hein, R., and Eyerich, K. (2012). Differential in situ expression of IL-17 in skin diseases. Eur. J. Dermatol. *22*, 781–784.

Flaquer, A., Baumbach, C., Ladwig, K.-H., Kriebel, J., Waldenberger, M., Grallert, H., Baumert, J., Meitinger, T., Kruse, J., Peters, A., et al. (2015). Mitochondrial genetic variants identified to be associated with posttraumatic stress disorder. Transl. Psychiatry *5*, e524.

Frauwirth, K. a, and Thompson, C.B. (2004). Regulation of T lymphocyte metabolism. J. Immunol. *172*, 4661–4665.

Gimsa, U., Kanitz, E., Otten, W., and Ibrahim, S.M. (2009). Behavior and stress reactivity in mouse strains with mitochondrial DNA variations. Ann. N. Y. Acad. Sci. *1153*, 131–138.

Girardi, M. (2006). Immunosurveillance and immunoregulation by gammadelta T cells. J Invest Dermatol *126*, 25–31.

Glancy, B., and Balaban, R.S. (2012). Role of Mitochondrial Ca 2+ in the Regulation of Cellular Energetics. Biochemistry *51*, 2959–2973.

Goios, A., Pereira, L., Bogue, M., Macaulay, V., and Amorim, A. (2007). mtDNA phylogeny and evolution of laboratory mouse strains. Genome Res. *17*, 293–298.

Gozalo, A.S., Hoffmann, V.J., Brinster, L.R., Elkins, W.R., Ding, L., and Holland, S.M. (2010). Spontaneous Staphylococcus xylosus infection in mice deficient in NADPH oxidase and comparison with other laboratory mouse strains. J. Am. Assoc. Lab. Anim. Sci. *49*, 480–486.

Grice, E.A. (2015). The intersection of microbiome and host at the skin interface: genomic- and metagenomic-based insights. Genome Res. *25*, 1514–1520.

Di Guida, R., Engel, J., Allwood, J.W., Weber, R.J.M., Jones, M.R., Sommer, U., Viant, M.R., and Dunn, W.B. (2016). Non-targeted UHPLC-MS metabolomic data processing methods: a comparative investigation of normalisation, missing value imputation, transformation and scaling. Metabolomics *12*, 1–14.

Hamanaka, R.B., and Chandel, N.S. (2010). Mitochondrial reactive oxygen species regulate cellular signaling and dictate biological outcomes. Trends Biochem. Sci. *35*, 505–513.

Hamanaka, R.B., and Chandel, N.S. (2013). Mitochondrial metabolism as a regulator of keratinocyte differentiation. Cell. Logist. *3*, e25456.

Hayter, S.M., and Cook, M.C. (2012). Updated assessment of the prevalence, spectrum and case definition of autoimmune disease. Autoimmun. Rev. *11*, 754–765.

Heath, W.R., and Carbone, F.R. (2013). The skin-resident and migratory immune system in steady state and memory: innate lymphocytes, dendritic cells and T cells. Nat. Immunol. *14*, 978–985.

Hill, M.O. (1973). Diversity and Evenness: A Unifying Notation and Its Consequences. Ecology *54*, 427–432.

Hirose, M., Schilf, P., Benoit, S., Eming, R., Gläser, R., Homey, B., Kunz, M., Nebel, A., Peitsch, W.K., Pföhler, C., et al. (2015). Polymorphisms in the

mitochondrially encoded ATP synthase 8 gene are associated with susceptibility to bullous pemphigoid in the German population. Exp. Dermatol. *24*, 715–717.

Houtkooper, R.H., Mouchiroud, L., Ryu, D., Moullan, N., Katsyuba, E., Knott, G., Williams, R.W., and Auwerx, J. (2013). Mitonuclear protein imbalance as a conserved longevity mechanism. Nature *497*, 451–457.

Hudson, G., Gomez-Duran, A., Wilson, I.J., and Chinnery, P.F. (2014). Recent Mitochondrial DNA Mutations Increase the Risk of Developing Common Late-Onset Human Diseases. PLoS Genet. *10*, e1004369.

Johnson, K.R., Y Zheng, Q., Bykhovskaya, Y., Spirina, O., and Fischel-Ghodsian, N. (2001). A nuclear-mitochondrial DNA interaction affecting hearing impairment in mice. Nat. Genet. *27*, 191–194.

Johnson-Cadwell, L.I., Jekabsons, M.B., Wang, A., Polster, B.M., and Nicholls, D.G. (2007). "Mild Uncoupling" does not decrease mitochondrial superoxide levels in cultured cerebellar granule neurons but decreases spare respiratory capacity and increases toxicity to glutamate and oxidative stress. J. Neurochem. *101*, 1619–1631.

Jonckheere, A.I., Hogeveen, M., Nijtmans, L., van den Brand, M., Janssen, A., Diepstra, H., van den Brandt, F., van den Heuvel, B., Hol, F., Hofste, T., et al. (2009). A novel mitochondrial ATP8 gene mutation in a patient with apical hypertrophic cardiomyopathy and neuropathy. BMJ Case Rep. *2009*.

Jonckheere, A.I., Smeitink, J.A.M., and Rodenburg, R.J.T. (2012). Mitochondrial ATP synthase: Architecture, function and pathology. J. Inherit. Metab. Dis. *35*, 211–225.

Käding, N. (2015). Hypoxia regulates host cell metabolism and thereby enhancing Chlamydia pneumoniae growth. (Doctoral dissertation). Department of Molecular and Clinical Infectious Diseases - University of Lübeck http://d-nb.info/1080504060/34.

Kalantari-Dehaghi, M., Chen, Y., Deng, W., Chernyavsky, A., Marchenko, S., Wang, P.H., and Grando, S.A. (2013). Mechanisms of mitochondrial damage in keratinocytes by pemphigus vulgaris antibodies. J. Biol. Chem. *288*, 16916–16925.

Kamiński, M.M., Sauer, S.W., Kamiński, M., Opp, S., Ruppert, T., Grigaravičius, P., Grudnik, P., Gröne, H.-J., Krammer, P.H., and Gülow, K. (2012). T cell Activation Is Driven by an ADP-Dependent Glucokinase Linking Enhanced Glycolysis with Mitochondrial Reactive Oxygen Species Generation. Cell Rep. *2*, 1300–1315.

Kamiński, M.M., Röth, D., Krammer, P.H., and Gülow, K. (2013).

Mitochondria as Oxidative Signaling Organelles in T-cell Activation: Physiological Role and Pathological Implications. Arch. Immunol. Ther. Exp. (Warsz). *61*, 367–384.

Kasperkiewicz, M., Sadik, C.D., Bieber, K., Ibrahim, S.M., Manz, R.A., Schmidt, E., Zillikens, D., and Ludwig, R.J. (2016). Epidermolysis Bullosa Acquisita: From Pathophysiology to Novel Therapeutic Options. J. Invest. Dermatol. *136*, 24–33.

Kelly, R.D.W., Mahmud, A., McKenzie, M., Trounce, I.A., and St John, J.C. (2012). Mitochondrial DNA copy number is regulated in a tissue specific manner by DNA methylation of the nuclear-encoded DNA polymerase gamma A. Nucleic Acids Res. *40*, 10124–10138.

Kelso, A. (1994). The enigma of cytokine redundancy. Immunol. Cell Biol. *72*, 97–101.

Kenney, M.C., Chwa, M., Atilano, S.R., Falatoonzadeh, P., Ramirez, C., Malik, D., Tarek, M., Caceres-del-Carpio, J., Nesburn, A.B., Boyer, D.S., et al. (2014). Inherited mitochondrial DNA variants can affect complement, inflammation and apoptosis pathways: insights into mitochondrial-nuclear interactions. Hum. Mol. Genet. *23*, 3537–3551.

Kim, M., Qie, Y., Park, J., and Kim, C.H. (2016). Gut Microbial Metabolites Fuel Host Antibody Responses. Cell Host Microbe 1–13.

Köberlin, M.S., Snijder, B., Heinz, L.X., Baumann, C.L., Fauster, A., Vladimer, G.I., Gavin, A.C., and Superti-Furga, G. (2015). A Conserved Circular Network of Coregulated Lipids Modulates Innate Immune Responses. Cell *162*, 170–183.

Koopman, W.J.H., Distelmaier, F., Smeitink, J.A., and Willems, P.H. (2012). OXPHOS mutations and neurodegeneration. EMBO J. *32*, 9–29.

Kostic, A.D., Howitt, M.R., and Garrett, W.S. (2013). Exploring host – microbiota interactions in animal models and humans. Genes Dev. *27*, 701–718.

Kramer, P.A., Ravi, S., Chacko, B., Johnson, M.S., and Darley-Usmar, V.M. (2014). A review of the mitochondrial and glycolytic metabolism in human platelets and leukocytes: Implications for their use as bioenergetic biomarkers. Redox Biol. *2*, 206–210.

Kytövuori, L., Lipponen, J., Rusanen, H., Komulainen, T., Martikainen, M.H., and Majamaa, K. (2016). A novel mutation m.8561C>G in MT-ATP6/8 causing a mitochondrial syndrome with ataxia, peripheral neuropathy, diabetes mellitus, and hypergonadotropic hypogonadism. J. Neurol. 1–8.

Larsson, N.-G. (2010). Somatic mitochondrial DNA mutations in mammalian

aging. Annu. Rev. Biochem. *79*, 683–706.

Ledderose, C., Bao, Y., Lidicky, M., Zipperle, J., Li, L., Strasser, K., Shapiro, N.I., and Junger, W.G. (2014). Mitochondria Are Gate-keepers of T Cell Function by Producing the ATP That Drives Purinergic Signaling. J. Biol. Chem. *289*, 25936–25945.

Lewis, R.S. (2001). Calcium signaling mechanisms in T lymphocytes. Annu. Rev. Immunol. *19*, 497–521.

Lin, C.S., Sharpley, M.S., Fan, W., Waymire, K.G., Sadun, A. a, Carelli, V., Ross-Cisneros, F.N., Baciu, P., Sung, E., McManus, M.J., et al. (2012). Mouse mtDNA mutant model of Leber hereditary optic neuropathy. Proc. Natl. Acad. Sci. U. S. A. *109*, 20065–20070.

Ludwig, R.J. (2013). Clinical Presentation, Pathogenesis, Diagnosis, and Treatment of Epidermolysis Bullosa Acquisita. ISRN Dermatol. *2013*, 1–25.

Ma, J., Coarfa, C., Qin, X., Bonnen, P.E., Milosavljevic, A., Versalovic, J., and Aagaard, K. (2014). mtDNA haplogroup and single nucleotide polymorphisms structure human microbiome communities. BMC Genomics *15*, 257.

MacIver, N.J., Jacobs, S.R., Wieman, H.L., Wofford, J.A., Coloff, J.L., and Rathmell, J.C. (2008). Glucose metabolism in lymphocytes is a regulated process with significant effects on immune cell function and survival. J. Leukoc. Biol. *84*, 949–957.

MacLeod, A.S., Hemmers, S., Garijo, O., Chabod, M., Mowen, K., Witherden, D.A., and Havran, W.L. (2013). Dendritic epidermal T cells regulate skin antimicrobial barrier function. J. Clin. Invest. *123*, 4364–4374.

Marchenko, S., Chernyavsky, A.I., Arredondo, J., Gindi, V., and Grando, S.A. (2010). Antimitochondrial autoantibodies in pemphigus vulgaris: A missing link in disease pathophysiology. J. Biol. Chem. *285*, 3695–3704.

Marrs, T., and Flohr, C. (2016). The role of skin and gut microbiota in the development of atopic eczema. Br. J. Dermatol. *175*, 13–18.

Martínez-Reyes, I., Diebold, L.P., Kong, H., Schieber, M., Huang, H., Hensley, C.T., Mehta, M.M., Wang, T., Santos, J.H., Woychik, R., et al. (2016). TCA Cycle and Mitochondrial Membrane Potential Are Necessary for Diverse Biological Functions. Mol. Cell *61*, 199–209.

Maslowski, K.M., Vieira, A.T., Ng, A., Kranich, J., Sierro, F., Yu, D., Schilter, H.C., Rolph, M.S., Mackay, F., Artis, D., et al. (2009). Regulation of inflammatory responses by gut microbiota and chemoattractant receptor GPR43. Nature *461*, 1282–1286.

Mayr, J.A., Paul, J., Pecina, P., Kurnik, P., Förster, H., Fötschl, U., Sperl, W., and Houštěk, J. (2004). Reduced Respiratory Control with ADP and Changed Pattern of Respiratory Chain Enzymes as a Result of Selective Deficiency of the Mitochondrial ATP Synthase. Pediatr. Res. *55*, 988–994.

Mayr, J.A., Havlickova, V., Zimmermann, F., Magler, I., Kaplanova, V., Jesina, P., Pecinova, A., Nuskova, H., Koch, J., Sperl, W., et al. (2010). Mitochondrial ATP synthase deficiency due to a mutation in the ATP5E gene for the F1 subunit. Hum. Mol. Genet. *19*, 3430–3439.

Metallo, C.M., and Vander Heiden, M.G. (2013). Understanding Metabolic Regulation and Its Influence on Cell Physiology. Mol. Cell *49*, 388–398.

Mishur, R.J., Khan, M., Munkácsy, E., Sharma, L., Bokov, A., Beam, H., Radetskaya, O., Borror, M., Lane, R., Bai, Y., et al. (2016). Mitochondrial metabolites extend lifespan. Aging Cell *15*, 336–348.

Moreno-Loshuertos, R., Acín-Pérez, R., Fernández-Silva, P., Movilla, N., Pérez-Martos, A., Rodriguez de Cordoba, S., Gallardo, M.E., and Enríquez, J.A. (2006). Differences in reactive oxygen species production explain the phenotypes associated with common mouse mitochondrial DNA variants. Nat. Genet. *38*, 1261–1268.

Murphy, K.P., Travers, P., and Walport, M. (2011). Janeway's Immunobiology. (New York: Garland Science), pp. 611–668.

Naik, S., Bouladoux, N., Wilhelm, C., Molloy, M.J., Salcedo, R., Kastenmuller, W., Deming, C., Quinones, M., Koo, L., Conlan, S., et al. (2012). Compartmentalized Control of Skin Immunity by Resident Commensals. Science (80-.). *337*, 1115–1119.

Naik, S., Bouladoux, N., Linehan, J.L., Han, S.-J., Harrison, O.J., Wilhelm, C., Conlan, S., Himmelfarb, S., Byrd, A.L., Deming, C., et al. (2015). Commensal-dendritic-cell interaction specifies a unique protective skin immune signature. Nature *520*, 104–108.

Nielsen, M.M., Lovato, P., MacLeod, A.S., Witherden, D.A., Skov, L., Dyring-Andersen, B., Dabelsteen, S., Woetmann, A., Odum, N., Havran, W.L., et al. (2014). IL-1 -Dependent Activation of Dendritic Epidermal T Cells in Contact Hypersensitivity. J. Immunol. *192*, 2975–2983.

O'Neill, C.A., Monteleone, G., McLaughlin, J.T., and Paus, R. (2016a). The gut-skin axis in health and disease: A paradigm with therapeutic implications. BioEssays *38*, 1167–1176.

O'Neill, L.A.J., Kishton, R.J., and Rathmell, J. (2016b). A guide to immunometabolism for immunologists. Nat. Rev. Immunol. *16*, 553–565.

Oaks, Z., and Perl, A. (2014). Metabolic control of the epigenome in systemic

Lupus erythematosus. Autoimmunity *47*, 256–264.

Oksanen, J., Blanchet, F.G., Friendly, M., Kindt, R., Legendre, P., McGlinn, D., Minchin, P.R., O'Hara, R.B., Simpson, G.L., Solymos, P., et al. (2016). vegan: Community Ecology Package. R package version 2.4-1. https://CRAN.R-project.org/package=vegan.

Otto, M. (2009). Staphylococcus epidermidis — the "accidental" pathogen. Nat. Rev. Microbiol. *7*, 555–567.

Ozaki, K., and Leonard, W.J. (2002). Cytokine and Cytokine Receptor Pleiotropy and Redundancy. J. Biol. Chem. *277*, 29355–29358.

Pelletier, M., Billingham, L.K., Ramaswamy, M., and Siegel, R.M. (2014). Extracellular flux analysis to monitor glycolytic rates and mitochondrial oxygen consumption (Elsevier Inc.).

Pinkert, C.A., and Trounce, I.A. (2002). Production of transmitochondrial mice. Methods *26*, 348–357.

Planchon, S., Gaillard-Martinie, B., Dordet-Frisoni, E., Bellon-Fontaine, M.N., Leroy, S., Labadie, J., Hébraud, M., and Talon, R. (2006). Formation of biofilm by Staphylococcus xylosus. Int. J. Food Microbiol. *109*, 88–96.

Pope, J.E., and Thompson, A. (1999). Antimitochondrial antibodies and their significance in diffuse and limited scleroderma. J. Clin. Rheumatol. *5*, 206–209.

Price, M.N., Dehal, P.S., and Arkin, A.P. (2010). FastTree 2 – Approximately Maximum-Likelihood Trees for Large Alignments. PLoS One *5*, e9490.

Quast, C., Pruesse, E., Yilmaz, P., Gerken, J., Schweer, T., Yarza, P., Peplies, J., and Glockner, F.O. (2013). The SILVA ribosomal RNA gene database project: improved data processing and web-based tools. Nucleic Acids Res. *41*, D590–D596.

R Core Team (2016). R: A language and environment for statistical computing. R Foundation for Statistical Computing, Vienna, Austria. URL https://www.R-project.org/.

Ribas, V., García-Ruiz, C., and Fernández-Checa, J.C. (2016). Mitochondria, cholesterol and cancer cell metabolism. Clin. Transl. Med. *5*, 22.

Ribot, J.C., DeBarros, A., Pang, D.J., Neves, J.F., Peperzak, V., Roberts, S.J., Girardi, M., Borst, J., Hayday, A.C., Pennington, D.J., et al. (2009). CD27 is a thymic determinant of the balance between interferon-γ- and interleukin 17–producing γδ T cell subsets. Nat. Immunol. *10*, 427–436.

Rogers, G.W., Brand, M.D., Petrosyan, S., Ashok, D., Elorza, A.A., Ferrick, D.A., and Murphy, A.N. (2011). High throughput microplate respiratory

measurements using minimal quantities of isolated mitochondria. PLoS One *6*.

Rognes, T., Flouri, T., Nichols, B., Quince, C., and Mahé, F. (2016). VSEARCH: a versatile open source tool for metagenomics. PeerJ *4*, e2584.

Saad, S., Peter, M., and Dechant, R. (2013). In Scarcity and Abundance: Metabolic Signals Regulating Cell Growth. Physiology *28*, 298–309.

Samuels, D.C., Carothers, A.D., Horton, R., and Chinnery, P.F. (2006). The Power to Detect Disease Associations with Mitochondrial DNA Haplogroups. Am. J. Hum. Genet. *78*, 713–720.

Schapira, A.H. (2006). Mitochondrial disease. Lancet *368*, 70–82.

Scharping, N.E., Menk, A. V., Moreci, R.S., Whetstone, R.D., Dadey, R.E., Watkins, S.C., Ferris, R.L., and Delgoffe, G.M. (2016). The Tumor Microenvironment Represses T Cell Mitochondrial Biogenesis to Drive Intratumoral T Cell Metabolic Insufficiency and Dysfunction. Immunity *45*, 374–388.

Scheffler, K., Krohn, M., Dunkelmann, T., Stenzel, J., Miroux, B., Ibrahim, S., Von Bohlen Und Halbach, O., Heinze, H.J., Walker, L.C., Gsponer, J.A., et al. (2012). Mitochondrial DNA polymorphisms specifically modify cerebral b-amyloid proteostasis. Acta Neuropathol. *124*, 199–208.

Schloss, P.D., Westcott, S.L., Ryabin, T., Hall, J.R., Hartmann, M., Hollister, E.B., Lesniewski, R.A., Oakley, B.B., Parks, D.H., Robinson, C.J., et al. (2009). Introducing mothur: Open-Source, Platform-Independent, Community-Supported Software for Describing and Comparing Microbial Communities. Appl. Environ. Microbiol. *75*, 7537–7541.

Schmidt, E., and Zillikens, D. (2011). The Diagnosis and Treatment of Autoimmune Blistering Skin Diseases. Dtsch. Arztebl. *108*, 399–405.

Schmidt, E., and Zillikens, D. (2013). Pemphigoid diseases. Lancet *381*, 320–332.

Schneider, C. a, Rasband, W.S., and Eliceiri, K.W. (2012). NIH Image to ImageJ: 25 years of image analysis. Nat. Methods *9*, 671–675.

Schönig, S., Recke, A., Hirose, M., Ludwig, R.J., and Seeger, K. (2013). Metabolite analysis distinguishes between mice with epidermolysis bullosa acquisita and healthy mice. Orphanet J. Rare Dis. *8*, 93.

Schröder, T., Kucharczyk, D., Bär, F., Pagel, R., Derer, S., Jendrek, S.T., Sünderhauf, A., Brethack, A.K., Hirose, M., Möller, S., et al. (2016). Mitochondrial gene polymorphisms alter hepatic cellular energy metabolism and aggravate diet-induced non-alcoholic steatohepatitis. Mol.

Metab. *5*, 283–295.

Schwacha, M.G., Rani, M., Nicholson, S.E., Lewis, A.M., Holloway, T.L., Sordo, S., and Cap, A.P. (2016). Dermal γδ T-Cells Can Be Activated by Mitochondrial Damage-Associated Molecular Patterns. PLoS One *11*, e0158993.

Sena, L.A., Li, S., Jairaman, A., Prakriya, M., Ezponda, T., Hildeman, D.A., Wang, C., Schumacker, P.T., Licht, J.D., Perlman, H., et al. (2013a). Mitochondria Are Required for Antigen-Specific T Cell Activation through Reactive Oxygen Species Signaling. Immunity *38*, 225–236.

Sena, L.A., Li, S., Jairaman, A., Prakriya, M., Ezponda, T., Hildeman, D.A., Wang, C.R., Schumacker, P.T., Licht, J.D., Perlman, H., et al. (2013b). Mitochondria Are Required for Antigen-Specific T Cell Activation through Reactive Oxygen Species Signaling. Immunity *38*, 225–236.

Shanware, N.P., Bray, K., and Abraham, R.T. (2013). The PI3K, Metabolic, and Autophagy Networks: Interactive Partners in Cellular Health and Disease. Annu. Rev. Pharmacol. Toxicol. *53*, 89–106.

Sharp, L.L., Jameson, J.M., Cauvi, G., and Havran, W.L. (2005). Dendritic epidermal T cells regulate skin homeostasis through local production of insulin-like growth factor 1. Nat. Immunol. *6*, 73–79.

Shoffner, J.M., Brown, M.D., Torroni, A., Lott, M.T., Cabell, M.F., Mirra, S.S., Beal, M.F., Yang, C.C., Gearing, M., and Salvo, R. (1993). Mitochondrial DNA variants observed in Alzheimer disease and Parkinson disease patients. Genomics *17*, 171–184.

Simonson, D.C., and DeFronzo, R.A. (1990). Indirect calorimetry: methodological and interpretative problems. Am. J. Physiol. *258*, E399-412.

Sitaru, C., and Zillikens, D. (2005). Mechanisms of blister induction by autoantibodies. Exp. Dermatol. *14*, 861–875.

Smaldini, P.L., Stanford, J., Romanin, D.E., Fossati, C. a, and Docena, G.H. (2014). Down-regulation of NF-κB signaling by Gordonia bronchialis prevents the activation of gut epithelial cells. Innate Immun. *20*, 626–638.

Smith, A.C., and Robinson, A.J. (2016). MitoMiner v3.1, an update on the mitochondrial proteomics database. Nucleic Acids Res. *44*, D1258–D1261.

Spinazzi, M., Casarin, A., Pertegato, V., Salviati, L., and Angelini, C. (2012). Assessment of mitochondrial respiratory chain enzymatic activities on tissues and cultured cells. TL - 7. Nat. Protoc. *7 VN-re*, 1235–1246.

Stewart, J.B., and Chinnery, P.F. (2015). The dynamics of mitochondrial DNA heteroplasmy: implications for human health and disease. Nat. Rev. Genet.

16, 530–542.

Sumaria, N., Roediger, B., Ng, L.G., Qin, J., Pinto, R., Cavanagh, L.L., Shklovskaya, E., Fazekas de St Groth, B., Triccas, J.A., and Weninger, W. (2011). Cutaneous immunosurveillance by self-renewing dermal gammadelta T cells. J. Exp. Med. *208*, 505–518.

Tan, X., Liu, L., Liu, S., Yang, D., Liu, Y., Yang, S., Jia, A., and Qin, N. (2014). Genome of Staphylococcus xylosus and Comparison with S. aureus and S. epidermidis. J. Genet. Genomics *41*, 413–416.

Taylor, R.W., and Turnbull, D.M. (2005). Mitochondrial DNA mutations in human disease. Nat. Rev. Genet. *6*, 389–402.

Taylor, E.M., Jones, A.D., and Henagan, T.M. (2014). A Review of Mitochondrial-derived Fatty Acids in Epigenetic Regulation of Obesity and Type 2 Diabetes. J. Nutr. Heal. Food Sci. *2*.

Taylor, K.R., Mills, R.E., Costanzo, A.E., and Jameson, J.M. (2010). γδ T Cells Are Reduced and Rendered Unresponsive by Hyperglycemia and Chronic TNFα in Mouse Models of Obesity and Metabolic Disease. PLoS One *5*, e11422.

Trifunovic, A., Wredenberg, A., Falkenberg, M., Spelbrink, J.N., Rovio, A.T., Bruder, C.E., Bohlooly-Y, M., Gidlöf, S., Oldfors, A., Wibom, R., et al. (2004). Premature ageing in mice expressing defective mitochondrial DNA polymerase. Nature *429*, 417–423.

Trompette, A., Gollwitzer, E.S., Yadava, K., Sichelstiel, A.K., Sprenger, N., Ngom-Bru, C., Blanchard, C., Junt, T., Nicod, L.P., Harris, N.L., et al. (2014). Gut microbiota metabolism of dietary fiber influences allergic airway disease and hematopoiesis. Nat. Med. *20*, 159–166.

Vithayathil, S.A., Ma, Y., and Kaipparettu, B.A. (2012). Transmitochondrial cybrids: tools for functional studies of mutant mitochondria. Methods Mol. Biol. *837*, 219–230.

Wallace, D.C. (1999). Mitochondrial Diseases in Man and Mouse. Science (80-.). *283*, 1482–1488.

Wallace, D.C., and Chalkia, D. (2013). Mitochondrial DNA Genetics and the Heteroplasmy Conundrum in Evolution and Disease. Cold Spring Harb. Perspect. Biol. *5*, a021220–a021220.

van der Walt, J.M., Dementieva, Y.A., Martin, E.R., Scott, W.K., Nicodemus, K.K., Kroner, C.C., Welsh-Bohmer, K.A., Saunders, A.M., Roses, A.D., Small, G.W., et al. (2004). Analysis of European mitochondrial haplogroups with Alzheimer disease risk. Neurosci. Lett. *365*, 28–32.

Wang, C., Yosef, N., Gaublomme, J., Wu, C., Lee, Y., Clish, C.B., Kaminski, J., Xiao, S., Zu Horste, G.M., Pawlak, M., et al. (2015). CD5L/AIM Regulates Lipid Biosynthesis and Restrains Th17 Cell Pathogenicity. Cell *163*, 1413–1427.

Warnes, G.R., Bolker, B., Bonebakker, L., Gentleman, R., Liaw, W.H.A., Lumley, T., Maechler, M., Magnusson, A., Moeller, S., Schwartz, M., et al. (2016). gplots: Various R Programming Tools for Plotting Data. R package version 3.0.1. https://CRAN.R-project.org/package=gplots.

Weinberg, S.E., Sena, L.A., and Chandel, N.S. (2015). Mitochondria in the regulation of innate and adaptive immunity. Immunity *42*, 406–417.

Weir, J.B. de V. (1949). New methods for calculating metabolic rate with special reference to protein metabolism. J. Physiol. *109*, 1–9.

Weiss, H., Wester-Rosenloef, L., Koch, C., Koch, F., Baltrusch, S., Tiedge, M., and Ibrahim, S. (2012a). The mitochondrial Atp8 mutation induces mitochondrial ROS generation, secretory dysfunction, and β-cell mass adaptation in conplastic B6-mtFVB mice. Endocrinology *153*, 4666–4676.

Weiss, H., Wester-Rosenloef, L., Koch, C., Koch, F., Baltrusch, S., Tiedge, M., and Ibrahim, S. (2012b). The mitochondrial Atp8 mutation induces mitochondrial ROS generation, secretory dysfunction, and β-cell mass adaptation in conplastic B6-mt FVB mice. Endocrinology *153*, 4666–4676.

Whittaker, R.H. (1960). Vegetation of the Siskiyou Mountains, Oregon and California. Ecol. Monogr. *30*, 279–338.

van der Windt, G.J., Everts, B., Chang, C.H., Curtis, J.D., Freitas, T.C., Amiel, E., Pearce, E.J., and Pearce, E.L. (2012). Mitochondrial respiratory capacity is a critical regulator of CD8+ T cell memory development. Immunity *36*, 68–78.

Wittig, I., Meyer, B., Heide, H., Steger, M., Bleier, L., Wumaier, Z., Karas, M., and Schägger, H. (2010). Assembly and oligomerization of human ATP synthase lacking mitochondrial subunits a and A6L. Biochim. Biophys. Acta - Bioenerg. *1797*, 1004–1011.

Won, Y.S., Kwon, H.J., Oh, G.T., Kim, B.H., Lee, C.H., Park, Y.H., Hyun, B.H., and Choi, Y.K. (2002). Identification of Staphylococcus xylosus Isolated from C57BL/6J- Nos2 tm1Lau Mice with Dermatitis. Microbiol. Immunol. *46*, 629–632.

Wu, H.-J., and Wu, E. (2012). The role of gut microbiota in immune homeostasis and autoimmunity. Gut Microbes *3*, 4–14.

Yilmaz, P., Parfrey, L.W., Yarza, P., Gerken, J., Pruesse, E., Quast, C., Schweer, T., Peplies, J., Ludwig, W., and Glöckner, F.O. (2014). The SILVA and "All-species Living Tree Project (LTP)" taxonomic frameworks. Nucleic Acids Res. *42*, D643–D648.

Yin, Y., Choi, S.-C., Xu, Z., Perry, D.J., Seay, H., Croker, B.P., Sobel, E.S., Brusko, T.M., and Morel, L. (2015). Normalization of CD4+ T cell metabolism reverses lupus. Sci. Transl. Med. *7*, 274ra18-274ra18.

Yu, X., Koczan, D., Sulonen, A.M., Akkad, D.A., Kroner, A., Comabella, M., Costa, G., Corongiu, D., Goertsches, R., Camina-Tato, M., et al. (2008). mtDNA nt13708A variant increases the risk of multiple sclerosis. PLoS One *3*, 1–7.

Yu, X., Gimsa, U., Wester-Rosenlöf, L., Kanitz, E., Otten, W., Kunz, M., and Ibrahim, S.M. (2009a). Dissecting the effects of mtDNA variations on complex traits using mouse conplastic strains. Genome Res. *19*, 159–165.

Yu, X., Wester-Rosenlöf, L., Gimsa, U., Holzhueter, S.A., Marques, A., Jonas, L., Hagenow, K., Kunz, M., Nizze, H., Tiedge, M., et al. (2009b). The mtDNA nt7778 G/T polymorphism affects autoimmune diseases and reproductive performance in the mouse. Hum. Mol. Genet. *18*, 4689–4698.

Zebrowska, A., Wagrowska-Danilewicz, M., Danilewicz, M., Stasikowska-Kanicka, O., Cynkier, A., Sysa-Jedrzejowska, A., and Waszczykowska, E. (2013). IL-17 Expression in Dermatitis Herpetiformis and Bullous Pemphigoid. Mediators Inflamm. *2013*, 1–7.

Zhou, R., Yazdi, A.S., Menu, P., and Tschopp, J. (2011). A role for mitochondria in NLRP3 inflammasome activation. Nature *469*, 221–225.

6 APPENDIX

6.1 Supplemental tables and figures

*Table 11. List of metabolites incorporated in the Absolute*IDQ® *p150 Kit (Biocrates Life Sciences).*

Biochemical Name	Metabolite	Biochemical Name	Metabolite
DL-Carnitine	C0	Phosphatidylcholine diacyl C 40:2	PC aa C40:2
Decanoyl-L-carnitine	C10	Phosphatidylcholine diacyl C 40:3	PC aa C40:3
Decenoyl-L-carnitine	C10:1	Phosphatidylcholine diacyl C 40:4	PC aa C40:4
Decadienyl-L-carnitine	C10:2	Phosphatidylcholine diacyl C 40:5	PC aa C40:5
Dodecanoyl-L-carnitine	C12	Phosphatidylcholine diacyl C 40:6	PC aa C40:6
Dodecanedioyl-L-carnitine	C12-DC	Phosphatidylcholine diacyl C 42:0	PC aa C42:0
Dodecenoyl-L-carnitine	C12:1	Phosphatidylcholine diacyl C 42:1	PC aa C42:1
Tetradecanoyl-L-carnitine	C14	Phosphatidylcholine diacyl C 42:2	PC aa C42:2
Tetradecenoyl-L-carnitine	C14:1	Phosphatidylcholine diacyl C 42:4	PC aa C42:4
Hydroxytetradecenoyl-L-carnitine	C14:1-OH	Phosphatidylcholine diacyl C 42:5	PC aa C42:5
Tetradecadienyl-L-carnitine	C14:2	Phosphatidylcholine diacyl C 42:6	PC aa C42:6
Hydroxytetradecadienyl-L-carnitine	C14:2-OH	Phosphatidylcholine acyl-alkyl C 30:0	PC ae C30:0
Hexadecanoyl-L-carnitine	C16	Phosphatidylcholine acyl-alkyl C 30:1	PC ae C30:1
Hydroxyhexadecanoyl-L-carnitine	C16-OH	Phosphatidylcholine acyl-alkyl C 30:2	PC ae C30:2
Hexadecenoyl-L-carnitine	C16:1	Phosphatidylcholine acyl-alkyl C 32:1	PC ae C32:1
Hydroxyhexadecenoyl-L-carnitine	C16:1-OH	Phosphatidylcholine acyl-alkyl C 32:2	PC ae C32:2
Hexadecadienyl-L-carnitine	C16:2	Phosphatidylcholine acyl-alkyl C 34:0	PC ae C34:0
Hydroxyhexadecadienyl-L-carnitine	C16:2-OH	Phosphatidylcholine acyl-alkyl C 34:1	PC ae C34:1
Octadecanoyl-L-carnitine	C18	Phosphatidylcholine acyl-alkyl C 34:2	PC ae C34:2
Octadecenoyl-L-carnitine	C18:1	Phosphatidylcholine acyl-alkyl C 34:3	PC ae C34:3
Hydroxyoctadecenoyl-L-carnitine	C18:1-OH	Phosphatidylcholine acyl-alkyl C 36:0	PC ae C36:0
Octadecadienyl-L-carnitine	C18:2	Phosphatidylcholine acyl-alkyl C 36:1	PC ae C36:1
Acetyl-L-carnitine	C2	Phosphatidylcholine acyl-alkyl C 36:2	PC ae C36:2
Propionyl-L-carnitine	C3	Phosphatidylcholine acyl-alkyl C 36:3	PC ae C36:3
Malonyl-L-carnitine/ Hydroxybutyryl-	C3-DC (C4-OH)	Phosphatidylcholine acyl-alkyl C 36:4	PC ae C36:4
Hydroxypropionyl-L-carnitine	C3-OH	Phosphatidylcholine acyl-alkyl C 36:5	PC ae C36:5
Propenyl-L-carnitine	C3:1	Phosphatidylcholine acyl-alkyl C 38:0	PC ae C38:0
Butyryl-L-carnitine	C4	Phosphatidylcholine acyl-alkyl C 38:1	PC ae C38:1
Butenyl-L-carnitine	C4:1	Phosphatidylcholine acyl-alkyl C 38:2	PC ae C38:2
Valeryl-L-carnitine	C5	Phosphatidylcholine acyl-alkyl C 38:3	PC ae C38:3
Glutaryl-L-carnitine/	C5-DC (C6-OH)	Phosphatidylcholine acyl-alkyl C 38:4	PC ae C38:4
Methylglutaryl-L-carnitine	C5-M-DC	Phosphatidylcholine acyl-alkyl C 38:5	PC ae C38:5
Methylmalonyl-L-carnitine/	C5-OH (C3-DC-M)	Phosphatidylcholine acyl-alkyl C 38:6	PC ae C38:6
Tiglyl-L-carnitine	C5:1	Phosphatidylcholine acyl-alkyl C 40:0	PC ae C40:0
Glutaconyl-L-carnitine	C5:1-DC	Phosphatidylcholine acyl-alkyl C 40:1	PC ae C40:1
Fumaryl-L-carnitine/ Hexanoyl-L-	C6 (C4:1-DC)	Phosphatidylcholine acyl-alkyl C 40:2	PC ae C40:2
Hexenoyl-L-carnitine	C6:1	Phosphatidylcholine acyl-alkyl C 40:3	PC ae C40:3
Pimelyl-L-carnitine	C7-DC	Phosphatidylcholine acyl-alkyl C 40:4	PC ae C40:4
Octanoyl-L-carnitine	C8	Phosphatidylcholine acyl-alkyl C 40:5	PC ae C40:5
Octenoyl-L-carnitine	C8:1	Phosphatidylcholine acyl-alkyl C 40:6	PC ae C40:6
Nonayl-L-carnitine	C9	Phosphatidylcholine acyl-alkyl C 42:0	PC ae C42:0
Arginine	Arg	Phosphatidylcholine acyl-alkyl C 42:1	PC ae C42:1
Glutamine	Gln	Phosphatidylcholine acyl-alkyl C 42:2	PC ae C42:2
Glycine	Gly	Phosphatidylcholine acyl-alkyl C 42:3	PC ae C42:3
Histidine	His	Phosphatidylcholine acyl-alkyl C 42:4	PC ae C42:4
Methionine	Met	Phosphatidylcholine acyl-alkyl C 42:5	PC ae C42:5
Ornithine	Orn	Phosphatidylcholine acyl-alkyl C 44:3	PC ae C44:3
Phenylalanine	Phe	Phosphatidylcholine acyl-alkyl C 44:4	PC ae C44:4
Proline	Pro	Phosphatidylcholine acyl-alkyl C 44:5	PC ae C44:5
Serine	Ser	Phosphatidylcholine acyl-alkyl C 44:6	PC ae C44:6
Threonine	Thr	lysoPhosphatidylcholine acyl C14:0	lysoPC a C14:0
Tryptophan	Trp	lysoPhosphatidylcholine acyl C16:0	lysoPC a C16:0
Tyrosine	Tyr	lysoPhosphatidylcholine acyl C16:1	lysoPC a C16:1
Valine	Val	lysoPhosphatidylcholine acyl C17:0	lysoPC a C17:0
xLeucine	xLeu	lysoPhosphatidylcholine acyl C18:0	lysoPC a C18:0
Phosphatidylcholine diacyl C 24:0	PC aa C24:0	lysoPhosphatidylcholine acyl C18:1	lysoPC a C18:1
Phosphatidylcholine diacyl C 26:0	PC aa C26:0	lysoPhosphatidylcholine acyl C18:2	lysoPC a C18:2
Phosphatidylcholine diacyl C 28:1	PC aa C28:1	lysoPhosphatidylcholine acyl C20:3	lysoPC a C20:3
Phosphatidylcholine diacyl C 30:0	PC aa C30:0	lysoPhosphatidylcholine acyl C20:4	lysoPC a C20:4
Phosphatidylcholine diacyl C 30:2	PC aa C30:2	lysoPhosphatidylcholine acyl C24:0	lysoPC a C24:0
Phosphatidylcholine diacyl C 32:0	PC aa C32:0	lysoPhosphatidylcholine acyl C26:0	lysoPC a C26:0
Phosphatidylcholine diacyl C 32:1	PC aa C32:1	lysoPhosphatidylcholine acyl C26:1	lysoPC a C26:1
Phosphatidylcholine diacyl C 32:2	PC aa C32:2	lysoPhosphatidylcholine acyl C28:0	lysoPC a C28:0
Phosphatidylcholine diacyl C 32:3	PC aa C32:3	lysoPhosphatidylcholine acyl C28:1	lysoPC a C28:1
Phosphatidylcholine diacyl C 34:1	PC aa C34:1	lysoPhosphatidylcholine acyl C6:0	lysoPC a C6:0
Phosphatidylcholine diacyl C 34:2	PC aa C34:2	Hydroxyshingomyeline C 14:1	SM (OH) C14:1
Phosphatidylcholine diacyl C 34:3	PC aa C34:3	Hydroxyshingomyeline C 16:0	SM (OH) C16:1
Phosphatidylcholine diacyl C 34:4	PC aa C34:4	Hydroxyshingomyeline C 22:1	SM (OH) C22:1
Phosphatidylcholine diacyl C 36:0	PC aa C36:0	Hydroxyshingomyeline C 22:2	SM (OH) C22:2
Phosphatidylcholine diacyl C 36:1	PC aa C36:1	Hydroxyshingomyeline C 24:1	SM (OH) C24:1

Phosphatidylcholine diacyl C 36:2	PC aa C36:2	Shingomyeline C 16:0	SM C16:0
Phosphatidylcholine diacyl C 36:3	PC aa C36:3	Shingomyeline C 16:1	SM C16:1
Phosphatidylcholine diacyl C 36:4	PC aa C36:4	Shingomyeline C 18:0	SM C18:0
Phosphatidylcholine diacyl C 36:5	PC aa C36:5	Shingomyeline C 18:1	SM C18:1
Phosphatidylcholine diacyl C 36:6	PC aa C36:6	Shingomyeline C 20:2	SM C20:2
Phosphatidylcholine diacyl C 38:0	PC aa C38:0	Shingomyeline C 22:3	SM C22:3
Phosphatidylcholine diacyl C 38:1	PC aa C38:1	Shingomyeline C 24:0	SM C24:0
Phosphatidylcholine diacyl C 38:3	PC aa C38:3	Shingomyeline C 24:1	SM C24:1
Phosphatidylcholine diacyl C 38:4	PC aa C38:4	Shingomyeline C 26:0	SM C26:0
Phosphatidylcholine diacyl C 38:5	PC aa C38:5	Shingomyeline C 26:1	SM C26:1
Phosphatidylcholine diacyl C 38:6	PC aa C38:6	Hexose	H1
Phosphatidylcholine diacyl C 40:1	PC aa C40:1		

Table 12. Bacterial families of indicator species of associated with wild-type or mutant mice. Overlap of independent studies is shown in Figure 27.

Indicator species for B6 wild-type mice			Indicator species for *mt-Atp8* mustant mice			Overlap between wild-type and *mt-Atp8* mutant mice in all replicates of skin microbiota study		
Overlap between replicates of skin microbiota study	**Number of OTUs**	**Bacterial family**	**Overlap between replicates of skin microbiota study**	**Number of OTUs**	**Bacterial family**	**overlap or unique in**	**Number of OTUs**	**Bacterial family**
Overlap in replicates 1 2 3	2	Staphylococcaceae Bacteroidales_S24-7_group	Overlap in replicates 1 3	7	Lachnospiraceae Streptococcaceae Prevotellaceae Bacteroidales_S24-7_group Firmicutes_unclassified Bacteroidaceae Aerococcaceae	overlap between wild-type and *mt-Atp8* mutant mice	20	Flavobacteriaceae Erysipelotrichaceae Coriobacteriaceae Lachnospiraceae Streptococcaceae Bacteria_unclassified Prevotellaceae Ruminococcaceae Helicobacteraceae Bacteroidales_S24-7_group Moraxellaceae Porphyromonadaceae Bacillaceae Burkholderiaceae Acetobacteraceae Bacteroidaceae Corynebacteriales_unclassified Family_XI Alcaligenaceae Staphylococcaceae
Overlap in replicates 2 3	1	Family_XI						
Overlap in replicates 1 2	2	Prevotellaceae Ruminococcaceae						
Unique found in replicate 3	7	Erysipelotrichaceae Clostridia_unclassified Streptococcaceae Lachnospiraceae Bacteria_unclassified Carnobacteriaceae Planococcaceae	Unique found in replicate 3	3	Enterococcaceae Bacteroidales_unclassified Staphylococcaceae			
			Unique found in replicate 2	2	Helicobacteraceae Corynebacteriales_unclassified			
Unique found in replicate 2	1	Sphingomonadaceae						
Unique found in replicate 1	18	Flavobacteriaceae Micrococcales_unclassified Lactobacillaceae Coriobacteriaceae Acetobacteraceae Bacteroidaceae Alicyclobacillaceae Corynebacteriales_unclassified Bradyrhizobiaceae Leuconostocaceae Alcaligenaceae Helicobacteraceae Moraxellaceae Porphyromonadaceae Burkholderiaceae Bacillaceae Deferribacteraceae Anaeroplasmataceae	Unique found in replicate 1	34	Flavobacteriaceae Rhodocyclaceae Vibrionaceae Erysipelotrichaceae Proteobacteria_unclassified Coriobacteriaceae Bacteria_unclassified Rhodobacteraceae Comamonadaceae Ruminococcaceae Corynebacteriaceae Enterobacteriaceae Veillonellaceae Moraxellaceae Rhodospirillaceae Gastranaerophilales_unclassified Porphyromonadaceae Burkholderiaceae Bacillaceae Neisseriaceae Anaplasmataceae Clostridiales_vadinBB60_group Micrococcaceae Oceanospirillaceae Acetobacteraceae Rikenellaceae Clostridiales_unclassified Chloroplast_unclassified Fusobacteriaceae Cyanobacteria_unclassified Leptotrichiaceae Family_XI Alcaligenaceae 480-2	Unique in wild-type mice across all replicates	11	Lactobacillaceae Carnobacteriaceae Planococcaceae Deferribacteraceae Clostridia_unclassified Micrococcales_unclassified Sphingomonadaceae Alicyclobacillaceae Bradyrhizobiaceae Leuconostocaceae Anaeroplasmataceae
						Unique in *mt-Atp8* mutant mice across all replicates	26	Rhodocyclaceae Vibrionaceae Proteobacteria_unclassified Enterococcaceae Rhodobacteraceae Comamonadaceae Corynebacteriaceae Enterobacteriaceae Veillonellaceae Rhodospirillaceae Bacteroidales_unclassified Gastranaerophilales_unclassified Neisseriaceae Clostridiales_vadinBB60_group Anaplasmataceae Micrococcaceae Oceanospirillaceae Firmicutes_unclassified Rikenellaceae Chloroplast_unclassified Clostridiales_unclassified Fusobacteriaceae Cyanobacteria_unclassified Leptotrichiaceae 480-2 Aerococcaceae

6.2 **Materials & Equipment**

Material	**vendor**
5,5′-Dithiobis(2-nitrobenzoic acid), (DTNB)	Sigma Aldrich, Darmstadt, Germany
6x DNA Loading Dye	Thermo Fisher Scientific, Dreieich, Germany
96-well plate, PCR grade	Sarstedt AG & Co., Nümbrecht, Germany
Acetic acid, glacial	Merck KGaA, Darmstadt, Germany
Aceton	Carl Roth GmbH & Co. KG, Karlsruhe, Germany
Acetyl-Coenzyme A (Acetyl-CoA)	Sigma Aldrich, Darmstadt, Germany
Adenosine diphosphate (ADP)	Sigma Aldrich, Darmstadt, Germany
Adenosine triphosphate (ATP)	Sigma Aldrich, Darmstadt, Germany
Agencourt® Ampure® XP	Beckman Coulter
Agilent High Sensitivity DNA Kit	Agilent Technologies
Amplex Red kit	Thermo Fisher Scientific, Dreieich, Germany
Antimycin A	Sigma, Darmstadt, Germany
BD Cytofix/Cytoperm buffer	BD Biosciences, Heidelberg, Germany
BD Cytoperm Permeabilization Buffer Plus	BD Biosciences, Heidelberg, Germany
BD Perm/Wash buffer (10x)	BD Biosciences, Heidelberg, Germany
Biozym LE Agarose	Biozym Scientific GmbH, Hessisch Oldendorf, Germany
Bis-Tris	Sigma Aldrich, Darmstadt, Germany
Bovine serum albumin fraction V-biotin free	Carl Roth GmbH & Co. KG, Karlsruhe, Germany
Bovine serum albumin fraction V-essentially fatty acid free	Sigma Aldrich, Darmstadt, Germany
BrdU	Sigma Aldrich, Darmstadt, Germany
Bromophenol blue	Sigma Aldrich, Darmstadt, Germany
Catch-All sample collection swabs	Biozym Scientific GmbH, Germany
CCCP	Sigma Aldrich, Darmstadt, Germany
CellTak™	Corning, Corning, USA
CellTiter-Glo® Luminescent Cell Viability Assay Kit	Promega GmbH, Mannheim, Germany
Clarity™ Western ECL Substrate	Bio-Rad Laboratories GmbH, Munich, Germany
Coomassie brilliant blue R-250	Bio-Rad Laboratories GmbH, Munich, Germany
Coomassie Brilliant G-250 dye	Sigma Aldrich, Darmstadt, Germany
Cytochrome c	SERVA Electrophoresis GmbH, Heidelberg, Germany
D-(+)-glucose solution (10 %)	Sigma Aldrich, Darmstadt, Germany
Dako Pen	Dako Deutschland GmbH, Hamburg, Germany

DAPI Fluoromount G	Southern Biotech, Birmingham, USA
Decylubiquinone	Sigma Aldrich, Darmstadt, Germany
Digitonin	Thermo Fisher Scientific, Dreieich, Germany
DMEM, no phenol red, no bi-carbonate, no glucose	Sigma Aldrich, Darmstadt, Germany
DNase	Sigma Aldrich, Darmstadt, Germany
DPBS pH 7.2 0.01 M	Invitrogen GmbH, Darmstadt, Germany
EDTA solution 0.5M pH 8	AppliChem GmbH, Darmstadt, Germany
EGTA	Sigma Aldrich, Darmstadt, Germany
Endogenous Avidin/Biotin Blocking Kit	Thermo Fisher Scientific, Dreieich, Germany
EnzyLight™ ADP/ATP Ratio Assay Kit	BioAssay Systems, Hayward, USA
Eosin Y-solution alcoholic	Merck KGaA, Darmstadt, Germany
Ethanol 70%	Carl Roth GmbH & Co. KG, Karlsruhe, Germany
Ethanol 96%	Carl Roth GmbH & Co. KG, Karlsruhe, Germany
Ethanol, absolute for analysis	Merck Millipore Merck KGaA, Darmstadt, Germany
ExpressPlus™ PAGE Gels,10×8cm, 4-20% or 4-12% , 12 wells	GenScript, Piscataway, USA
FBS superior	Merck KGaA, Darmstadt, Germany
FCCP	Sigma Aldrich, Darmstadt, Germany
FoxP3 FJK-16a/PCH101 staining buffer set (Fixation/Permeabilization Buffer Set)	eBioscience, Frankfurt am Main, Germany
GeneJET Gel Extraction Kit	Thermo Fisher Scientific, Dreieich, Germany
GeneJET Genomic DNA Purification Kit	Thermo Fisher Scientific, Dreieich, Germany
GeneRuler 100 bp Plus DNA Ladder	Thermo Fisher Scientific, Dreieich, Germany
Glutamate	Sigma Aldrich, Darmstadt, Germany
Glycerol	Sigma Aldrich, Darmstadt, Germany
Glycine	Carl Roth GmbH & Co. KG, Karlsruhe, Germany
Haematoxylin	Merck KGaA, Darmstadt, Germany
HEPES	Sigma Aldrich, Darmstadt, Germany
HEPES,1 M solution	Biochrom GmbH, Berlin, Germany
Hydrochloric acid (25%)	Carl Roth GmbH & Co. KG, Karlsruhe, Germany
Isopropanol (100%)	Carl Roth GmbH & Co. KG, Karlsruhe, Germany
K_2HPO_4	Sigma Aldrich, Darmstadt, Germany
Ketamine hydrochloride	Sigma-Aldrich, Darmstadt, Germany
KH_2PO_4	Sigma Aldrich, Darmstadt, Germany
Lactate dehydrogenase / pyruvate kinase enzyme LDH/PK	Sigma Aldrich, Darmstadt, Germany

L-Glutamine, 200mM	Thermo Fisher Scientific, Dreieich, Germany
Lithium borohydride	Sigma Aldrich, Darmstadt, Germany
Magnesium chloride ($MgCl_2$)	Sigma Aldrich, Darmstadt, Germany
Malate	Sigma Aldrich, Darmstadt, Germany
Mannitol	Sigma Aldrich, Darmstadt, Germany
MEM non-essential amino acids	Thermo Fisher Scientific, Dreieich, Germany
Methanol	Carl Roth GmbH & Co. KG, Karlsruhe, Germany
$MgSO_4$	Sigma Aldrich, Darmstadt, Germany
MiSeq Reagent Kit v3	Illumina, San Diego, USA
MitoSOX	Thermo Fisher Scientific, Dreieich, Germany
Mitotracker Green FM	Thermo Fisher Scientific, Dreieich, Germany
MOPS	Carl Roth GmbH & Co. KG, Karlsruhe, Germany
NADH	Sigma Aldrich, Darmstadt, Germany
Na-Pyruvate	Thermo Fisher Scientific, Dreieich, Germany
n-Dodecyl β-D-maltoside (DDM)	Sigma Aldrich, Darmstadt, Germany
Nitrocellulose membranes, 0.45 µm	Bio-Rad Laboratories GmbH, Munich, Germany
Normal goat serum	Dako Deutschland GmbH, Hamburg, Germany
NovaQUANT™ Mouse Mitochondrial to Nuclear Ratio kit	Novagen, Merk Millipore, Darmstadt, Germany
NP-40	Sigma Aldrich, Darmstadt, Germany
Oligomycin	Sigma Aldrich, Darmstadt, Germany
Oxal acetic acid	Sigma Aldrich, Darmstadt, Germany
$Pb(NO_3)_2$	Sigma Aldrich, Darmstadt, Germany
PBS (phosphate buffer saline, cell culture grade)	Thermo Fisher Scientific, Dreieich, Germany
PCR plate seal, adhesive	Sarstedt AG & Co., Nümbrecht, Germany
Penicillin (10'000 U/mL) and Streptomycin (10'000 µg/mL)	Thermo Fisher Scientific, Dreieich, Germany
Percoll	GE Healthcare Europe GmbH, Freiburg, Germany
Phenylmethanesulfonyl fluoride (PMSF)	Sigma Aldrich, Darmstadt, Germany
Phosphoenolpyruvate (PEP)	Sigma Aldrich, Darmstadt, Germany
Phusion Hot Start II High-Fidelity	Thermo Fisher Scientific, Dreieich, Germany
Pierce™ BCA Protein Assay Kit	Thermo Fisher Scientific, Dreieich, Germany
Pierce™ Protease and Phosphatase Inhibitor Mini Tablets	Thermo Fisher Scientific, Dreieich, Germany
Ponceau S	Sigma Aldrich, Darmstadt, Germany
Potassium Chloride (KCl)	Sigma Aldrich, Darmstadt, Germany

Potassium cyanide (KCN)	Sigma Aldrich, Darmstadt, Germany
PowerLyzer Ultra Clean Microbial DNA Isolation Kit	MO BIO Laboratories, West Carlsbad, USA
Powersoil DNA Isolation Kit	MO BIO Laboratories, West Carlsbad, USA
primers for NGS library preparation (see Table 7and 8)	metabion GmbH, Planegg/Steinkirchen, germany
Protein G sepharose beads	Hölzel Diagnostika Handels GmbH, Köln, Germany
Proteinkinase K, lyophilized	Roche Diagnostics GmbH, Mannheim, Germany
Pyruvate	Sigma-Aldrich, Darmstadt, Germany
Qubit® dsDNA HS Assay Kit	Thermo Fisher Scientific, Dreieich, Germany
Rabbit sera, murine type VII collagen immunized	Eurogentec GmBH, Köln, Germany
RBS lysis buffer	Sigma Aldrich, Darmstadt, Germany
Rotenone	Sigma Aldrich, Darmstadt, Germany
Roti-Histofix (4% solution)	Carl Roth GmbH & Co. KG, Karlsruhe, Germany
RPMI 1640 with L-glutamine	Lonza Cologne GmbH, Köln, Germany
RPMI 1640 with L-glutamine w/o glucose w/o phenol red	Genaxxon bioscience GmbH, Ulm, Germany
RT-PCR Grade Water	Thermo Fisher Scientific, Dreieich, Germany
SCF-1 solution	Teknova, Hollister, USA
SERVAGel™N Native Gel, 3-12%	SERVA Electrophoresis GmbH, Heidelberg, Germany
Sodium chloride	Merck KGaA, Darmstadt, Germany
Sodium citrate dihydrate	Sigma Aldrich, Darmstadt, Germany
Sodium dedocylsulfate (SDS)	Carl Roth GmbH & Co. KG, Karlsruhe, Germany
sodium deoxycholate	Sigma Aldrich, Darmstadt, Germany
Sodium dithionite	Sigma Aldrich, Darmstadt, Germany
Sodium hydroxide	Merck KGaA, Darmstadt, Germany
Spectra Multicolor BR protein ladder	Thermo Fisher Scientific, Dreieich, Germany
Succinate	Sigma Aldrich, Darmstadt, Germany
Sucrose	Sigma Aldrich, Darmstadt, Germany
sulfosalicylic acid	Sigma Aldrich, Darmstadt, Germany
SYBR® Safe DNA Gel Stain	Thermo Fisher Scientific, Dreieich, Germany
Tissue-Tek O.C.T. compound	Sakura Finetek, Torrane USA
TMRE (Tetramethylrhodamine, ethyl ester, perchlorate)	Thermo Fisher Scientific, Dreieich, Germany
trichloracetic acid	Sigma Aldrich, Darmstadt, Germany
Tricine	Sigma Aldrich, Darmstadt, Germany
Tris (Tris hydroxymethyl aminomethane)	Serva electrophoresis GmbH, Heidelberg, Germany
Triton X-100	Carl Roth GmbH & Co. KG, Karlsruhe,

	Germany
Trypan blue	Sigma-Aldrich, Darmstadt, Germany
Tween 20 (Polyoxyethylene sorbitan monolaurate)	Sigma-Aldrich, Darmstadt, Germany
Whatman paper	Bio-Rad Laboratories GmbH, Munich, Germany
Xylazine hydrochloride	Sigma-Aldrich, Darmstadt, Germany
Xylene	Sigma-Aldrich, Darmstadt, Germany
β-mercaptoethanol	Sigma-Aldrich, Darmstadt, Germany

antibody	clone	Isotype	dilution	vendor	purpose
Biotin anti-mouse CD3ε Antibody	145-2C11	Armenian Hamster IgG	1:100	Biolegend	IIF
Biotin anti-mouse TCR γ/δ Antibody	GL3	Armenian Hamster IgG	1:100	Biolegend	IIF
Streptavidin Protein, DyLight 594 conjugate			1:200	Thermo Fisher Scientific	IIF
Streptavidin Protein, DyLight 488 conjugate			1:200	Thermo Fisher Scientific	IIF
anti-BrdU antibody, FITC conjugate	B44	IgG 1	ready-to-use	BD Biosciences	FC
anti-mouse CD4 antibody, APC conjugate	RM4-5	Rat IgG2a	1:160	eBioscience	FC
anti-mouse CD8a antibody, eFluor710 conjugate	53-6.7	Rat IgG2a	1:100	eBioscience	FC
anti-mouse CD25 antibody, PE conjugate	PC61.5	Rat IgG1	1:80	eBioscience	FC
anti-mouse IFN-g antibody, FITC conjugate	XMG1.2	Rat IgG1	1:100	eBioscience	FC
anti-mouse IL-17A antibody, PE conjugate	eBio17B7	Rat IgG2a	1:160	eBioscience	FC
anti-mouse IL-4 antibody, APC conjugate	11B11	Rat IgG1	1:40	eBioscience	FC
anti-mouse FoxP3 antibody, Alexa 488 conjugate	FJK-16s	Rat IgG2a	1:200	eBioscience	FC
MitoProfile® Total OXPHOS Rodent WB Antibody Cocktail (anti-NDUFB8, anti-C-II-30, anti-C-III-Core 2, anti-C-IV-I, anti-C-V-α)	20E9DH10C12, 21A11AE7, 13G12AF12BB 11, 1D6E1A8, 15H4C4	-	1:1000	MitoScience	WB
Rabbit, anti-mouse-*mt-Atp8* antibody	polyclonal	-	1:1000	Biorbyt	WB
Rabbit, anti-mouse IgG antibody, HRP conjugate	polyclonal	-	1:2000	DAKO	WB
Goat, anti-rabbit IgG antibody, HRP conjugate	polyclonal	-	1:2000	DAKO	WB

Equipment Source	**Supplier**
AgencourtSPRIPlate 96 Super Magnet Plate	Beckman Coulter
Agilent 2100 Bioanalyzer	Agilent Technologies
Allegra® X-15R Centrifuge	Beckman Coulter
Analytical scale ABS/ABJ-BA-def-1019	Kern & Sohn GmbH, Balingen, Germany
Bio-photometer plus 8.5 mm	Eppendorf AG, Hamburg, Germany
Centrifuge 5810R	Eppendorf AG, Hamburg, Germany
CFI Plan Apo λ 10x lense	Keyence Deutschland GmbH, Neu-Isenburg, Germany
CFI Plan Apo λ 20x lense	Keyence Deutschland GmbH, Neu-Isenburg, Germany
Cryostat CM3050 S	Leica Mikrosysteme Vertrieb GmbH, Wetzlar, Germany
FACSCalibur	Becton Dickinson GmbH, Heidelberg, Germany
Freezer -20˚	Liebherr Hausgeräte GmbH, Ochsenhausen, Germany
Freezer -80˚	Thermo Fisher Scientific GmbH, Dreieich, Germany
Freezer: Comfort NoFrost	Liebherr
Fridge: Comfort	Liebherr
Fusion Fx7 CCD imaging system	Vilber Lourmat Deutschland GmbH, Eberhardzell, Germany
GeneAmp® PCR System 9700	Applied Biosystems
HandyStep S dispenser	BRAND GmbH, Wertheim, Germany
HERAcell incubator	Heraeus Instruments GmbH, Hanau, Germany
Infinite M200 PRO ELISA reader	Thermo Fisher Scientific GmbH, Dreieich, Germany
Keyence microscope BZ-9000E	Keyence Deutschland GmbH, Neu-Isenburg, Germany
Laminar hood	NuAire, Plymouth, Minnesota, USA
Mastercycler ep realplex	Eppendorf AG, Hamburg, Germany
Micro centrifuge Micro Star 17R	VWR International GmbH, Darmstadt, Germany
Microtome	Leica Mikrosysteme Vertrieb GmbH, Wetzlar, Germany
Microwave: 700 & Grill	Severin
Mikro 120 Microliter Centrifuge	Hettich, Tuttlingen, Germany
Mini protean tetra system	Bio-Rad Laboratories GmbH, Munich, Germany
MiSeq Desktop Sequencer	Illumina, San Diego, USA

NanoDrop 2000c spectrophotometer	Thermo Fisher Scientific GmbH, Dreieich, Germany
Neubauer cell counting chamber	Laboroptik GmbH, Friedrichsdorf, Germany
open-circuit indirect calorimetry system, PhenoMaster System™	TSE, Bad Homburg, Germany
pH meter HI208	HANNA instruments, Vöhringen, Germany
Potter-Elvehjem glass homogenizer	Kimble Chase, Rockwood, USA
Power Pac basic	Bio-Rad Laboratories GmbH, Munich, Germany
Precellys 24 Homogenizer	Bertin Instruments, Rockville, USA
Precision balance 440-47N	Kern, Balingen, Germany
QUANTUM ST4 1100 imaging system	Vilber Lourmat Deutschland GmbH, Eberhardzell, Germany
Qubit® Fluorometer	Thermo Fisher Scientific
Refrigerator	Siemens, Munich, Germany
Seahorse XF24 Extracellular Flux Analyzer	Agilent Technologies Deutschland GmbH & Co. KG, Waldbronn, Germany
SpeedMill PLUS Homogenisator	Analytik Jena
Vortex	Vortex-Genie® 2-Scientific Industries Inc., Bohemia, New-York,USA
Vortex Adapter	MO BIO Laboratories, Inc.

6.3 **Publications**

Schilf, P., Peter, A., Hurek, T., and Stick, R. (2014). Lamins of the sea lamprey (*Petromyzon marinus*) and the evolution of the vertebrate lamin protein family. Eur. J. Cell Biol. *93*.

Hirose, M., **Schilf, P.**, Benoit, S., Eming, R., Gläser, R., Homey, B., Kunz, M., Nebel, A., Peitsch, W.K., Pföhler, C., et al. (2015). Polymorphisms in the mitochondrially encoded ATP synthase 8 gene are associated with susceptibility to bullous pemphigoid in the German population. Exp. Dermatol. *24*.

Hirose, M., **Schilf, P.**, Lange, F., Mayer, J., Reichart, G., Maity, P., Jöhren, O., Schwaninger, M., Scharffetter-Kochanek, K., Sina, C., et al. (2016). Uncoupling protein 2 protects mice from aging. Mitochondrion *30*.

Hirose, M., **Schilf, P.**, Gupta, Y., Wright, M.N., Jöhren, J., Wagner, A.E., Sina, C., Ziegler, A., Ristow, M., Ibrahim, S.M. (2016). Lifespan Effects of Mitochondrial Mutations. Comments on Latorre-Pellicer *et al*., Nature, Jul 28; 535(7613):561-5, 2016. *Nature doi*:10.1038/nature20778 (In Press)

Sezin, T., Krajewski, M., Wutkowski, A., Mousavi, S., Bieber, K., Ludwig, R., Dahlke, M., Rades, D., Schulze, F.S., Schmidt, E., Kalies, K., Gupta, Y., **Schilf, P.**, Ibrahim, S.M., König, P., Schwudke, D., Zillikens, D., Sadik, C.D. (2017). The leukotriene B_4 and its receptor BLT1 act as gatekeeper for neutrophil recruitment in autoantibody-driven skin inflammation. J. Invest. Dermatol. 1-10 doi: 10.1016/j.jid.2016.12.021.

6.4 **Conference contributions**

Poster presentations at

43rd Annual Meeting German Society for Immunology (DGfI), Mainz, Germany, September 2013

36th Symposium of the North-German Immunologists (NDI), Borstel, Germany, November 2014

9th International Meeting on Mitochondrial Pathology (EuroMIT), Tampere, Finland, June 2014

37th Symposium of the North-German Immunologists (NDI), Borstel, Germany, November 2014

Bioinformatics Satellite Meeting, Halle, Germany, September 2015

Oral presentation at

42nd Annual Meeting of the Arbeitsgemeinschaft Dermatologische Forschung (ADF), Ulm, Germany, March 2015

7 ACKNOWLEDGEMENTS

First and foremost I would like to thank Prof. Dr. Saleh Ibrahim for providing me with the opportunity to pursue my doctoral thesis in his lab and his guidance during my years of work. Thanks to encouraging discussions and different perspectives he greatly supported me in pursuing this work.

To Dr. Misa Hirose I am immensely grateful for her untiring support and patience as well as insightful discussions and feedback. Thanks to her constant vigilance I was able to find new ways to approach the topics of this thesis.

Many thanks go to Dr. Tanya Sezin for her help with and teaching of various wet lab techniques and to Dr. Yask Gupta for his help with statistical analysis and data processing. I am grateful to both of them for their encouragement and invaluable advice.

I am also grateful to Miriam Freitag who provide as sense of order when things were drifting towards chaos. I would like to thank Dr. Axel Künstner, Julia Bischof and Stephanie Dahl for their help in processing and analyzing the microbiome data. I gratefully acknowledge Prof. Dr. Jan Rupp for providing access to and support in operating the Seahorse XF24 Extracellular Flux Analyzer. Additionally, I want to acknowledge Dr. Cornelia Prehn, Dr. Werner Römisch Margl, Julia Scarpa and Katharina Faschinger for their cooperation and support with the metabolomics measurements performed at the Helmholtz Center Munich, Genome Analysis Center, Metabolomics Core Facility.

I dedicate this work to Jam. Without her endless support and encouragement I would not have been able to reach this point in my life.